Wind-Tunnel Investigations of the Aerodynamics of Bridge Stay Cable Cross-Sectional Shapes

U.S. Department of Transportation
Federal Highway Administration

FOREWORD

Cable-stayed bridge configurations have become more common over the past several decades for bridges in the medium- to long-span range. In some cases, serviceability problems involving large amplitude vibrations of stay cables under certain wind and wind-rain conditions have been observed. This study was conducted in response to State transportation departments' interest in developing improved design guidance for mitigation of excessive cable vibrations on cable-stayed bridges. The study included wind tunnel testing of bridge cable models having various cross-sectional shapes to evaluate the influence of cable roundness on cable aerodynamic behavior. The results of this study will be made available to the Post-Tensioning Institute's DC-45 Cable-Stayed Bridge Committee for consideration during their periodic updates of its publication, Recommendations for Stay Cable Design, Testing and Installation.[1]

This report will be of interest to bridge engineers, wind engineers, and consultants involved in the design of cable-stayed bridges. It is the sixth in a series of reports addressing the subject of aerodynamic stability of bridge stay cables.[2-6]

<div align="center">

Cheryl A. Richter, P.E., Ph.D.
Director, Office of Infrastructure
Research and Development

</div>

TECHNICAL REPORT DOCUMENTATION PAGE

1. Report No. FHWA-HRT-21-074	2. Government Accession No.	3. Recipient's Catalog No.	
4. Title and Subtitle Wind-Tunnel Investigations of the Aerodynamics of Bridge Stay Cable Cross-Sectional Shapes		5. Report Date August 2021	
		6. Performing Organization Code	
7. Author(s) Heidi Christiansen and Guy L. Larose		8. Performing Organization Report No. LTR-AL-2016-0001	
9. Performing Organization Name and Address National Research Council of Canada (NRC) Institute for Aerospace Research 1200 Montreal Road Ottawa, Ontario Canada K1A OR6		10. Work Unit No.	
		11. Contract or Grant No. DTFH61-13-D-00011	
12. Sponsoring Agency Name and Address Office of Infrastructure R&D Federal Highway Administration 6300 Georgetown Pike McLean, VA 22101-2296		13. Type of Report and Period Covered Laboratory Report; September 2014–September 2016	
		14. Sponsoring Agency Code HRDI-40	
15. Supplementary Notes The Contracting Officer's Representative (COR) was Harold R. Bosch (HRDI-40).			

16. Abstract

Experiments on stationary sectional models of scaled replica of bridge stay cables were carried out in a 2-by 3-m wind tunnel. The cross-sectional shapes of the cable models were obtained from direct measurements of stay cables for bridges in service. The purpose of the experiments was to establish a relationship between the level of eccentricity and surface irregularities of the cross-sectional shapes of stay cables and their propensity to experience wind-induced vibrations. The experiments confirmed that the aerodynamics of the stay cables are highly sensitive to their cross-sectional shapes. A small deviation from the mean curvature had an important influence on the aerodynamic force coefficients, in particular the mean across-wind force coefficients in the critical Reynolds number regime. Based on a quasi-steady analysis of the experimental results, negative aerodynamic damping in excess of 1 percent of critical could be predicted, confirming the propensity of stay cables to gallop for certain orientations to the flow, Reynolds numbers, and cross-sectional irregularities. Because of these experiments, researchers concluded that changes in across-wind forces as a function of angle of attack and Reynolds numbers could be the main contributors to anticipated wind-induced vibrations. Finally, this report discusses how such critical angles can be identified.

| 17. Key Words
Cable-stayed bridges; cables; vibrations; HDPE; pipe roundness; helical fillets; hazard mitigation; wind tunnel testing; galloping | | 18. Distribution Statement
No restrictions. This document is available to the public through the National Technical Information Service, Springfield, VA 22161.
http://www.ntis.gov | |
| 19. Security Classif. (of this report)
Unclassified | 20. Security Classif. (of this page)
Unclassified | 21. No. of Pages
114 | 22. Price
N/A |

Form DOT F 1700.7 (8-72)   Reproduction of completed page authorized.

SI* (MODERN METRIC) CONVERSION FACTORS

APPROXIMATE CONVERSIONS TO SI UNITS

Symbol	When You Know	Multiply By	To Find	Symbol
LENGTH				
in	inches	25.4	millimeters	mm
ft	feet	0.305	meters	m
yd	yards	0.914	meters	m
mi	miles	1.61	kilometers	km
AREA				
in²	square inches	645.2	square millimeters	mm²
ft²	square feet	0.093	square meters	m²
yd²	square yard	0.836	square meters	m²
ac	acres	0.405	hectares	ha
mi²	square miles	2.59	square kilometers	km²
VOLUME				
fl oz	fluid ounces	29.57	milliliters	mL
gal	gallons	3.785	liters	L
ft³	cubic feet	0.028	cubic meters	m³
yd³	cubic yards	0.765	cubic meters	m³
NOTE: volumes greater than 1,000 L shall be shown in m³				
MASS				
oz	ounces	28.35	grams	g
lb	pounds	0.454	kilograms	kg
T	short tons (2,000 lb)	0.907	megagrams (or "metric ton")	Mg (or "t")
TEMPERATURE (exact degrees)				
°F	Fahrenheit	5 (F-32)/9 or (F-32)/1.8	Celsius	°C
ILLUMINATION				
fc	foot-candles	10.76	lux	lx
fl	foot-Lamberts	3.426	candela/m²	cd/m²
FORCE and PRESSURE or STRESS				
lbf	poundforce	4.45	newtons	N
lbf/in²	poundforce per square inch	6.89	kilopascals	kPa

APPROXIMATE CONVERSIONS FROM SI UNITS

Symbol	When You Know	Multiply By	To Find	Symbol
LENGTH				
mm	millimeters	0.039	inches	in
m	meters	3.28	feet	ft
m	meters	1.09	yards	yd
km	kilometers	0.621	miles	mi
AREA				
mm²	square millimeters	0.0016	square inches	in²
m²	square meters	10.764	square feet	ft²
m²	square meters	1.195	square yards	yd²
ha	hectares	2.47	acres	ac
km²	square kilometers	0.386	square miles	mi²
VOLUME				
mL	milliliters	0.034	fluid ounces	fl oz
L	liters	0.264	gallons	gal
m³	cubic meters	35.314	cubic feet	ft³
m³	cubic meters	1.307	cubic yards	yd³
MASS				
g	grams	0.035	ounces	oz
kg	kilograms	2.202	pounds	lb
Mg (or "t")	megagrams (or "metric ton")	1.103	short tons (2,000 lb)	T
TEMPERATURE (exact degrees)				
°C	Celsius	1.8C+32	Fahrenheit	°F
ILLUMINATION				
lx	lux	0.0929	foot-candles	fc
cd/m²	candela/m2	0.2919	foot-Lamberts	fl
FORCE and PRESSURE or STRESS				
N	newtons	2.225	poundforce	lbf
kPa	kilopascals	0.145	poundforce per square inch	lbf/in²

*SI is the symbol for International System of Units. Appropriate rounding should be made to comply with Section 4 of ASTM E380.
(Revised March 2003)

TABLE OF CONTENTS

LIST OF FIGURES

LIST OF TABLES

LIST OF ABBREVIATIONS AND SYMBOLS

Abbreviations

DOF	degree-of-freedom
FHWA	Federal Highway Administration
HDPE	high-density polyethylene
HF	helical fillet
PE	polyethylene
PTI	Post-Tensioning Institute
SLS	selective laser sintering
UV	ultraviolet

Symbols

C_D	along-wind force coefficient
C_L	across-wind force coefficient
D	diameter
F	drag or lift force
f	frequency
f_n	natural frequency
I_u, I_v	intensity of turbulence, where u = longitudinal, v = lateral components
L	wind-exposed length of cable model
m	mass per unit exposed length of cable model
q	dynamic pressure
R	radius
Re	Reynolds number
Sc	Scruton number
t	time
U	mean wind speed
U/fB	reduced velocity
z_a	nondimensional aerodynamic damping parameter
α	angle of attack
α_N	angle between the vertical cable plane and the wind component normal to the cable axis
α'	cable-specific reference angle corresponding to α_n
α_s	structural angle
β	yaw angle
ϵ	surface roughness
κ	curvature
μ	air dynamic viscosity
ρ	air density
ϕ or Φ	cable-wind angle
τ	azimuth angle
θ	cable inclination angle
ζ	damping ratio as a fraction of critical

ζ_a aerodynamic damping ratio as a fraction of critical

EXECUTIVE SUMMARY

Experiments on stationary sectional models of scaled replica of bridge stay cables were carried out in a 2- by 3-m wind tunnel. The cross-sectional shapes of the cable models were obtained from direct measurements of stay cables for bridges in service. The purpose of the experiments was to establish a relationship between the level of eccentricity and surface irregularities of the cross-sectional shapes of stay cables and their propensity to experience wind-induced vibrations.

The Federal Highway Administration initiated this research project and carried out measurements of the cross-sectional shapes of stay cables on three in-service bridges in the United States, using a custom-built scanning robot that could climb up and down the stays. The measurements focused on stays covered with a polyethylene or high-density polyethylene sheathing, with and without helical fillets. From the measurements, four cross-sectional shapes were selected, and their aerodynamics were studied in the wind tunnel on sectional models. The models were made with a constant cross-sectional shape along their length at a geometrical scale of approximately 1:2 to 1:3. The sectional mean and fluctuating aerodynamic forces (along wind and across wind) were measured as a function of wind speed, inclination angle, yaw angle, and axial rotation of the cable models.

In addition to the tests on replicas of stay-cable cross-sectional shapes, sectional model tests were carried out for five other shapes. The additional shapes were selected to establish a set of reference cross-sectional force coefficients for the same Reynolds number range, surface roughness, and attitude to the flow as the replica of the cross-sectional shapes of cables in service. The results of the tests performed on the reference shapes were used to establish a link between cross-sectional irregularity and aerodynamic instability. They were also compared to the results of the tests performed on the cable replica.

The experiments confirmed that the aerodynamics of the stay cables are highly sensitive to their cross-sectional shapes. A small deviation from the mean curvature had an important influence on the aerodynamic force coefficients, in particular the mean across-wind force coefficients in the critical Reynolds number regime. Based on a quasi-steady analysis of the experimental results, negative aerodynamic damping in excess of 1 percent of critical could be predicted, confirming the propensity of stay cables to gallop for certain orientations to the flow, Reynolds numbers, and cross-sectional irregularities. As a result of these experiments, researchers concluded that changes in across-wind forces as a function of angle of attack and Reynolds numbers could be the main contributors to anticipated wind-induced vibrations. Finally, the report discusses how such critical angles can be identified.

CHAPTER 1. INTRODUCTION

BACKGROUND

The Federal Highway Administration (FHWA) oversees a large number of cable-stayed bridges in the United States currently in service or in the planning phase. In support of these large infrastructure projects, FHWA provides advice and expertise in wind engineering and aerodynamics to the bridge operators, focusing on long-term sustainability, efficiency, and low maintenance costs. Between 2001 and 2017, FHWA partnered with Canadian government research agencies, private engineering firms, and multiple universities to advance the knowledge with regard to the wind-induced vibration phenomena of stay cables for cable-stayed bridges.

Since stay cables are inclined and yawed to the winds, combined with the fact that they are in the critical Reynolds number regime for the majority of wind conditions they experience daily, the study of the aerodynamics of stay cables is challenging. Adding to the complexity of the problem, researchers observed during a wind-tunnel measurement campaign in 2011 that stay cables are not necessarily perfectly round, and this eccentricity can influence the wind-induced response of the stays.[4]

As a part of its multiyear experimental study of the effects of wind on inclined stay cables of cable-stayed bridges, FHWA, through its laboratory contractor, aimed to establish a relationship between the level of eccentricity of the cross-sectional shapes of stay cables and their propensity to experience wind-induced vibrations.

This report presents the work and findings of an FHWA-sponsored wind tunnel study. In summary, FHWA measured cross-sectional shapes of stay cables on three in-service bridges in the United States during the spring and early summer of 2015. To complete this task, FHWA used a custom-built scanning robot that could climb up and down the stays of these bridges. The measurements focused on stays covered with a sheathing of polyethylene (PE) or high-density polyethylene (HDPE), with and without helical fillets. From the measurements, four cross-sectional shapes were selected, and their aerodynamics were studied in the 2- by 3-m wind tunnel on stationary sectional models. The models were made with a constant cross-sectional shape along their length at a geometrical scale of approximately 1:2 to 1:3. The sectional mean and fluctuating aerodynamic forces (along wind and across wind) were measured as a function of wind speed, inclination angles, yaw angles, and axial rotations of the cable models.

In addition to the tests on replicas of cable cross-sectional shapes for bridges in service, sectional model tests were carried out for five other cross-sectional shapes. The additional shapes were selected to establish a set of reference cross-sectional coefficients for the same Reynolds number range, surface roughness, and attitude to the flow as the replicas of the cross-sectional shapes of cables in service. The results of the tests performed on the reference shapes were used to establish a link between cross-sectional irregularity and aerodynamic instability and compared to the results of the tests performed on the cable replicas.

The three shapes that exhibited the highest possibility of wind-induced vibrations based on the static coefficients were selected for a second-phase study: dynamic tests on free-to-respond models in 2016, whose results have yet to be published.

The sectional model tests of this study's first phase, which focused on 10 cross-sectional shapes of stay cables in the 2- by 3-m wind tunnel, took place in two periods: May 19 to 29, 2015, and July 27 to August 14, 2015. The main findings of the investigation for both series of tests are presented in this report. Appendix A provides the test log for the wind-tunnel test program that identifies the test runs performed for each of the cross-sectional shapes and the details of the test conditions. Appendix B presents additional results of the experiments in graphical form not covered in the main body of the report.

The documentation of the tests also includes video recordings on DVD, still images, and all the experimental data in electronic form. A thorough analysis of the results of the experiments is presented in two companion papers submitted for publication in scientific journals.[7, 8]

OBJECTIVES

The objective of this experimental campaign was to establish a relationship between the irregularities of the cross-sectional shapes of stay cables and their propensity to experience wind-induced vibrations. The experiments were designed to answer the following questions:

- How do the irregularities of the cross-sectional shapes, axial rotation, cable-wind angles, and Reynolds number affect the force coefficients?
- What is the influence of a helical fillet on the propensity of the inclined stay cables to experience wind-induced vibrations?
- Based on the quasi-steady theory, which shapes seem most prone to wind-induced vibrations?
- How does turbulence influence the behavior observed?

CHAPTER 2. TEST SETUP AND PROCEDURES

THE 2- BY 3-M WIND TUNNEL

The test program was undertaken in a 2- by 3-m wind tunnel located in an aerodynamic research laboratory in Ottawa, Ontario, Canada. The wind tunnel is a closed circuit atmospheric facility with a test section 2.7 m wide by 1.9 m high by 5.2 m long and a 9:1 contraction ratio. It is equipped with floor and roof turntables allowing precise yawing of models mounted vertically in the test section. The maximum wind speed of the wind tunnel, 140 m/s, and the size of the test section make this facility suitable for testing model-scale stay cables at full-scale Reynolds numbers while accommodating models with length-to-diameter ratios (aspect ratio) larger than 20. A picture of a typical stay cable model installed in the test section is shown in figure 1. The lower and upper turntables were equipped with supports that allowed changes of cable model inclination and yaw angles. Breathers on the floor and walls at the test section exit are vented to the tunnel surroundings to equalize the otherwise negative pressure in the test section with atmospheric pressure.
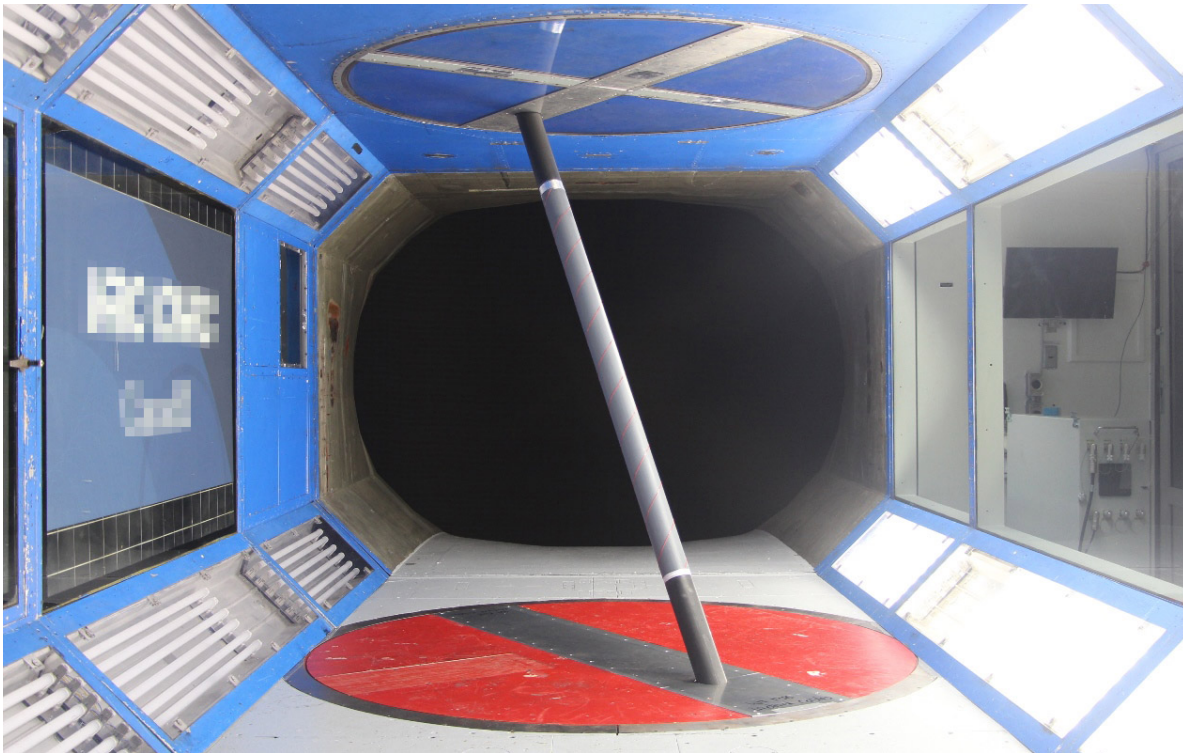
© 2015 NRC.

Figure 1. Photo. Downstream view of a cable model in the 2- by 3-m wind tunnel.

CABLE MODEL DESIGN AND FABRICATION

The experiments were carried out on stay-cable models with a minimum exposed length of 2,230 mm and a mean diameter of 88.9 mm for a length-to-diameter ratio of at least 25 for a cable model inclination of 60 degrees. The cable model consisted of an active central part

anchored to two dummy tubular sections at each end. The upper and lower sections were round with an outer diameter of 88.9 mm and made of steel. They penetrated the wind-tunnel floor and ceiling turntables, where they were rigidly anchored to the wind-tunnel structure. The length of the dummy sections that protruded out of the ceiling and floor turntables was adjustable to accommodate various cable inclinations. Views of the cable model and the lower and upper sections are shown in figure 2 and figure 3.

Figure 2. Photos. Views of the cable model and the lower dummy section interface with the floor turntable of the 2- by 3-m wind tunnel.

Figure 3. Photo. View of the upper dummy section with the two-component force sensor installed.

The majority of the tests were completed for a cable inclination of 60 degrees. However, for one of the setups, the model inclination was reduced to 45 degrees. For this inclination, the lower anchorage was too far downstream of the floor turntable, and a special anchorage had to be fabricated. The special anchorage was designed to minimize the aerodynamic interference between the cable model and the anchorage at the floor level. A view of the cable model inclined at 45 degrees and the special lower anchorage is shown in figure 4.

Figure 4. Photo. View from downstream of the cable model inclined at 45 degrees.

The central part of the model that sensed the aerodynamic forces (i.e., the metric part) consisted of a carbon fiber cylindrical spar 1500 mm long. Tubes with the study's cross-sectional shapes were mounted over this cylindrical spar. Carbon fiber was selected due to its high Young modulus (349 GPa) and its low density (1.7 g/cm^3) so that the bending frequency of the cable model on its supports would be higher than any vortex-shedding frequency of the model that could appear during the tests. These material properties helped avoid resonance and vibrations of the model.

Each end of the carbon fiber spar was fitted with clamps made of aluminum, one of which was designed with a threaded outer ring that could be removed to replace the cable model tube to test. The ring also served as a tightener that would squeeze the cable model tube in place between the clamps. The clamps, including the tightener, had an outer diameter of 88.9 mm. With the clamps, the metric part of the cable model had a total length of 1,560 mm. Views of the interface between the metric part of the model and the upper dummy sections are shown in figure 5. In figure 5, left side photo, one can see the upper dummy section, force sensor, aluminum clamp, tightening ring, and carbon fiber spar. In figure 5, middle photo, one can see the idem with steel spacer and SLS tube installed. In figure 5, right side photo, one can see the metallic tape cover installed.

Figure 5. Photos. Views of the interface between the central part of the model and the upper dummy section.

Researchers fabricated the cable model tubes using Selective Laser Sintering (SLS), a rapid prototyping technique. This method made it possible to produce tubes (or shells) with constant cross section directly from scans of stay cable in service with a light (0.96 g/cm^3) but relatively strong material. Nominally, the precision of the SLS machine was estimated to be 0.25 mm in the longitudinal and transverse directions. Since the precision of the SLS process is influenced by several parameters, a test piece was made and scanned. The results of the scanning were compared to the initial drawing. Deviations generally less than 0.18 mm were observed and considered satisfactory. From this verification, it was concluded that details in the cross-sectional geometry smaller than 0.5 mm, as measured on full-scale stay cables, could not be reproduced with enough accuracy in this study on model scale cables.

Due to the limitation in the size of the largest element that could be built in the SLS machine (400 mm in height), the cable model tubes were constructed out of smaller pieces. It was first attempted to construct a model out of four 380 mm long pieces. However, the pieces came out with a 2-3 mm bend after cooling, and a straight model could not be assembled. Instead, the models were constructed out of 11 smaller pieces, each 142 mm long. The pieces were designed with interlocks to facilitate their alignment and were subsequently glued together to form 1,500 mm long tubes. A photo of one of the SLS tubes before being painted is shown in figure 6. The small tab that can be seen on the picture was used for the initial orientation of the SLS tube and was removed for the tests.

Figure 6. Photo. End view of one of the SLS tubes before painting.

As a final treatment, the assembled tube was spray painted. Researchers wanted to match the ratio of the model surface roughness and the model diameter, ϵ/D, to that of HDPE tubes of full-scale cables. An example of the latter is the surface roughness data from two stay cable HDPE tubes obtained from the Øresund Bridge (a long-span cable-stayed bridge joining Copenhagen, Denmark to Malmö, Sweden). These two stay cable tubes had surface roughness-to-diameter ratios of 3.9×10^{-6} (mean diameter, $D = 250$ mm) and 6.5×10^{-6} ($D = 160$ mm), which were measured in connection with earlier experiments conducted by Larose et al.[9] In 2010, Matteoni and Georgakis performed measurements on three dummy cable sections with $D = 250$ mm at the Øresund Bridge.[10] The cable sections had no structural purpose and were installed for research and monitoring. In regions where the cables had not been mechanically damaged, $\epsilon/D = 2.8 \times 10^{-6}$ to 4×10^{-6}, and, in regions with major mechanical degradation regions, $\epsilon/D = 16 \times 10^{-6}$ to 20×10^{-6}.

The spray painting of the SLS tube cable models resulted in a surface roughness of $\epsilon = 1.56$ µm (i.e., $\epsilon/D = 17.5 \times 10^{-6}$). This surface roughness corresponded to the major degradation regions of the Øresund Bridge cables, which were somewhat larger than the full-scale equivalent. According to Engineering Sciences Data Unit International (ESDU), this surface roughness-to-diameter ratio is still considered smooth and smaller than the roughness-to-diameter for steel and was therefore considered appropriate for the study.[11] To match the surface roughness of the SLS tube, the steel dummy tubular sections were sandblasted and covered with two layers of spray paint, resulting in a surface roughness of $\epsilon/D = 1^9 \times 10^{-6}$.

The spacing between the outer diameter of the carbon fiber spar and the inner diameter of the SLS tubes was kept at a fraction of a millimeter. An axial rotation of the cable model tube (a change of angle of attack of the metric part of the cable model) consisted of releasing the tightener at the upper end of the carbon fiber spar (figure 5), rotating the long SLS tube around

the carbon fiber spar to the specified angular position and re-tying the tightener. For certain model shapes, the geometry would create a rather abrupt change in cross section in relation to the circular clamps. In such situations, tape would be placed over the two, along with putty underneath in the more severe cases, to smoothen the change in shape (figure 5).

The total mass of the metric part of the cable models was 7.32 kg, composed of 2.90 kg for the SLS tube, 2.89 kg for the carbon fiber spar, and 1.53 kg for the aluminum clamps and spacer. For two of the cable models, a right-handed double helical fillet was glued to the surface of the models after they had been tested with the smooth surface. The helical fillet was made from a plastic lace with a rectangular cross section of 1.56 mm wide by 0.78 mm high (equal to 1.75-percent-diameter by 0.88-percent-diameter of the model.) The dimensions of the model helical fillet were based on the helical fillets on the stay cables of one of the bridges scanned by FHWA for this study. The full-scale helical fillet had a width by height ratio of 3-mm wide by 1-mm high (equal to 1.75-percent-diameter wide by 0.58-percent-diameter high, where diameter equals 171.8 mm). The height of the helical fillet was slightly larger in the model setup. The pitch angle of the helical fillet on the full scale cable was 45 degrees, yielding a model pitch length = πD tan(90 − pitch angle) = $\pi \cdot 88.9$ mm·tan(45) = 280 mm for the cable model. Photos of one of the cable models with the helical fillets installed are shown in figure 7.
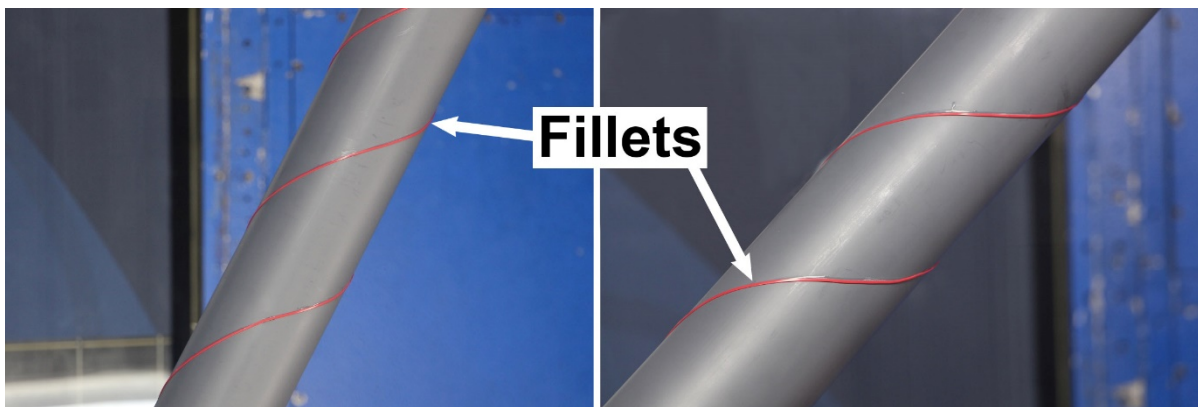
Figure 7. Photos. Views of a cable model with the helical fillets installed. Left: cable at 60-degree inclination. Right: cable at 45-degree inclination.

INSTRUMENTATION AND DATA ACQUISITION

Inside the lower and upper dummy sections of the cable model, a two-axis force sensor was mounted at each end to measure the drag (along-wind) and lift (across-wind) aerodynamic forces on the model perpendicular to the model axis. The metric central part of the model was clamped to the bearing journals of the force sensors, which were protruding from the dummy tubes. The force sensors were independent of the force introduction point (i.e., not affected by lever arm action), so any minor misalignment in the test setup that could arise would not affect the measurements.

The two-axis force sensors were rigidly anchored to the dummy sections of the model. Care was taken to ensure that the along-wind sensor was installed fully parallel to the flow direction using calibrated weights, a string, a pulley, a level, and a plumb bob. The calibration of the sensors and

signal conditioning electronics was also verified in situ using calibrated weights. Views of the force sensors are shown in figure 8.
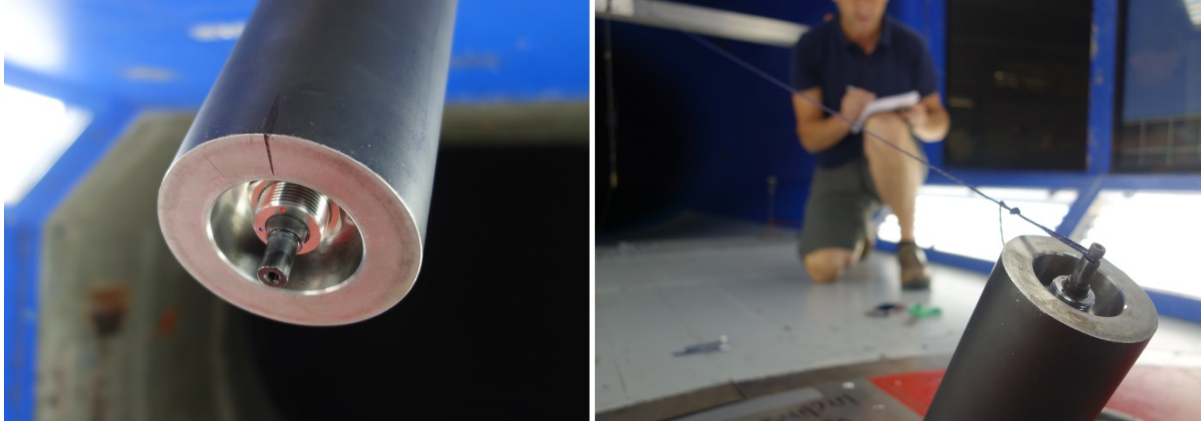
Photos © 2015 NRC.

Figure 8. Photos. Views of force sensors installed in the dummy sections. Left: top sensor. Right: lower sensor alignment.

The two-axis force sensors have a high structural stiffness which, when combined with the high stiffness and low weight of the metric part of the model (carbon fiber spar and SLS tube), allowed measurements of the aerodynamic force fluctuations for frequencies up to over 50 Hz. These sensors also provided stable and repeatable mean aerodynamic force measurements.

The instrumentation infrastructure of the 2- by 3-m wind tunnel determined the flow characteristics, which involved measurements of total pressure, static pressure, barometric pressure, temperature, and humidity at various positions in the wind tunnel. The measurements were used to define the mean dynamic pressure, wind speed, air density, and air viscosity for each test point.

All analog outputs from the load sensors were passed through an anti-aliasing filter (a low pass filter) prior to being sampled simultaneously at a frequency of 1,500 Hz. Afterward, the signal was passed through an analog-to-digital converter. The sampling time was set to 60 s. During the same period, the flow characteristics measurements were sampled at 10 Hz.

Aerodynamic force coefficients were calculated at the completion of each test run, as shown in figure 9. The coefficients were based on the total force acting on the cable (i.e., the summation of the two load cells in the along-wind and across-wind directions normal to the cable axis, respectively):

$$C_F = \frac{(F_{F,top} + F_{F,bot})}{0.5 \rho U^2 DL}$$

Figure 9. Equation. Aerodynamic force coefficient.

Where:
   F = drag (along-wind) or lift (across-wind) force.

12

U = incoming flow speed.
ρ = air density.
D = model diameter.
L = length of the metric part of the cable model.

Drag and lift in this report refer to the components normal to the cable axis, and their coefficients (C_D and C_L) are described in the equations in figure 10 and figure 11, respectively. Reynolds numbers in this report were based on the reference cylinder diameter D and the incoming flow speed U.

$$C_D = \frac{(\text{along} - \text{wind force})}{0.5\rho U^2 DL}$$

Figure 10. Equation. Drag coefficient.

$$C_L = \frac{(\text{across} - \text{wind force})}{0.5\rho U^2 DL}$$

Figure 11. Equation. Lift coefficient.

EXPERIMENTAL CONDITIONS

To prevent the transfer of loads between the active and dummy parts of the model, the dummy part locations were adjusted so that a 1–3 mm gap (depending on the model attitude) was left between the sections. The gaps were not sealed, and their influence is difficult to quantify, but they were not expected to have significant influence since the overall length of the metric section of the cable model was more than 1,000 times larger than the gaps.

Two tests were undertaken with the gap sealed with flexible tape and stiff aluminum tape. The development of the mean drag and lift coefficients as a function of Reynolds number in the first case was similar, although with a 36 percent reduction in the magnitude of the across-wind force coefficient. However, the researchers did not know if this difference was due to force transfer from the tape or sealing of the gap. In the second case with the aluminum tape, no differences were seen in the mean aerodynamic force coefficients.

End plates were not used in these experiments to provide conditions favorable for three-dimensional flow. End plates were used in the Larose et al. 2002 tests since they isolated the cable model from the horseshoe vortices that form at the intersection of the cable extremities and the wind tunnel floor and ceiling.[9] However, Zasso et al. found that end plates also generate a more two-dimensional flow, unlike what is expected in natural conditions, which was not desired for this study.[12] The length of the dummy sections was selected to limit the influence of the horseshoe vortices on the metric span of the cable model.

The blockage area ratio, evaluated as the ratio of the model diameter and the wind tunnel width, was three percent. A blockage correction was carried out on the force coefficients, wind speed, and Reynolds number based on the Maskell III approach for the cable model at a yaw angle of zero degrees.[13] However, the results of the tests on yawed models were not corrected for

blockage since it was believed that the uncertainties associated with the corrections for such cases would be similar to the magnitude of the corrections themselves.

The majority of the tests were completed in smooth flow. In smooth flow, the turbulence intensity in the along-wind direction was $I_u < 0.14$ percent, and the uniformity of the mean wind speed at the position of the model was well within 0.5 percent of the mean wind speed in the test section.

Researchers in this study also completed a series of experiments in turbulent flow. An isotropic grid of steel wires and nylon ropes was installed at the inlet of the test section, approximately 2.5 m upstream of the model. The turbulence intensity at the location of the center of the model for the turbulent flow tests was measured with a Cobra probe. This study indicated that, for the longitudinal component of the flow fluctuations, $I_u = 1.7-2.0$ percent, and for the lateral component, $I_v = 1.0-1.2$ percent. A view from downstream of the turbulence grid is shown in figure 12.
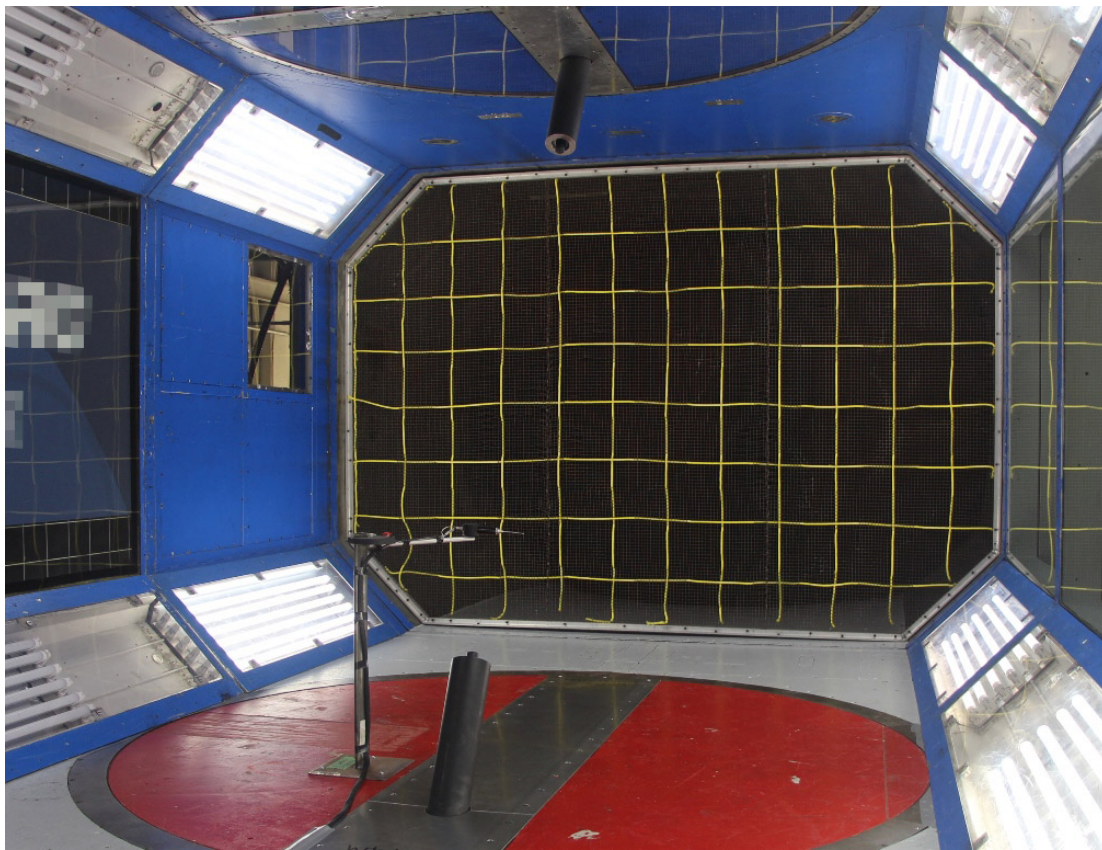
© 2015 NRC.

Figure 12. Photo. View from downstream of the turbulence grid in the 2- by 3-m wind tunnel with the cable model removed and Cobra probe installed.

CHAPTER 3. CROSS-SECTIONAL GEOMETRIES OF THE MODELS

REFERENCE MODELS

Throughout the life span of an HDPE tube, the outer shape changes for several reasons. The initial shape is controlled in the manufacturing phase using extrusion, yielding the first deviations from a circular cylinder. Depending on the diameter of the tube, the type of extruding machine, and the density and composition of the PE compound, a variety of shapes are possible.[14] A one percent deviation from the mean outside diameter is typically referred to as the tolerance for such tubes when a manufacturer must meet the standards that govern this product.

Hereafter, stacking of the tubes (or, as previously done, rolling on spools) for storage and transportation alters the outside shape of the tube. Once installed, the natural sagging of the stay cable and the side force exerted by the steel strands in the tube, combined with exposure to sunlight and temperature extremes, will impose large stresses on the tube, resulting in possible creep of the material over time.

As a result, a wide spectrum of cross-sectional shapes is possible. To establish a set of reference cross-sectional force coefficients for the same Reynolds number range, surface roughness, and attitude to the flow as the replicas of the shapes from field tests, sectional model tests were carried out for reference cross-sectional shapes that had relatively simple geometry.

In total, four reference shapes were selected and manufactured. One reference shape was a nominally circular cylinder (eccentricity between 0.2 and 0.3 percent of the mean diameter) that served as a benchmark for the other sections. For the three other reference shapes, two had oval sections with ovalization degrees of three and five percent, respectively, with respect to the cable diameter D, and the other had a flat face (figure 13). These three shapes were made up of one cylinder half, which was circular, and the other half, which was distorted. This setup was beneficial in understanding the influence of the shape distortions on the flow characteristics., as the aerodynamics of the round cylinder half would largely behave as those for a circular cylinder, isolating the influence of the shape distortion to one side of the cylinder.

The two generic oval sections reflected deformation during fabrication, stacking, and transportation. The oval shapes also reflected the influence of the sagging of the stay cable, which introduces tension in the lower part of the HDPE tube and compression in the upper part. Likewise, they could be considered a simplified version of stay cables with ice accretion. Two ovalization degrees were chosen to study the influence of the size of the cross-sectional distortion and thus the influence of the change in the surface curvature.

The flat-faced model was another possible shape distortion caused by the tension in the lower part of the HDPE tube from the stay cable sag. The lower distorted half was composed of three parts: an oval part (based on the equation of an ellipse with an ovalization degree of 5.45 percent diameter), a circular part, and a flat part with dimensions, as shown in figure 13. The percentage deviations of the reference shapes from a circular cylinder were believed to be within expected full-scale deformations. Up to 10 percent ovalization tolerances of the average diameter of

HDPE tubes was accepted on-site (i.e., any deformation that would arise from the handling and stacking during and after transportation).
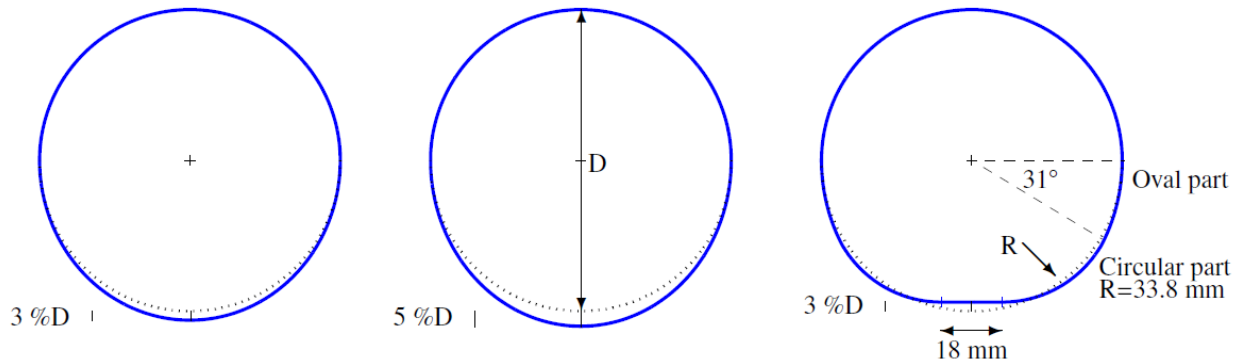
Source: FHWA.
Note: Dashed curves mark a perfectly round cylinder with the diameter $D = 88.9$ mm. The angle of attack $\alpha = 0$ degrees for wind from the bottom of the page.

Figure 13. Illustration. Sketch of three of the reference cross-sectional shapes.

The curvatures (κ) of the reference cross-sectional shapes are shown in figure 14. The curvatures are based on standard equations for a circle: $\kappa(\tau) = 1/R$, where R is the radius, and an ellipse: $\kappa(\tau) = ab/(a^2 \sin^2 \tau + b^2 \cos^2 \tau)$, where a and b are semi-major and semi-minor axes, and where $\tau = 0 \rightarrow 2\pi$. For the flat-faced cross section, there is a large discontinuity in the curvature between the flat part and the rounded corners. The curvature of the flat part is zero, which is not directly shown in figure 14 but indicated.
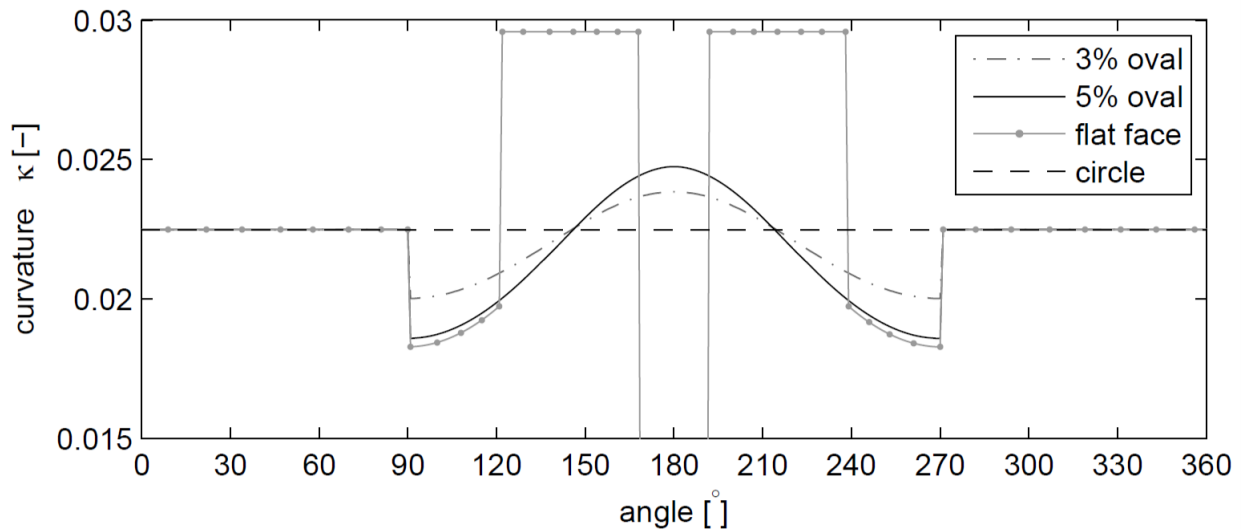
Source: FHWA.
Note: τ is positive clockwise starting from the top of the cross-sectional shapes of figure 13.

Figure 14. Graph. Variation of the curvatures of the reference shapes with azimuth angle, τ.

16

REPLICAS OF STAY CABLE SHAPES

Field Measurements of Cross-Sectional Shapes

FHWA carried out measurements of the cross-sectional shapes of stay cables on three in-service U.S. bridges in the spring and early summer of 2015, using a custom-built scanning robot that could climb up and down the stays. The measurements focused on stays covered with an HDPE sheathing, with and without helical fillets. One set of measurements was also carried out for a cable-stayed bridge with stay cables covered with a steel tube that was painted and grouted.

For the benefit of the current study, field measurements were provided for the James River Bridge (also known as Varina-Enon Bridge) in Virginia and the Indian River Inlet Bridge (Charles W. Cullen Bridge) in Delaware. The James River Bridge opened for traffic in 1990, and the Indian River Bridge opened in 2012, a 22-yr gap between the two structures. It was believed that the measurements could potentially indicate a change in the cross-sectional shape of the HDPE tube with time. The third bridge, the Chesapeake and Delaware Canal Bridge, had painted steel sheathing covering the stays. It was observed that the cross-sectional shapes of the steel tubes had a small level of eccentricity, and therefore cross-sectional data were not provided for the current study. When referring to a specific cable number in this report, the abbreviation IR is used for the Indian River Bridge, while the abbreviation JR is used for the James River Bridge.

The James River Bridge had PE tubes wrapped in weather-resistant tape, while the Indian River Bridge had HDPE tubes. From time to time, loose flaps or wrinkles in the tape would appear locally in the scans and could be filtered out. The wrapping of stay cables with tape is a practice that was adopted for ultraviolet (UV) protection of the PE tubes and has mostly been abandoned. The stay cables of the Indian River bridge have current state-of-the-art HDPE sheathing, with UV protection and helical fillets, representative of most new cable-stayed bridge construction in North America and Europe.

Data were provided from two cables from the Indian River Bridge and six cables from the James River bridge. The shape measurements were taken in intervals of 0.5 m from the deck-anchorage and over a length of the cable of roughly 9 m. Generally, there was not one prevailing shape. Many had an overall elliptical shape that was distorted in various ways. The major axis (of near symmetry) did not have a fixed location in relation to the vertical cable plane in between cables (e.g., the Indian River bridge cables in figure 15). Other cables had an overall round shape with random distortions, where no line of symmetry was seen, as shown in JRSS08 in figure 15. But the enlarged deformations can trick the eye. For stays of the James River Bridge, over the length of 9 m where measurements were taken, some tubes exhibited significant changes in shape while the shapes of other tubes remained nearly unchanged. The deviations varied between 0.17–0.63 percent diameter. There did not seem to be an influence of the sagging of the cable stay except for the cable JRSS09 (figure 15). For this cable, the shape of the PE tube started as near round with small deviations and then changed to an elliptical section with a horizontal major axis and deviations of 0.6 percent diameter.

IR Cable 113E, D=172 mm, factor 15
1%
0.5%
−0.5%
−1%
15 scans.
Scan distance:
1264–8296 mm.

IR Cable 118E, D=192 mm, factor 15
1.5%
1%
0.5%
−0.5%
−1%
−1.5%
12 scans.
Scan distance:
766–6292 mm.

JR Cable SS08, D=220 mm, factor 30
0.45%
0.3%
0.15%
−0.15%
−0.3%
−0.45%
11 scans.
Scan distance:
3178–8175 mm.

JR Cable SS09, D=221 mm, factor 30
0.6%
0.3%
−0.3%
−0.6%
13 scans.
Scan distance:
3290–9287 mm.
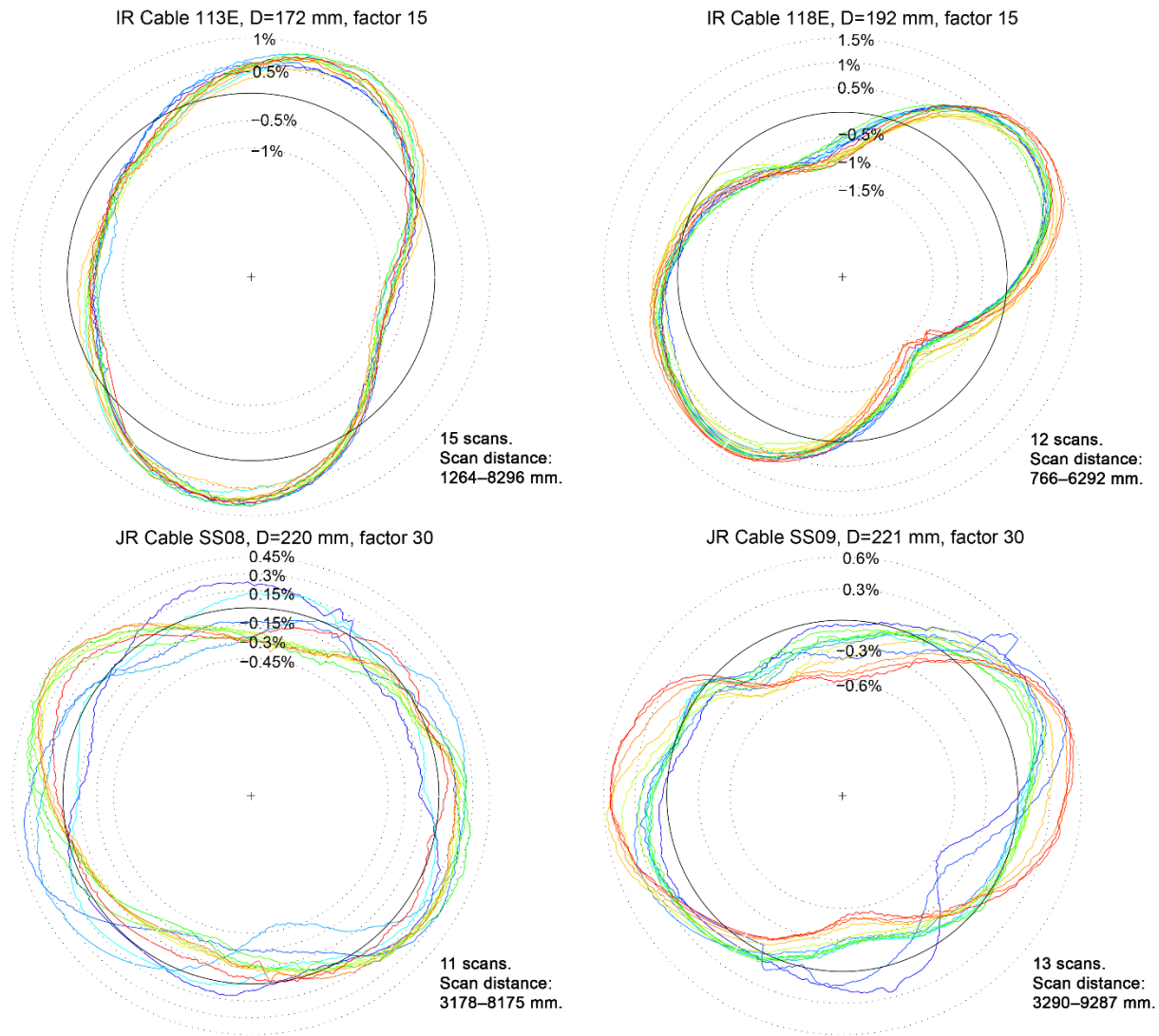
Source: FHWA.
Note: Deviations from the mean diameter are exaggerated with the factor shown for each figure. The dotted circles show the percentage-wise deviation from a circle with respect to the cable diameter *D*. The top of the images in this figure corresponds to the top surface of the stay cables in the field, looking up the cables.

Figure 15. Graph. Variations with height of the cross-sectional shapes of stay cables in service for the Indian River Bridge (top) and the James River Bridge (bottom).

For the two cables from the Indian River Bridge, deviations from a circle were larger: 0.82 percent diameter for IR113E and 1.43 percent diameter for IR118E. The cross-sectional shapes were observed to be consistent along the measured length of the tubes. This finding is significant because a consistent cross section is more likely to provide a loading mechanism that is correlated over that length of a cable, which yields a higher possibility to put the cable into motion. However, further measurements higher up on the cable stays would be of value to properly assess the consistency in cross section observed for the lower part of the stays. The protective tubes are delivered in sections, and different sections could have different cross sections. For one of the stay cables, cable JRSS10, scans were made on the adjacent tube. But the distortions along the measured length turned out to be less than 0.17 percent diameter and, thus,

not conclusive. As a result, no figure of the shape is shown in this report. Also, a bridge is in the atmospheric boundary layer, so the wind speed varies over the bridge height. As a result, the Reynolds number will vary along the length (height) of the cable. Considering the number of events of excessive cable vibration that have been recorded, the researchers in this study theorized that only a shorter consistent loading length is necessary. Also, for the cable models in this test study, the cross section was kept constant along the length of the cable. Based on the consistent cross-sectional shapes observed for IR113E and IR118E, these constant shapes can be considered representative of stay cables in service.

Two sections of stay cables from each bridge have been replicated for the model tests of this study and are shown in figure 16. For the Indian River Bridge, the percentage-wise deviations from the cable diameter were sufficiently large to be replicated for the model with a diameter of 88.9 mm. For the James River Bridge, the deformations were too small to be replicated with fidelity given the resolution of the SLS process. As a result, the magnitude of the deformations on these tubes (JRSS08 and JRSS13) were maintained as measured in the field but replicated on an 88.9-mm-diameter tube, resulting in a scaling factor of deviations of 2.5. Another model was created for section JRSS13, where the deformations were increased by a factor of 5 to examine the influence of the size of the deformations on the aerodynamic forces.

The main objective of this experimental campaign was to study the direct influence of geometrical (and not roughness) changes of the HDPE tube on the aerodynamics of the stay cables. However, currently, the majority of bridge stays are erected with a surface modification on the HDPE tube to mitigate rain/wind-induced vibrations. In Europe and the Americas, the only modification used to date are helical fillets, and two of the models have been tested both with and without helical fillets.
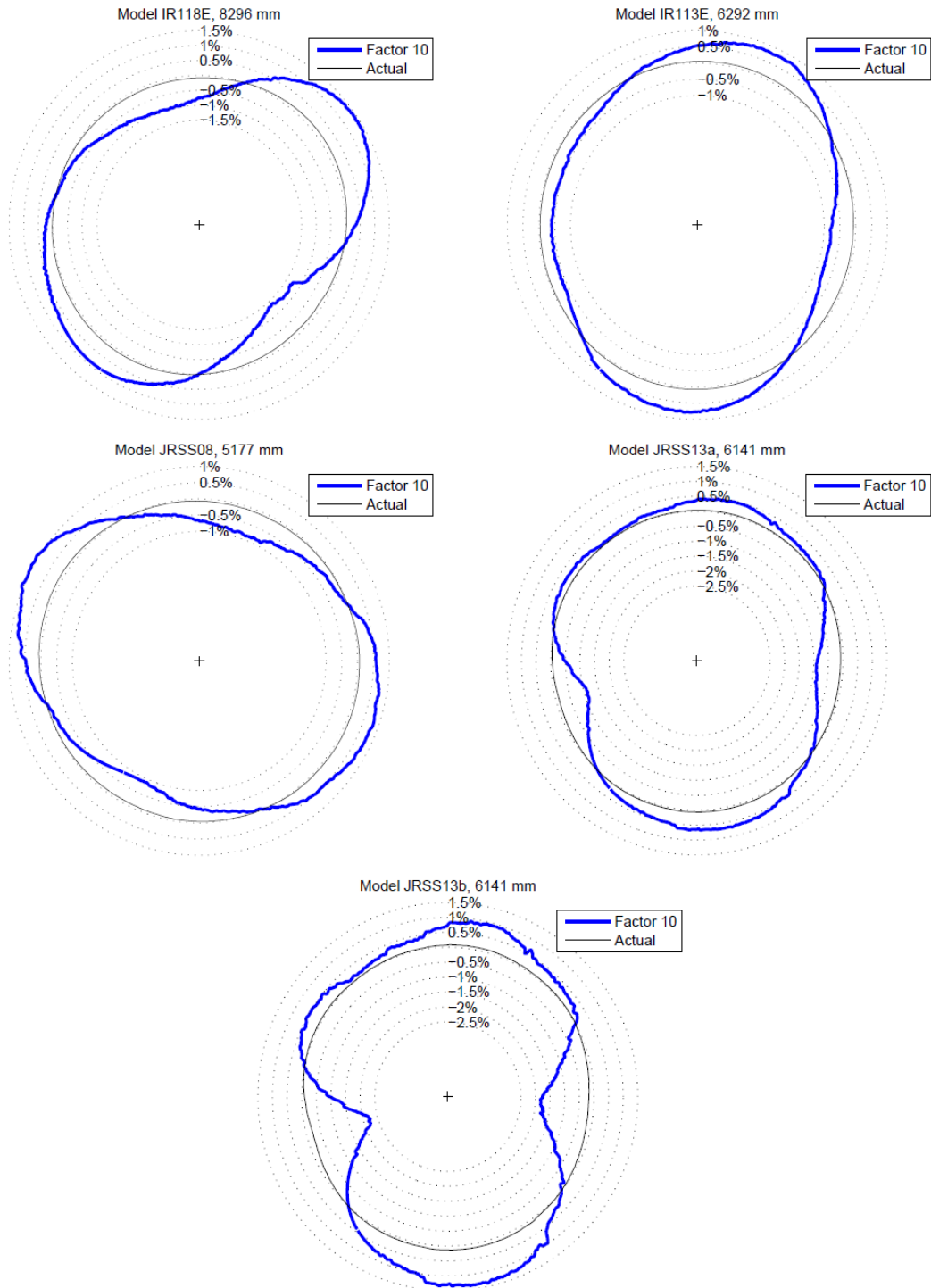
Source: FHWA.

Note: Shapes from the cables of the Indian River Bridge (top) and the James River Bridge (bottom). Deviations from the mean diameter are exaggerated by a factor of 10. The dotted circles show the percentage-wise deviation from a circle with respect to the cable diameter $D = 88.9$ mm. $\alpha = 0$ degrees for wind from the top of the page. Cable rotations are positive in the counterclockwise direction.

Figure 16. Graph. Sketch of the cross-sectional shapes selected for the experiments based on the field tests.

Cross-Sectional Shape of a Reference Cable

To complete the spectrum of cross-sectional shapes to study in this experimental campaign, the aerodynamic forces were measured on a sectional model that had the cross-sectional shape of a cable model with a known dynamic behavior and propensity for inclined cable galloping during laboratory experiments. The cable model used in the Larose and D'Auteuil experiments in 2001, 2008, and 2011—in an 8-spring dynamic rig—was considered a prime candidate for this purpose.[4]

Scans of the cable model at several sections were carried out by the researchers. This cable model is composed of an HDPE tube obtained from a bridge construction site covering a 6,700-mm long steel pipe. Its cross-sectional shape and its surface roughness are representative of stay cables in service. The cross-sectional shape of this reference stay cable (referred to hereafter as the M46 cable) is presented in figure 17.
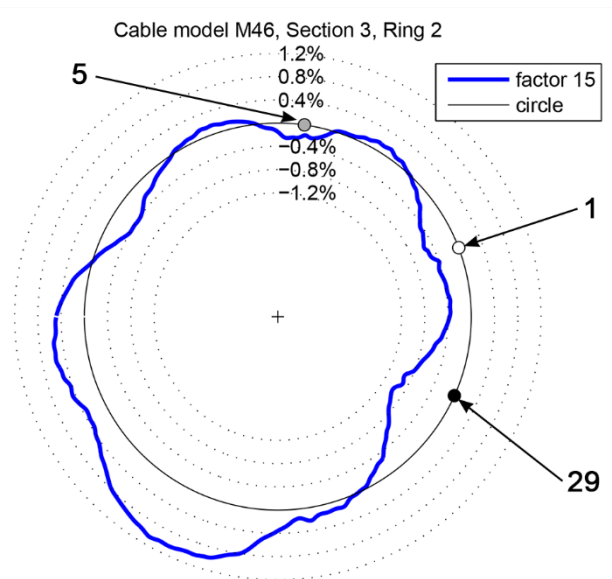
Source: FHWA.
Note: The three dots on the circumference mark the position of pressure taps: numbers 1, 5, and 29. Deviations from the mean diameter are exaggerated by a factor of 15.

Figure 17. Graph. Sketch of the cross-sectional shape of the M46 reference cable.

As for the James River Bridge cable cross sections, the deformations of the M46 reference cable were too small to be replicated on a scaled model with accuracy. The magnitude of the deformations measured on this tube with $D = 161.7$ mm was maintained for the model diameter $D = 88.9$ mm. The section that was replicated was measured at the ring of pressure taps called 'ring 2' in Larose and D'Auteuil.[4]

CHAPTER 4. EXPERIMENTAL RESULTS

TEST PROGRAM

The complete list of shapes tested in this investigation is presented in table 1.

Table 1. Cross-sectional shapes investigated. Helical fillets (HF).

Name	Section [mm]	Scale of Deviation
circle	—	1:1
3% oval	—	1:1
5% oval	—	1:1
flat face	—	1:1
M46	—	1.8:1
IR118E	8296	1:1
IR113E	6292	1:1
IR113E HF	6292	1:1
JRSS08	7675	2.5:1
JRSS13a	6141	2.5:1
JRSS13b	6141	5:1
JRSS13b HF	6141	5:1

—No value.

The measurement campaign was organized into a flow visualization campaign and three blocks of tests to systematically investigate changes in angle of attack and cable-wind angle.

- **Flow Visualization:** Surface oil flow visualizations were carried out for two models to help depict the main flow features associated with the drag crisis and the single or double bubble regime. Christiansen et al.'s paper presents the main findings of the flow visualization experiments.[8]

- **Block 1:** All shapes were taken first through the same exploratory test program, where comprehensive Reynolds number sweeps (minimum 20 points) at nine axial rotations (angles of attack) were undertaken with the setup fixed to a 60-degree inclination and 0-degree yaw, corresponding to a cable-wind angle of 60 degrees. These tests are referred to as "Block 1 tests" in the test log presented in appendix A.

- **Block 2:** The IR118E and IR113E—with and without helical fillets (HF)—were thereafter studied in detail in the Block 2 tests. The cross-sectional shapes of the Indian River Bridge stay cables were selected because they represent with accuracy the distortions measured in full-scale. The IR118E cable model has a smooth surface. Such a model represents many of the older existing bridges that have smooth stay cable surfaces without surface treatment to mitigate rain/wind-induced vibrations. The IR113E HF cable model with helical fillets represents the current prevailing aerodynamic method for mitigating rain/wind-induced vibrations. The Block 2 tests were conducted at $\theta = 60$ degrees and 0-degree yaw, corresponding to a cable-wind angle of 60 degrees. Numerous

angles of attack at small increments were tested at $\Phi = 60$ degrees, but only at five different wind speeds (see Block 2 results in appendix A).

Additional tests were carried out in turbulent flow for models IR113E HF and IR118E for a limited number of axial rotations for an inclination angle of 60 degrees. The results are also shown in appendix B.

- **Block 3:** Afterward, different cable-wind angles Φ were tested, ranging from 45 to 90 degrees in 5-degree steps. They were constructed by inclinations of 45 or 60 degrees and various yaw angles of the model, as shown in table 2. Also, a cable-wind angle of 120 degrees was included, corresponding to a full 180-degree rotation of the turntable at a 60-degree cable inclination angle. Figure 18 presents a schematic of the sign convention established for this study unless otherwise specified.
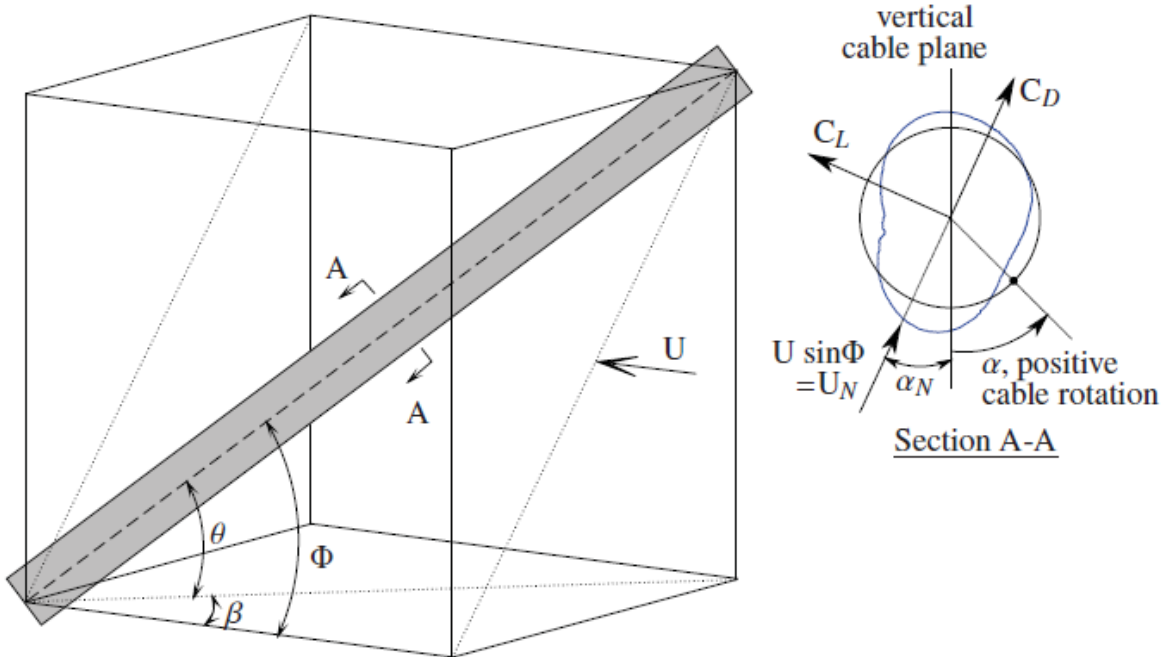
Source: FHWA.

Figure 18. Illustration. Schematic of the generic sign convention established for this study.

The cable-wind angle is defined in figure 19 as follows:

$$\cos \Phi = \cos \theta \cos \beta$$

Figure 19. Equation. Cable-wind angle.

The angle between the vertical cable plane and the wind component normal to the cable axis is defined in figure 20 as follows:

24

$$\tan \alpha_N = \tan \beta / \sin \theta$$

Figure 20. Equation. Angle between the vertical cable plane and the wind component normal to the cable axis.

In previous laboratory experimental studies to characterize the mean aerodynamic force coefficients for varying cable-wind angles on stay cables, the influence of surface irregularities had not been considered. In this study, the wind component normal to the cable axis, U_N, was directed to the same geometrical line on the cylinder cross section throughout the cable-wind angles tested to account for surface irregularities. This alignment corresponds to having the stagnation line of the normal wind component on the same physical location on the model for all of the cable-wind angles. In total, four sweeps through the cable-wind angles were undertaken, including two for the IR118E model and two for the IR113E HF model.

The test conditions for the Block 3 study are shown in table 2 and highlight the combinations of inclination angle θ, yaw angle β, and cable-wind angle Φ. The angle between the vertical cable plane and the wind component normal to the cable (α_N) for the combinations of β and θ are included in table 2.

For the IR118E model, the two geometrical points of attack of the cable that were studied corresponded to the angles of attack $\alpha' = 90$ and -100 degrees for the 60-degree inclination and 0-degree yaw. For the IR113E HF model, the two geometrical points of attack corresponded to $\alpha' = 55$ and -48 degrees at 0-degree yaw. The angle α' is the reference angle on each model to which the model was rotated to achieve the required α_N. As a result, the wind component normal to the cable axis was directed to the same geometric position on the cable for each cable-wind angle. For instance, the cable model IR118E,90° was tested at a reference angle of attack of 90 degrees which corresponded to $\alpha_N = 0$ degrees for an inclination angle of 60 degrees and a yaw angle of 0. As the cable wind angle is increased from 60 to 120 degrees, the α_N changes to ensure that the same geometric position is encountered by the wind component normal to the cable axis. The α' values for cable IR113,90° show the angle settings used to achieve the required α_N settings for each cable-wind angle.

Table 2. Test conditions for the Block 3 study, showing the combinations of inclination angle θ, yaw angle β, and cable-wind angle Φ. The angle between the vertical cable plane and the wind component normal to the cable axis is α_N.

θ	β	Φ	α_N	$\alpha'_{\text{IR118E,90°}}$	$\alpha'_{\text{IR118E,-100°}}$	$\alpha'_{\text{IR113E HF,55°}}$	$\alpha'_{\text{IR113E HF,-48°}}$
45	0	45	0	90	−100	55	−48
45	24.6	50	32.9	56.5	−133.5	22	−81
45	35.8	55	45.6	44.5	−145.5	9.5	−93.5
60	0	60	0	90	−100	55	−48
60	32.2	65	36	54	−136	19	−84
60	46.9	70	51	39	−151	4	−99
60	58.8	75	62.3	28	−162	−7	−110
60	69.7	80	72.2	18	−172	−17	−120
60	80	85	81.3	9	180	−26	−129
60	90	90	90	0	170	−35	−138
60	180	120	0	−90	80	−125	132

TESTS ON REFERENCE CROSS-SECTIONAL SHAPES

Circular Cylinder

The time-averaged aerodynamic force coefficients as a function of Reynolds number for the nominally round cylinder are shown in figure 21 for two angles of attack α. A repeatability test carried out for the 0-degree angle of attack (distinguished by the letters a and b in figure 21) showed that the measurements repeated well. Only one other rotation about the model axis was tested for the circular cylinder, which was 45 degrees. In this run, the asymmetric regime was in the same Reynolds number range as the 0-degree rotation, but the lift was directed to the opposite side and with a small reduction in value. This revealed the tendency of the separation bubble on a circular cylinder to switch sides due to the influence of small surface irregularities or changes in wind characteristics.

For comparison, figure 21 presents the mean drag coefficient from the Larose et al. 2002 experiments for $\theta = 60$ degrees and $\beta = 0$ degrees (an average of two rings of pressure taps) and the mean lift coefficient (from one ring of pressure taps).[9] Even though the 2002 experiments were performed on a different model, the results are similar. The larger drag coefficient in the subcritical Reynolds number region is most likely due to the limited nature of the measurements in a few discrete sections in rings of pressure taps rather than the entire model length. The cylinder shape was assumed to be round, and the precise cross-sectional geometry is unknown.
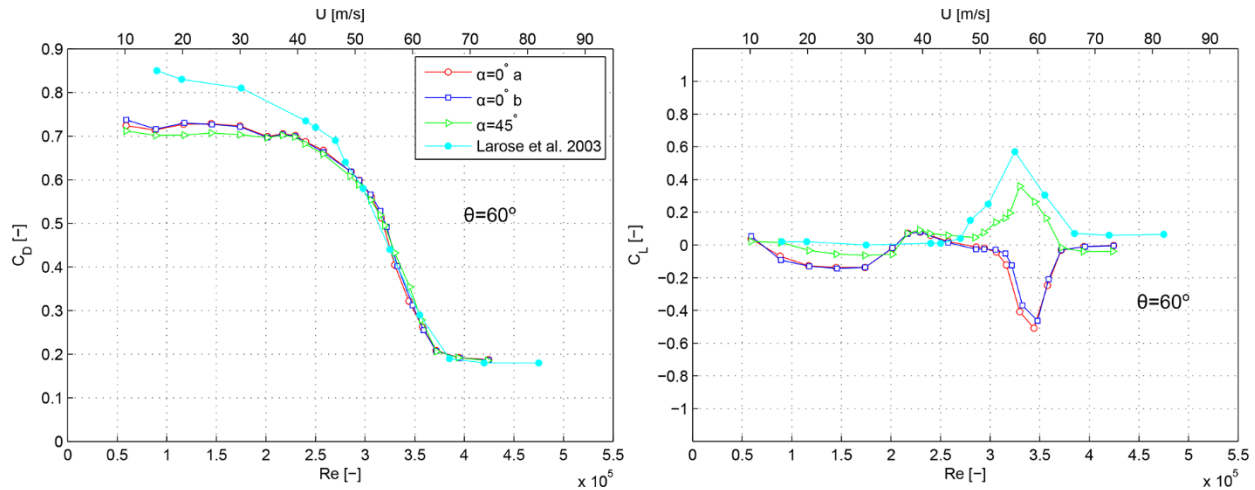
Source: FHWA.
Note: The curve "$\alpha=0°$ a" is used as the reference in this report. "$\alpha=0°$ b" was a repeatability test. The coefficients are components normal to the cable axis, and the inclination angle is $\theta = 60$ degrees.

Figure 21. Graph. Mean drag and lift coefficients as a function of Reynolds numbers and wind speeds for the circular model at different angles of attack α.

The nonzero values in lift observed at subcritical Reynolds numbers (i.e., prior to the drag crisis) have, to the authors' knowledge, not been published anywhere else in the literature, and there is no clear explanation for these results. Although both load sensors showed such development, the largest contribution came from the upper sensor, whereas the largest contribution to the lift in the drag crisis region came from the lower sensor. Subsequent experiments on the cable models representing the shapes measured by FHWA showed that the roles of the load sensors were reversed for a 180-degree yaw of the model (figure 56).

Oval Cross-Sectional Shapes

The variations of the drag and lift coefficients with respect to Reynolds number for the two oval shapes are shown in figure 22 and figure 23 for various angles of attack. The results of the tests for the circular cable model at the 0-degree angle of attack (figure 21) are shown as a reference. Many initial variations can be observed for the different angles. For the drag coefficient, these variations include the magnitude in the subcritical region, the initiation of the drag crisis, and the rate of change of drag as a function of Reynolds number. Likewise, the Reynolds number span of the asymmetric one-bubble regime in the drag crisis region varies (TrBL1 regime using Zdravkovich's nomenclature), and thus the plateau seen in the drag curves varies.[15] The sign and magnitude of the lift coefficient vary throughout the drag crisis regime.
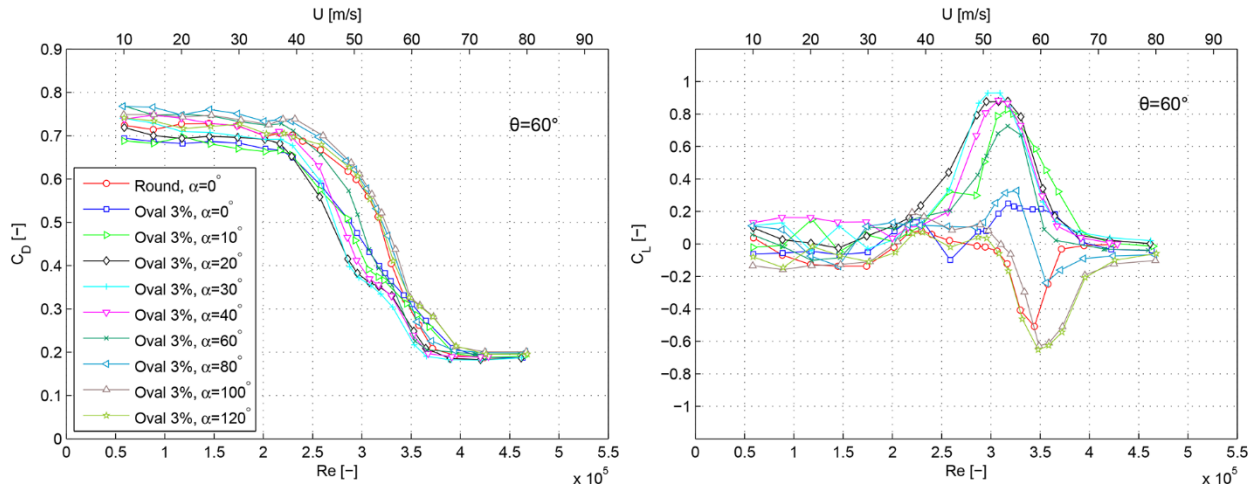
Source: FHWA.

Figure 22. Graph. Mean drag and lift coefficients for the 3-percent oval model at different angles of attack.
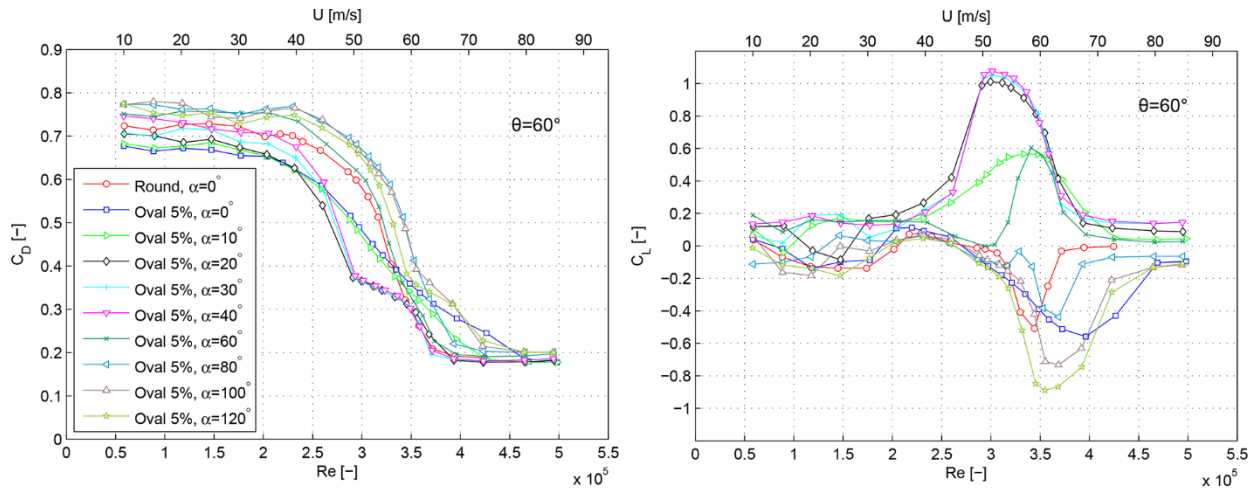
Source: FHWA.

Figure 23. Graph. Mean drag and lift coefficients for the 5-percent oval model at different angles of attack.

Individual studies of the force coefficients for each of the angles of attack are shown in figure 24. For a better comparison of the influence of the ovalization degree, the development of the force coefficients with Reynolds number is shown for three of the angles of attack in figure 24 together with the round cable.

28
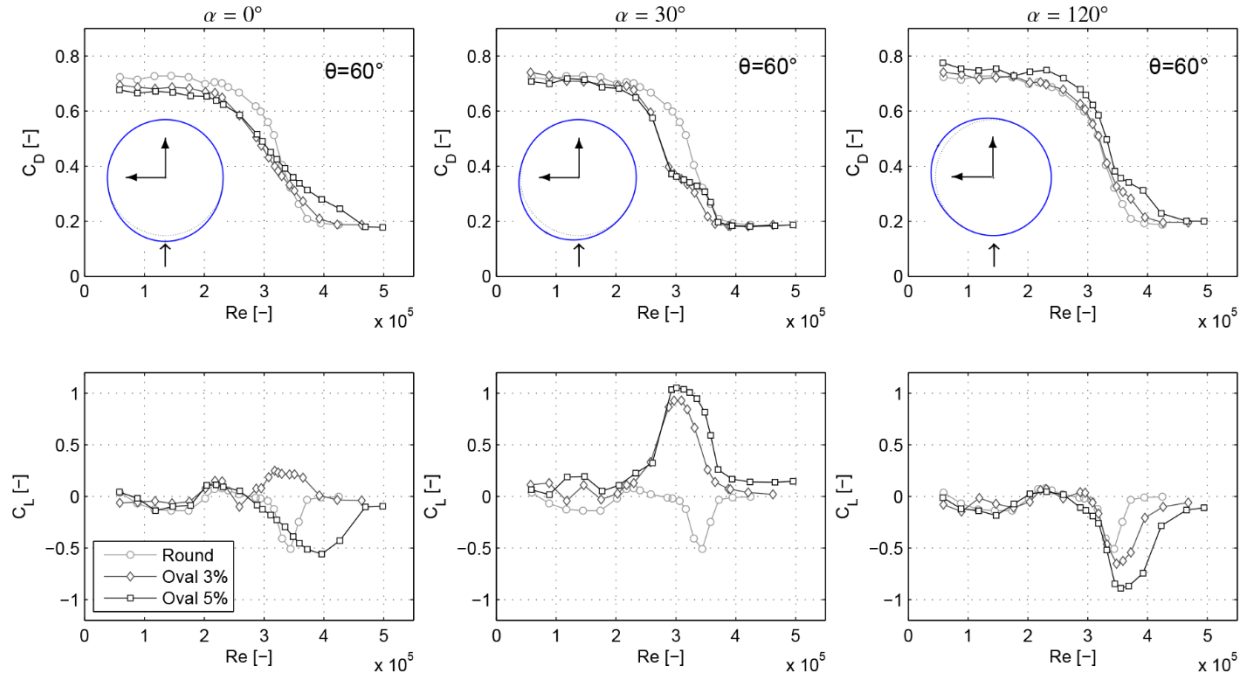
Note: The round cylinder at $\alpha = 0$ degrees is used as a reference.

Figure 24. Graph. Mean drag and lift coefficients as a function of Reynolds number for the oval cylinders at three different angles of attack α.

For $\alpha = 0$ degrees (wind normal to the head of the oval), a slower transition to the supercritical regime was seen (figure 24, left) for the drag coefficient with for increasing ovalization degree. This finding is a result of the oval models evolving toward a streamlined body. These slower transitions were also accompanied by a nonzero lift over a much wider Reynolds number range than the circular cylinder. In these cases, the direction of the lift was unpredictable due to the cylinder symmetry. Also, in the subcritical region, the drag is reducing with increasing ovalization degree. Ma et al. show that on cylinders with semi-elliptical shapes, the stagnation region reduces as the head of the profile becomes sharper, which then reduces the form drag.[16]

For the remaining rotations, the general development of the lift coefficient in the drag crisis region is first considered. Generally, when the oval head was on the upstream side (i.e., for the angles of attack of 10, 20, 30, 40, and 60 degrees), the lift was directed toward the side of the cable with the oval head. The upstream positions (20, 30, 40 degrees) also yielded the largest magnitude in lift compared with the downstream positions of the oval head. A transition occurred around 80 degrees (depending on the ovalization degree), and as the oval head was rotated further toward the downstream side (i.e., for 100 and 120 degrees), the lift was directed toward the circular side of the cable. Figure 25 and figure 26 clearly depict this phenomenon. Both show the drag and lift coefficients as a function of the angle of attack that also depends on Reynolds number. A similar development in lift with the angle of attack is found for other elongated bodies such as flat plates and airfoils, as well as the semi-elliptical sections illustrated in Ma et al.'s paper (for $Re \leq 1.78 \times 10^5$).[16] Comparing the 3- and 5-percent oval models, an increased deformation can lead to an increase in magnitude of the lift, but also a more stable asymmetric state, as shown in figure 24.
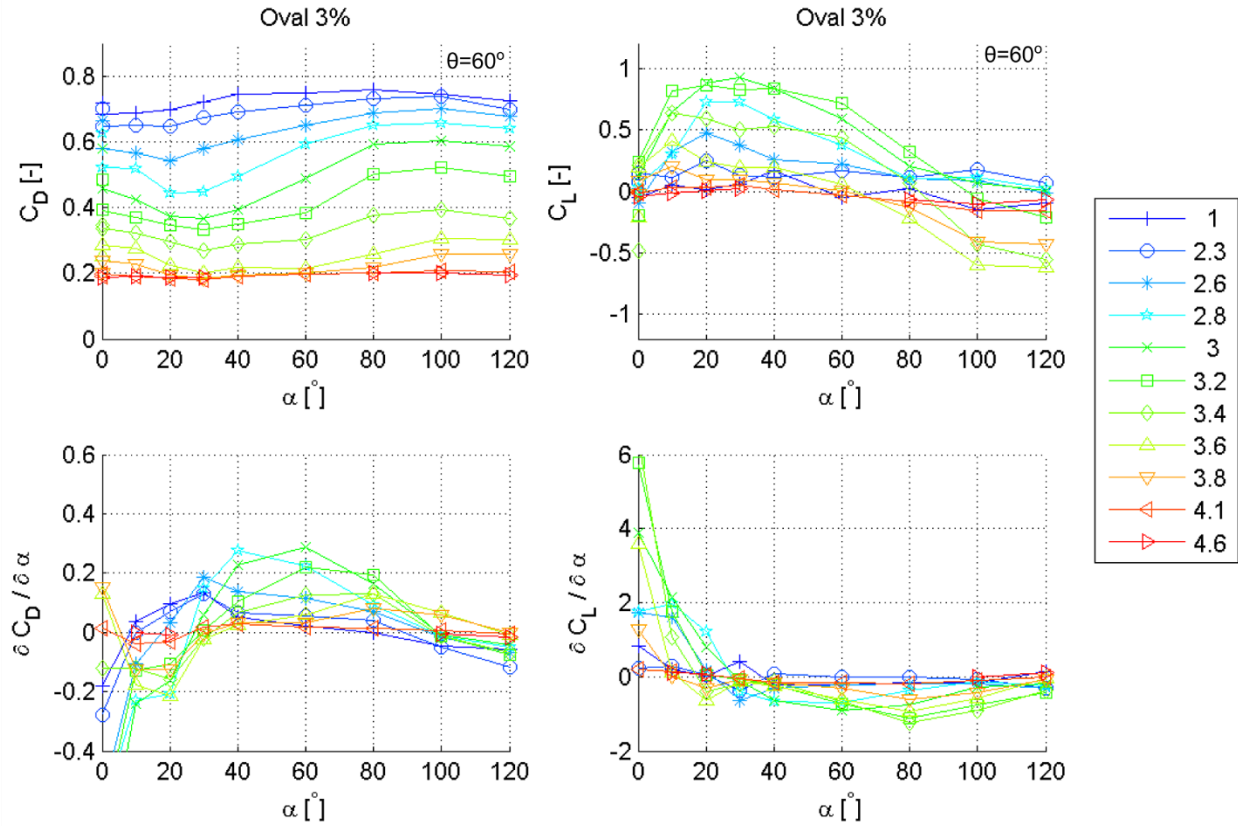
Source: FHWA.
Note: The values in the legend are ×10^5.

Figure 25. Graph. Mean drag and lift coefficients as a function of angle of attack for the 3- percent oval model at different Reynolds numbers.
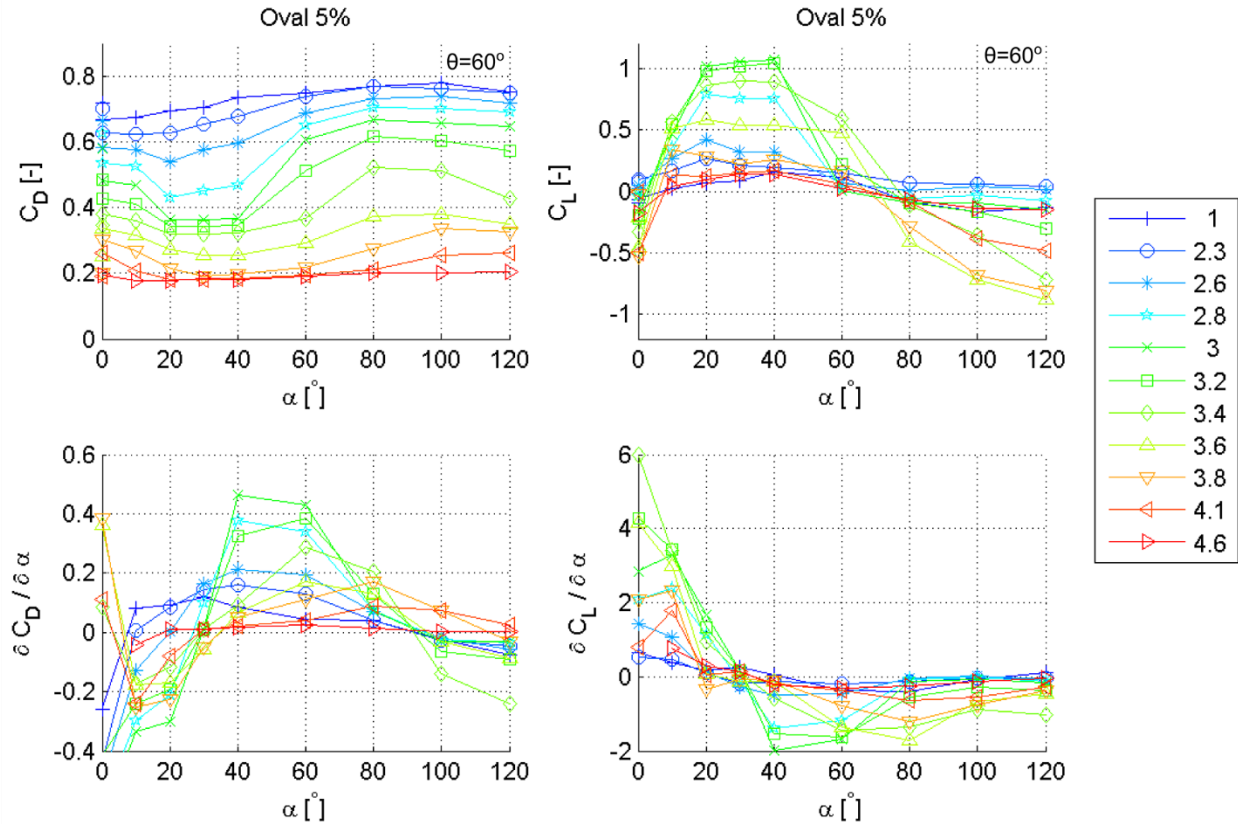
Source: FHWA.
Note: The values in the legend are ×10^5.

Figure 26. Graph. Mean drag and lift coefficients as a function of angle of attack for the 5- percent oval model at different Reynolds numbers.

Consider first the setup with the oval head on the downstream side. For the angle of attack of 120 degrees (figure 24 right), the drag crisis began at the same Reynolds number for the oval sections as for the circular section. Also, the lift force was directed toward the circular side of the cylinder. The asymmetric TrBL1 state is caused by the formation of a laminar separation bubble. At this point, laminar separation of the boundary layer occurred, followed by a transition to turbulence in the shear layer. With the increased momentum of the flow, the adverse pressure gradient was overcome, and the shear layer then reattached to the cylinder surface. This reattachment formed a closed region of recirculating flow called a "bubble." The transition from laminar to turbulent flow of the boundary layer happened undisturbed on the circular side of the cylinder.

On a nominally circular cylinder, the transition would have happened on the opposite side of the cylinder for only a small band of Reynolds number, but the oval distortion delays the transition to turbulence and allows for further development of the asymmetric state. In the asymmetric state, the increase in the ovalization degree (i.e., the further from a circular cylinder) causes a wider Reynolds number range for the asymmetric regime (i.e., the nonzero lift and the plateau in drag in figure 24, right) and an increase in the magnitude of the lift coefficient.

For $\alpha = 120$ and 30 degrees in figure 24, the plateau in drag in the asymmetric regime was decreasing as Reynolds number increased, indicating that one or both of the final separation points moved further downstream. The delay of the symmetric TrBL2 state happened because of the different positions of the locally widest geometrical points on the opposing cylinder sides combined with the surface curvature or inward bend downstream of that point. The more abrupt the inward curvature, the higher the adverse pressure gradient. The locally widest point can be found as the point tangential to a line parallel with the incoming flow. For the rotation of 120 degrees, the locally widest point on the circular cylinder half is 90 degrees counterclockwise from the stagnation point, and on the oval half, the widest point is approximately 93 and 94 degrees clockwise from the stagnation point for the 3- and 5-percent oval sections, respectively.

For the angles of attack 20, 30, and 40 degrees (figure 22 and figure 23), the widest point is first passed on the cylinder side with the oval part. Due to smaller surface curvatures downstream from this point than on the circular cylinder side (with respect to the incoming wind direction), the lift force is directed toward the oval cylinder side. This entails that the transition to the TrBL1 regime will commence at a lower Reynolds number than for a circular cylinder, which was seen to be the case. For an increasing ovalization degree, the lift coefficients increased in magnitude, and the asymmetric regime became more pronounced, see figure 24, middle for $\alpha = 30$ degrees as an example. Since the transition on the circular cable side was initiated at a higher wind speed for increasing ovalization, the ovalization degree has a global influence on the flow around the sections.

The 80-degree rotation is considered a "transition" region. For the 5-percent oval section, the adverse pressure gradient is still more severe on the oval cable side, and the lift is therefore directed toward the circular side. However, for the 3-percent oval section, where the change in curvature is not as large on the oval side, the lift is seen to change sign with increasing Reynolds numbers. The authors of this report are unable to explain this switch. One possible reason could be that the gentler curvature allows reattachment on the oval side as the Reynolds number increases, so the lift can switch sign. Another possible reason is the transition happens before laminar separation since the Reynolds number is greater.

Although $\alpha = 90$ degrees was not tested, the authors of this report speculate that the lift in the drag crisis regime would still turn toward the round cable side in this situation. At this angle of attack, the line of symmetry of the cross section is normal to the incoming wind, resulting in a larger curvature on the oval side (figure 14), and therefore a higher adverse pressure gradient.

For the oval cylinder sides, once the flow has separated, it is believed that the inward curvature of the surface, and thus the adverse pressure gradient is too strong for the shear layer to reattach at the same wind speed as the circular cylinder half. The flow needs more energy (i.e., a higher wind speed) to surpass the adverse pressure gradient and reattach. For increasing ovalization degree, a higher wind speed is needed, which would explain the increasing range of Reynolds number in which the asymmetric state is present. This relationship would be valid for bodies with smaller changes in curvature only. Higher changes would yield a pressure gradient too severe for the formation of a separation bubble but not necessarily too severe to be surmounted for a sufficiently high flow velocity. This example is seen for the flat-faced cylinder model at 60-

and 80-degree angles of attack in the next section. A similar development as described for the 120-degree rotation was also seen for the rotation of 100 degrees.

Surface pressure distributions supporting these statements can be found in Ma et al.'s paper presenting pressure distributions for a semi-elliptical cylinder with a 25-percent-diameter distortion at a 20-degree angle of attack.[16] A lobe of suction pressure is present on the oval side of the cylinder at $Re = 1.75 \times 10^5$, indicating a separation bubble in accordance with the present findings. References can also be drawn to the field of sports aerodynamics—in particular speed skating—where drag reduction was investigated by studying surface pressure distributions around the legs and arms of a mannequin.[17] The legs of an athlete and the surface of a cable have some similarities in cross section and Reynolds number regime and, in some cases, resemble the oval sections studied. Surface pressure coefficient distributions of the left ankle ($Re = 0.8 \times 10^5$) and left thigh ($Re = 1.8 \times 10^5$) in smooth flow had a suction lobe on the oval side, providing additional supporting evidence for this study's findings.

As previously shown in figure 23, for the angles of 10 and 60 degrees, the lift is still directed toward the oval side, but the behavior depends on the ovalization degree. At 10 degrees, the drag and lift coefficients for the 5-percent oval cylinder resemble the 0-degree rotation. For the 60-degree angle, the drag coefficients for the 5-percent oval cylinder were similar to the round cylinder, and the lift coefficients were similar in magnitude but had an opposite sign.

The rate of change of the force coefficients is also of interest when it comes to predicting large amplitude vibrations. These rates have been determined in MATLAB® using the grad function.[18] The change in the drag and lift coefficients with respect to the angle of attack α is most severe for the larger ovalization, figure 25 and figure 26. The drag coefficient's most critical region is for α between 10 and 20 degrees, where the drag crisis is shifted to a lower Reynolds number. At the same time, the critical region for the lift coefficient lies between an angle of attack of 40 to 80 degrees, depending on the Reynolds number, where the lift changes direction. This contribution would promote classical galloping, according to the Den Hartog criterion $C_D + \partial C_L / \partial \alpha < 0$.[19]

The rate of change of the force coefficients with respect to Reynolds number is shown in figure 27. For the angles of attack where a premature drag crisis was obtained compared with the circular cylinder, the $\partial C_D / \partial Re$ was smaller in magnitude than the circular cylinder and, therefore, less critical. Also, there was no systematic variation in the rate of change with the ovalization degree. For $\alpha = 20$, 30, and 40 degrees, the plateau in drag shown previously in figure 24 (middle) near a Reynolds number of 3×10^5 furthermore divided $\partial C_D / \partial Re$ into two peaks, as shown in figure 27 left. When the oval head was on the downstream side and the drag crisis was similar to a circular cylinder, there was no clear distinction between the rate of change of drag from a circular cylinder, as shown in figure 27 right. Generally, the 5-percent oval cylinder seemed to have a slightly steeper drag as a function of Reynolds number than the 3-percent oval cylinder for this situation. Regarding the rate of change of the lift coefficient, no direct conclusions could be drawn. A finer interval of speed variations is required to find the rate of change of the lift coefficient.
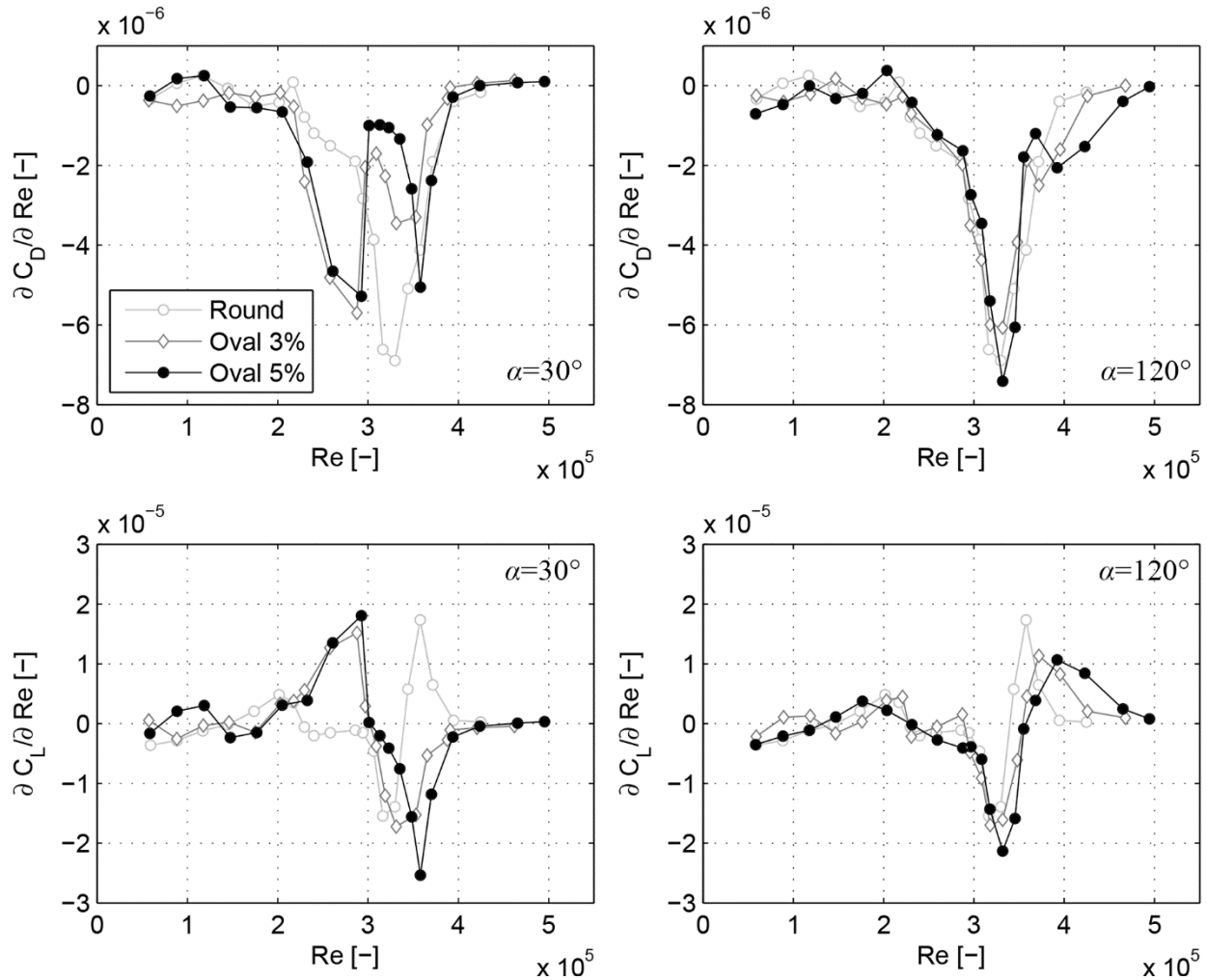
Source: FHWA.
Note: The round cylinder at $\alpha = 0$ degrees is used as a reference. Left: $\alpha = 30$ degrees. Right: $\alpha = 120$ degrees.

Figure 27. Graph. Mean drag and lift coefficients derived with respect to Reynolds number for the oval cylinders at two different angles of attack α.

In summary, the experiments on the oval models revealed that once the separation of the boundary layer had taken place, flow would reattach. Flow would then form a separation bubble on the side of the cylinder with the smallest change in curvature downstream of the laminar separation point and, therefore, the weakest adverse pressure gradient. As a result, the lift force (i.e., across-wind) would also be directed to this side.

Flat-Faced Cross-Sectional Shapes

The dependency of the mean aerodynamic force coefficients on Reynolds number for the flat-faced cylinder is shown in figure 28 for different wind angles of attack. As a reference, the mean drag and lift coefficients for the nominally circular cylinder are shown as well. Compared with the oval cylinders, the asymmetric regimes and the initiation of the drag crisis regions extend over much wider Reynolds number ranges. These results are similar to Lockwood's, who tested three flat-front cylinders with varying breadth in cross-flow.[20] Lockwood showed that the

broader the cylinder, the larger the range of Reynolds numbers over which the side force existed. The individual angles of attack will be examined in the following section to understand the aerodynamics of this shape.

Source: FHWA.

Figure 28. Graph. Mean drag and lift coefficients for the flat-faced model.

Although the shapes are different, the oval sections and the flat-faced section had certain similarities when the oval head of the oval sections and one of the rounded corners of the flat-faced section were at the same angular position from the stagnation point. For visual help, schematics of the flat-faced model at all angles of attack are shown in figure 29. When one of the rounded corners was on the upstream side but not directly upstream (i.e., for $\alpha = 10$, 20, 30, and 100 degrees), the lift was positive (corresponding to $\alpha = 10$, 20, 30, 40, and 60 degrees for the oval cylinders). When one of the rounded corners was directly upstream or near/on the downstream side (i.e., for $\alpha = 40$ and 60 degrees), the lift was negative (corresponding to $\alpha = 80$, 100, and 120 degrees for the oval cylinders). Although the rounded corner was on the upstream side for the 120-degree angle of attack, the lift was still negative, which will be explained later in this report. This change in direction and reduction in magnitude in C_L with the angle of attack can be seen in figure 30.
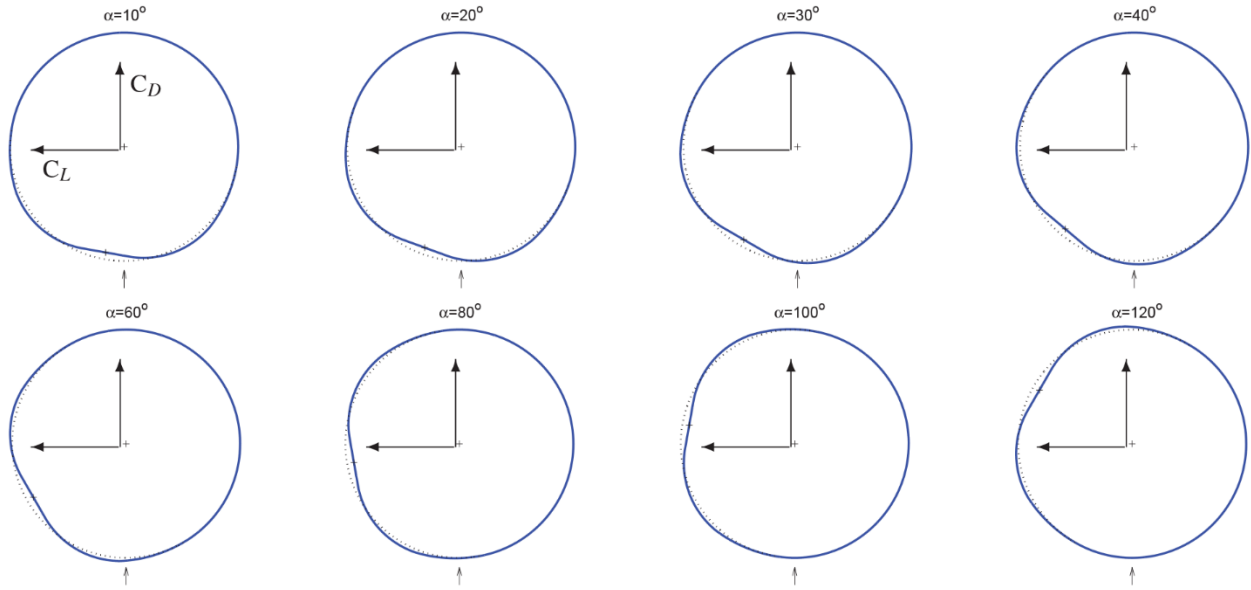
Figure 29. Illustration. Angles of attack α of the flat-faced model with sign convention.
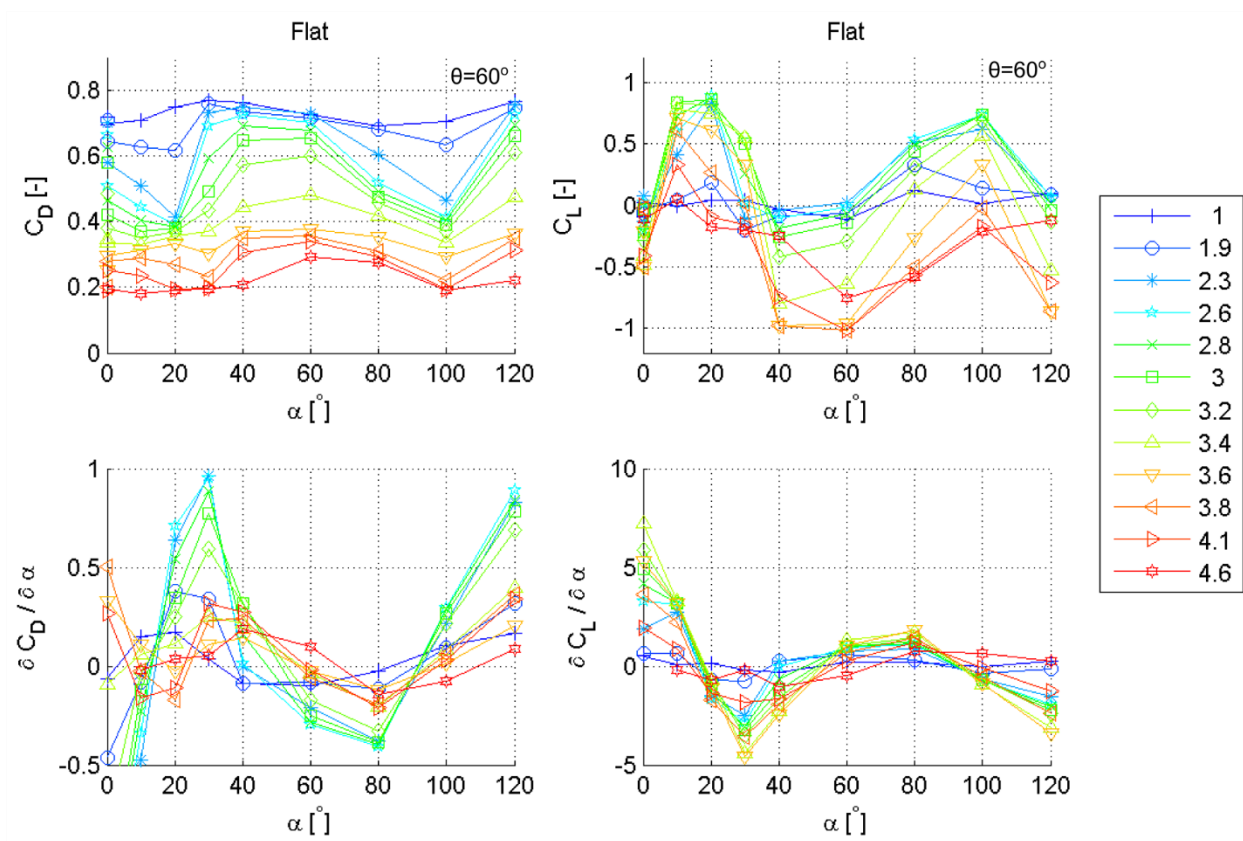
Note: The values in the legend are ×10^5.

Figure 30. Graph. Mean drag and lift coefficients as a function of angle of attack for the flat model at various Reynolds numbers.

For a 0-degree angle of attack, the flat face has a slow transition from the subcritical to the supercritical regime. The flow sees a symmetric section, and the direction of the lift force is therefore unpredictable.

Rotating the flat-faced cylinder to 10, 20, and 30 degrees, the drag crisis began at a lower Reynolds number than the circular cylinder, and the lift force was positive (i.e., directed toward the distorted side of the cylinder). As for the oval cylinders, the rounded corner on the left side introduced a maximum local width further upstream than the opposing side, causing separation of the flow at an earlier circumferential position than the opposing side.

Downstream of the laminar separation point, the change in curvature with respect to the oncoming wind direction was also smaller, forming a less severe adverse pressure gradient. The reattachment of the turbulent shear layer and, in turn, the formation of a laminar separation bubble occurred here first. The same characteristics were seen for $\alpha = 100$ degrees where the second rounded corner was at the same angular position.

For the angles of attack of 40 and 60 degrees, the lift force changed direction, and the initiation of the drag crisis occurred at the same Reynolds number as the circular cylinder. Regarding the former rotation, the locally widest points were at the same angular positions on the two sides, but the adverse pressure gradient was less severe on the circular side due to a smaller downstream curvature. Separation and subsequent reattachment, therefore, took place there first. The asymmetric regime again covered a Reynolds number range wider than the circular cylinder since a higher wind speed was needed for the flow to surmount the more severe adverse pressure gradient on the distorted cylinder side and reattach. Similar behavior was observed for $\alpha = 120$ degrees.

For the 60-degree angle of attack, the separation point on the distorted side had moved further rearward, and the adverse pressure gradient had become even higher, widening the asymmetric Reynolds number range. It is not certain that a separation bubble actually formed in this case due to the severe adverse pressure gradient.

The final angle of 80 degrees is characterized by a shift in the direction of the lift coefficient for increasing Reynolds number. It seems that at low Reynolds numbers, the flow separates at the leading rounded corner where it reattaches on the flat-faced part, creating a positive lift coefficient. Final separation would happen at the trailing corner. At higher Reynolds numbers, the flow contains more energy. The flow would overcome the adverse pressure gradient on the distorted cylinder side and remain attached until reaching the trailing corner. On the circular cylinder shoulder, separation and reattachment would now take place, causing the lift to change direction. In the Reynolds number range tested, the flow never obtained sufficient energy to overcome the adverse pressure gradient at the trailing corner by which the lift remained at a nearly constant value of −0.6.

The rate of change of the force coefficients with respect to α is seen in figure 30. As figure 30 illustrates, for drag and especially for lift, the values are larger than for the oval cylinders due to the more abrupt changes in cylinder shape encountered by the flow. The largest negative values in drag and lift, again, do not appear for the same angles of attack.

The rate of change of the drag coefficient with respect to Reynolds number for the flat-faced cylinder at α = 10, 20, 30, and 100 degrees was less critical than for a circular cylinder, as seen in figure 31, left. This was also the case for the oval cylinders with the oval head upstream. The same tendency was seen for the 80-degree angle of attack, seen in figure 31 middle. At the angles of attack of 40, 60 (cylinders with the rounded corners at an angular position between 80 to 100 degrees), and 120 degrees, the magnitude of $\partial C_D /\partial Re$ was similar to a circular cylinder, as seen in figure 31 right, with the same tendency as the oval cylinders with the oval head on the downstream side. The three shapes tested were thus equal to or less critical than the circular cylinder in this aspect. There was no clear pattern regarding the lift coefficient.
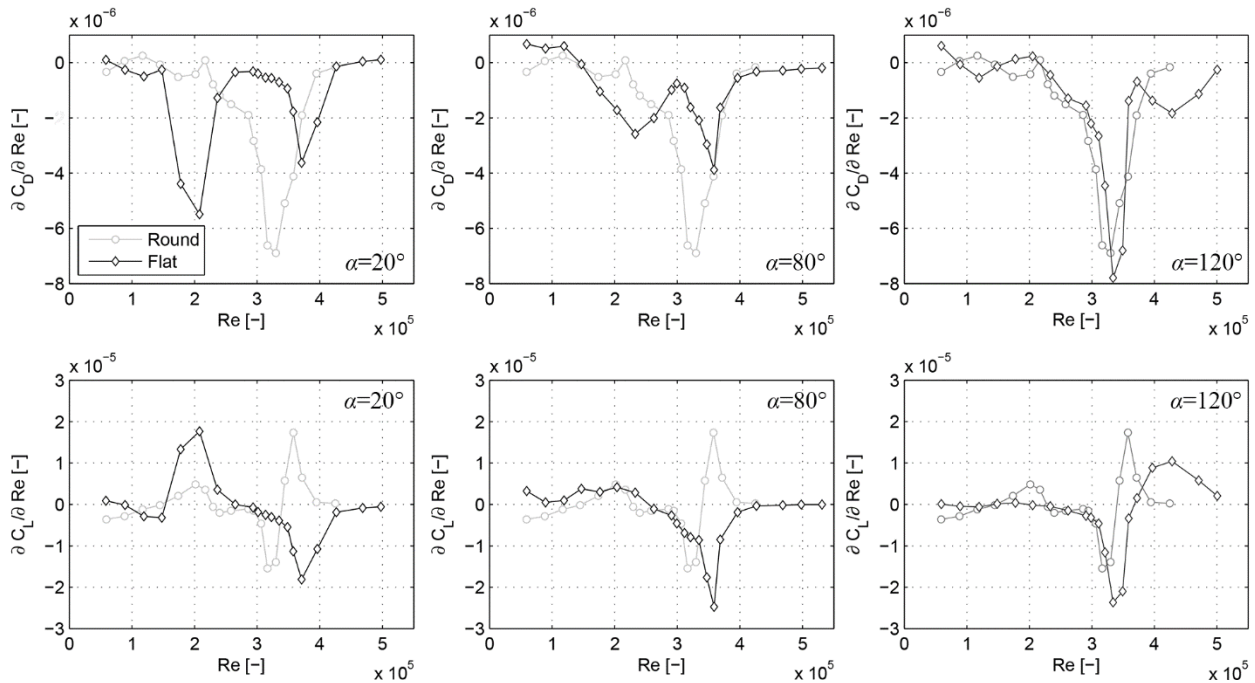
Source: FHWA.
Note: The round cylinder at α = 0 degrees is used as a reference. Left: α = 20 degrees. Center: α = 80 degrees. Right: α = 120 degrees.
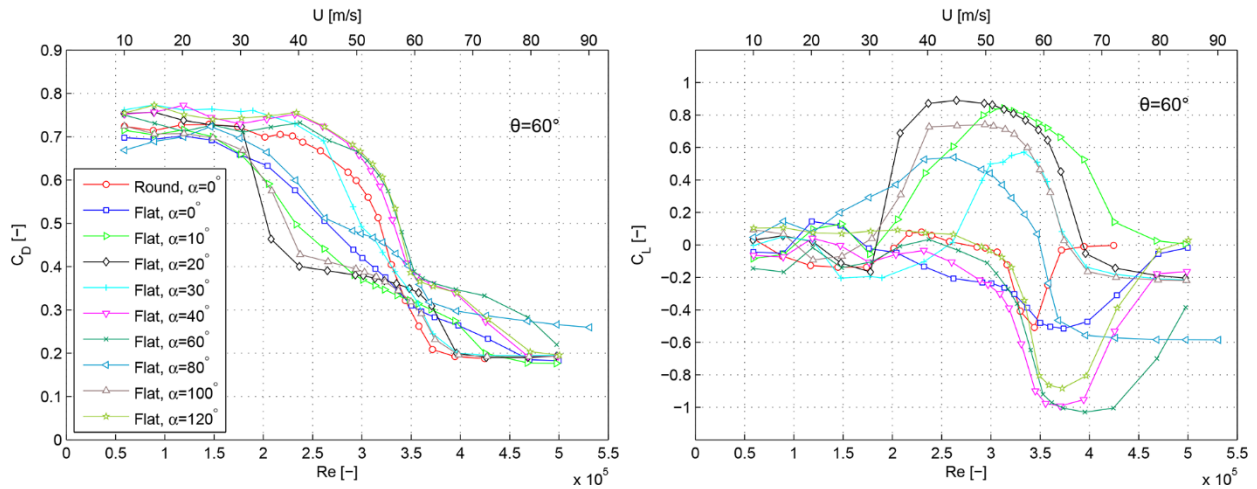
Figure 31. Graph. Mean drag and lift coefficients derived with respect to Reynolds number for the flat-faced cylinders at three different angles of attack α.

TESTS ON CROSS-SECTIONAL SHAPES OF STAY CABLES

Variable Angles of Attack for a Constant Cable-Wind Angle

The aerodynamic force coefficients with respect to Reynolds number will be compared with the drag and lift of the round cable model presented in the previous section on reference tests of circular cylinders. When the variation of the force coefficients is shown with respect to Reynolds number, the wind speed axis is purely indicative, as the kinematic viscosity is different for each run.

Smooth Cable

In the first series of experiments of this study (Block 1), the cable models were fixed at an inclination angle of 60 degrees, and the yaw angle was kept at zero degrees. Nine different angles of attack (i.e., axial rotation) were tested for each model.

The variation of the time-averaged aerodynamic force coefficients with Reynolds number for the cable models of the Indian River Bridge is shown in figure 32 and figure 33 for IR118E and IR113E, respectively. The results displayed a high dependency on the angle of attack of the cable model. There was a wide distribution in the initiation of the drag crisis region as well as for the magnitude of the lift coefficient in the asymmetric one-bubble regime. The largest magnitude of the lift coefficient was 1.06 for IR113E at $\alpha = 100$ degrees (i.e., nearly three times larger than the drag coefficient). At this angle of attack, the Reynolds number range containing the asymmetric regime extended, resulting in a wide plateau of the drag coefficient. This result occurred because the positive (i.e., adverse) pressure gradient downstream the point of laminar separation of the boundary layer must have been more severe on one side of the model than the other. Hence, the formation of the second laminar separation bubble took place at a much higher Reynolds number than for the first bubble. This result allowed for the further existence of the asymmetric regime compared with the extent and magnitude observed for the nominally circular model.
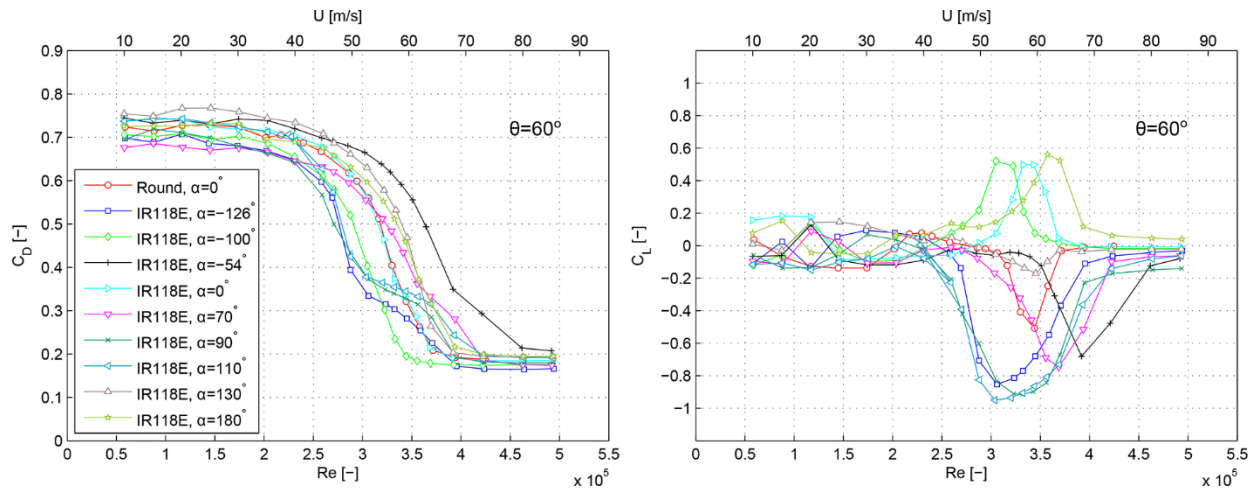
Source: FHWA.

Figure 32. Graph. Mean drag and lift coefficients for IR118E.
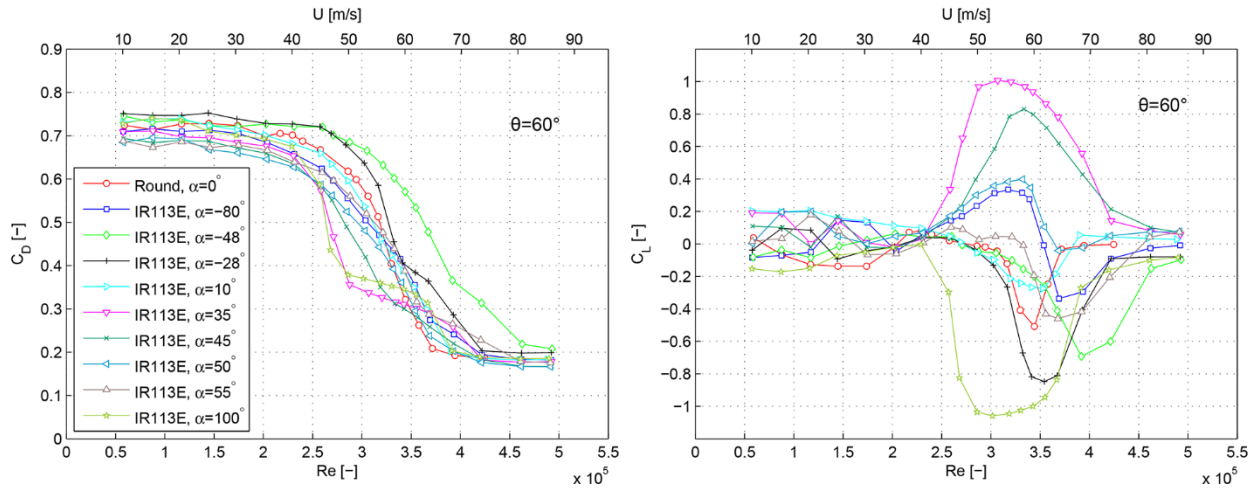
Source: FHWA.

Figure 33. Graph. Mean drag and lift coefficients for IR113E.

Although the surface distortions were less than 1.5-percent-diameter for these cables, the direction of the lift in the asymmetric regime was not random, and gradual changes between positive and negative lift were observed. An example is shown in figure 34 for IR118E. The aerodynamic forces were measured at fine increments of angles of attack but only at a few wind speeds sufficient for this purpose. For an increasing angle of attack, the lift changed from negative to positive. A change in lift of 0.6 was, for example, achieved within a 2.5-degree increment between $\alpha = 127.5$ and 130 degrees at $Re = 3.7 \times 10^5$, and a change of 0.7 within a 1.5-degree increment between $\alpha = 132.5$ and 134 degrees at $Re = 3.4 \times 10^5$.

Source: FHWA.

Figure 34. Graph. Mean lift coefficients for IR118E and direction of lift for two angles of attack.

An explanation for these changes in lift can be found in the results of the tests on the oval cylinders. Take the angle $\alpha = 135$ degrees sketched in figure 34. The local widest points were positioned at nearly the same angular position. Downstream of these points, the change in curvature with respect to the oncoming wind direction was smaller on the left side, indicating a

40

less severe adverse pressure gradient. After laminar separation, less energy was thus needed in the separated shear layer for reattachment to occur. The first laminar separation bubble, therefore, formed on this side, creating a positive lift. For $\alpha = 125$ degrees, the local widest point was located on the right-hand side and was far upstream compared to the opposite side. On the right side, the adverse pressure gradient was smaller, and the first laminar separation bubble was established on this side, changing the direction of lift.

A similar trend is depicted for model IR113E in figure 33 between the angles of attack of 35, 45, 50, and 55 degrees. However, in this case, the explanation related to the cylinder shape was not obvious. For this cable model, it was impossible to predict the direction of the lift for the majority of rotations. Therefore, either the deformations were too small to use the same reasoning as for the oval cylinders, or some small disturbances invisible to the naked eye were present on the surface.

Based on the quasi-steady theory formulated by Macdonald and Larose, for the angle of attack to become significant in respect to dry inclined cable galloping, the cable surface geometry will be positioned such that a small change in the angle of attack leads to a significant change in the magnitude of the adverse pressure gradients.[21] For the smooth models, a change in relative angle of attack can disrupt or delay (with respect to wind speed) a laminar separation bubble or change the side of the cable where the first bubble will form.

The drag and lift coefficients for the smooth IR118E model are shown in figure 35 as a function of the angle of attack, along with their derivatives. The x-axis was selected to match the definition by Den Hartog, positive angles of attack in a clockwise direction.[19] The "gradient" function in MATLAB was used to determine the derivatives.[18] The angles of attack were selected as the wind-tunnel testing progressed to find the angles yielding the largest changes in forces.
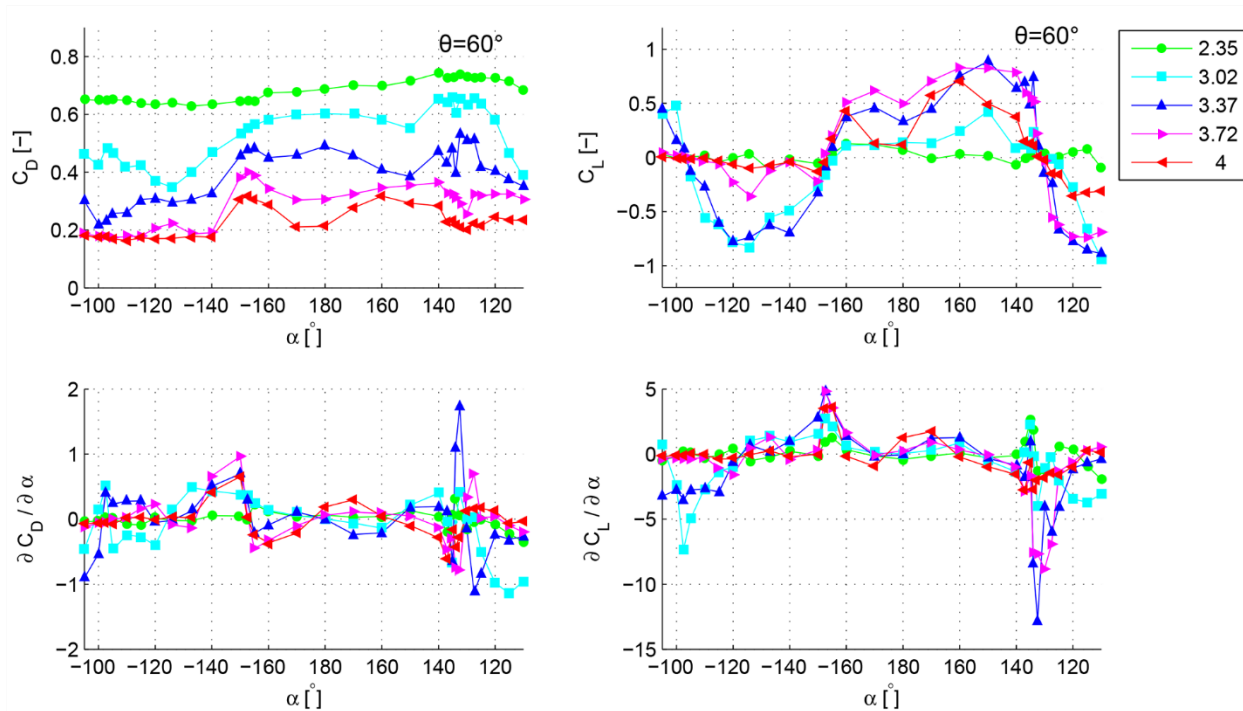
Source: FHWA.
Note: The values in the legend are $\times 10^5$.

Figure 35. Graph. Mean drag and lift coefficients as a function of angle of attack for IR118E from $\alpha = -95$ to 110 degrees at various Reynolds numbers.

The derivative of lift with respect to α is important with regard to galloping. According to the classical Den Hartog galloping criterion for a cylinder in cross-wind, the system becomes unstable when $C_D + \partial C_L/\partial \alpha < 0$.[19] For the IR118E cable model, the largest magnitude of $\partial C_L/\partial \alpha$ was -12.7 for $\alpha = 132.5$ degrees at $Re = 3.37 \times 10^5$. This value was significantly larger than the drag coefficient. The value was found in the one-bubble regimes described in relation to figure 34, where the lift changed abruptly from positive to negative. At this angle and Reynolds number, the cable would be prone to wind-induced vibrations.

According to the Post-Tensioning Institute's (PTI) design recommendations of stay cables, section 5.2.3.3, a requirement exists to calculate the minimum structural damping necessary with respect to galloping related to ice accumulation.[1] For this equation, the PTI suggests a typical value of $\partial C_L/\partial \alpha$ to be approximately -2.0. Values in that range were reported elsewhere. The possibility of what is termed inclined galloping of dry inclined cables is also recognized in the recommendations. However, the PTI guidelines suggest that one should consult the latest experimental findings about this phenomenon since it is not fully understood. In light of the findings in this report, a higher value of the $\partial C_L/\partial \alpha$ parameter should be considered (could be as high as -13) since the findings reported here were obtained directly from the geometry of a stay cable measured in-situ.

Surface irregularities still proved influential in turbulent flow with $I_u = 1.7$ to 2.0 percent for IR118E (figure 54). For the angles of attack tested, the lift force was directed to the same side as

42

in the smooth flow case, and the sequence in which drag varied remained (e.g., largest drag coefficient for $\alpha = -54$ degrees).

To depict the influence of amplified deformations, the aerodynamic force coefficients for the models JRSS13a and JRSS13b are shown in figure 36 and figure 37, respectively. The deformations of JRSS13b were twice the size of the deformations of JRSS13a. The overall variation with Reynolds number was maintained when increasing the deformations. For the angles of attack with a low rate of change in drag for model JRSS13a (e.g., $\alpha = -36$ and 20 degrees), the rate of change became even smaller when increasing the deformations. For all α, the asymmetric regime extended over a longer Reynolds number range for JRSS13b, and the magnitude of lift either increased or decreased depending on α. Considering that the distortions of the JRSS13a cable model were already 2.5 times larger than the original cable deformations (table 1), the asymmetric regimes of the true shape were expected to be of shorter extent and with steeper drag crises. However, one of the authors of this report has become aware that ovalization tolerances of 10 percent of the average diameter of the HDPE tubes are accepted on-site. Cable deformations up to 5 percent diameter (as for JRSS13b) could be found in the field. As a result, the force coefficients can cover a wide envelope of magnitudes, as seen in figure 37. A significant systematic drop in lift as reported for the Indian River Bridge cables was also seen for both JRSS13a and b between the angles of attack 160, 170, and 180 degrees.
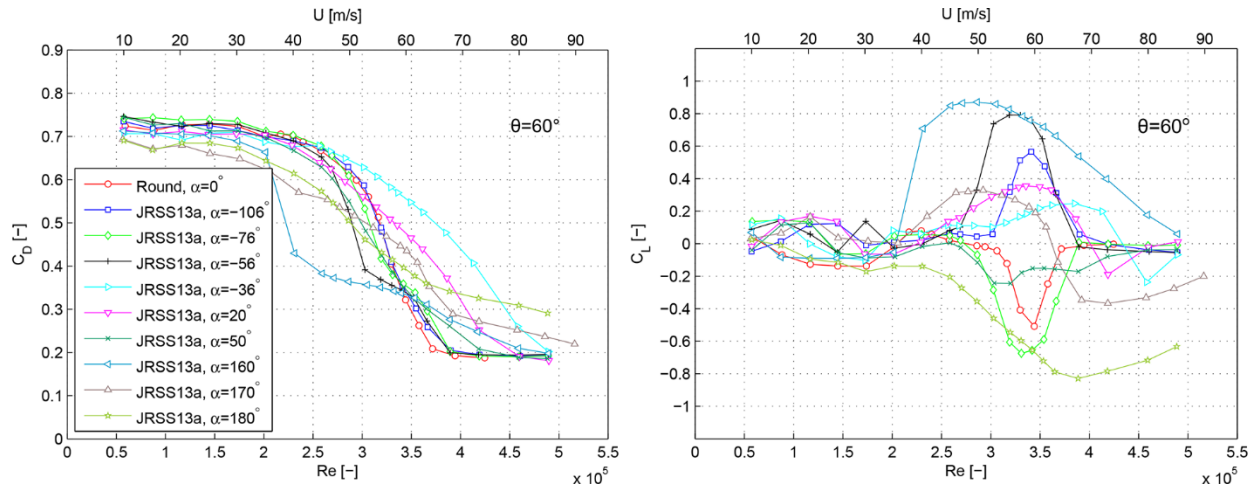
Source: FHWA.

Figure 36. Graph. Mean drag and lift coefficients for JRSS13a.
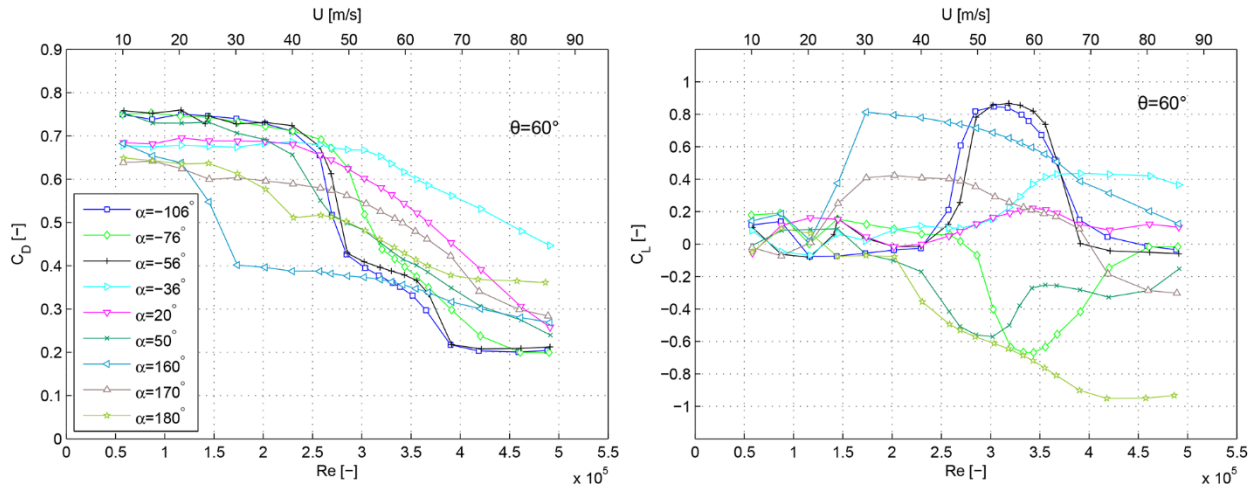
Source: FHWA.

Figure 37. Graph. Mean drag and lift coefficients for JRSS13b.

The variation of the time-averaged aerodynamic force coefficients with Reynolds number for the reference stay cable (M46) and JRSS08 cable models are shown in figure 38 and figure 39, respectively.
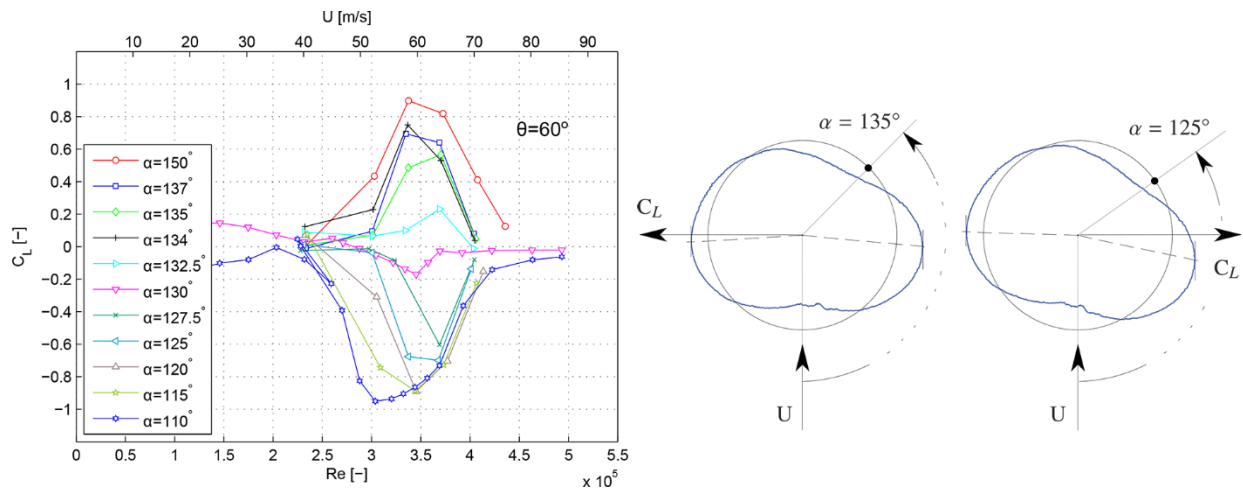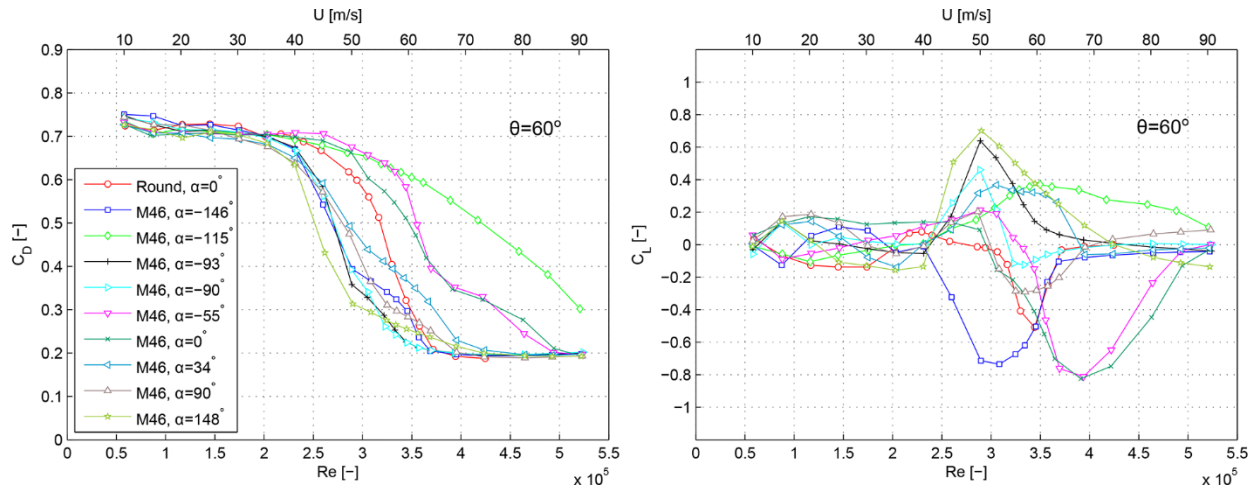

Source: FHWA.

Figure 38. Graph. Mean drag and lift coefficients for M46.
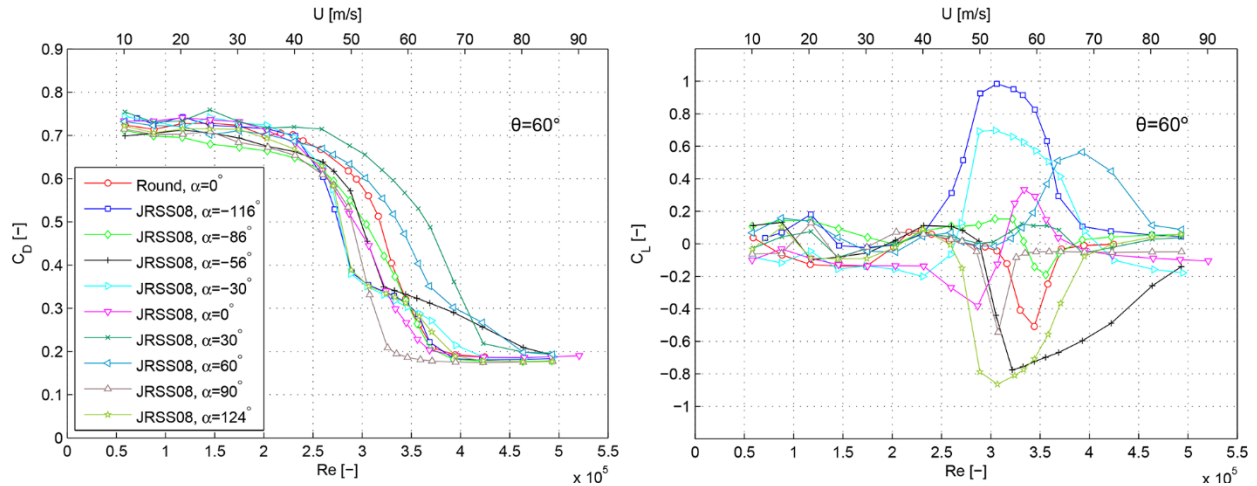
Source: FHWA.

Figure 39. Graph. Mean drag and lift coefficients for JRSS08.

Cable with helical fillets

For the cable model IR113E HF, the same angles of attack were tested as for the smooth model for direct comparisons of the aerodynamic force coefficients. For JRSS13b HF, only a few angles were studied. The time-averaged drag and lift coefficients are shown in figure 40 and figure 41. The drag crisis was displaced to a lower Reynolds number for this model setup, and the supercritical value in drag is higher than for the smooth cable, as reported by Larose and D'Auteuil.[4] Also, the peak lift coefficient was reduced in the critical Reynolds number regime. At high Reynolds numbers, the lift coefficient was observed to be two to three times greater with the helical fillet than for the smooth IR113E cable.
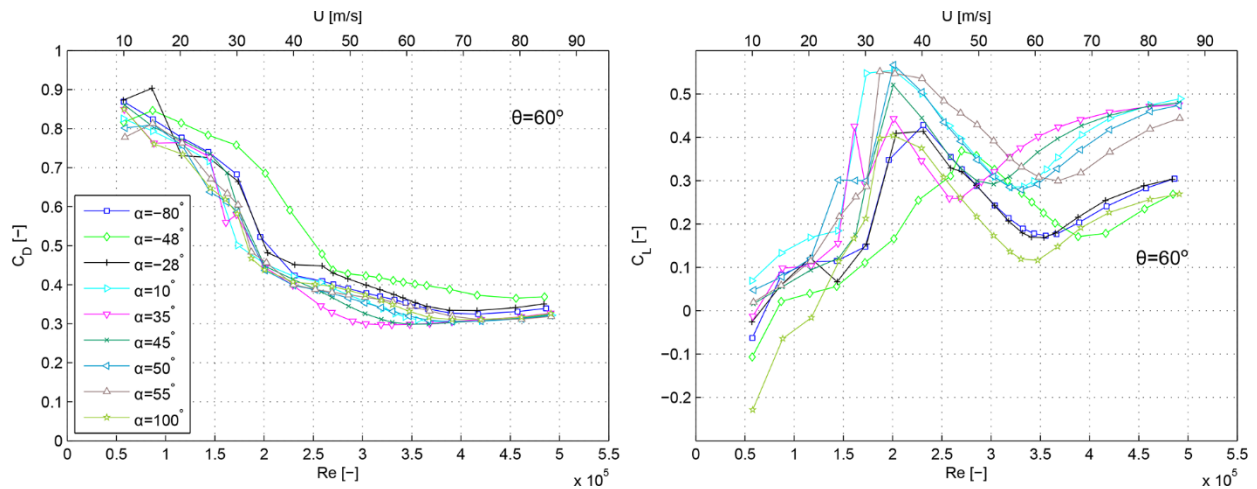
Source: FHWA.
Note: Different scale than figure 33.

Figure 40. Graph. Mean drag and lift coefficients for IR113E HF.
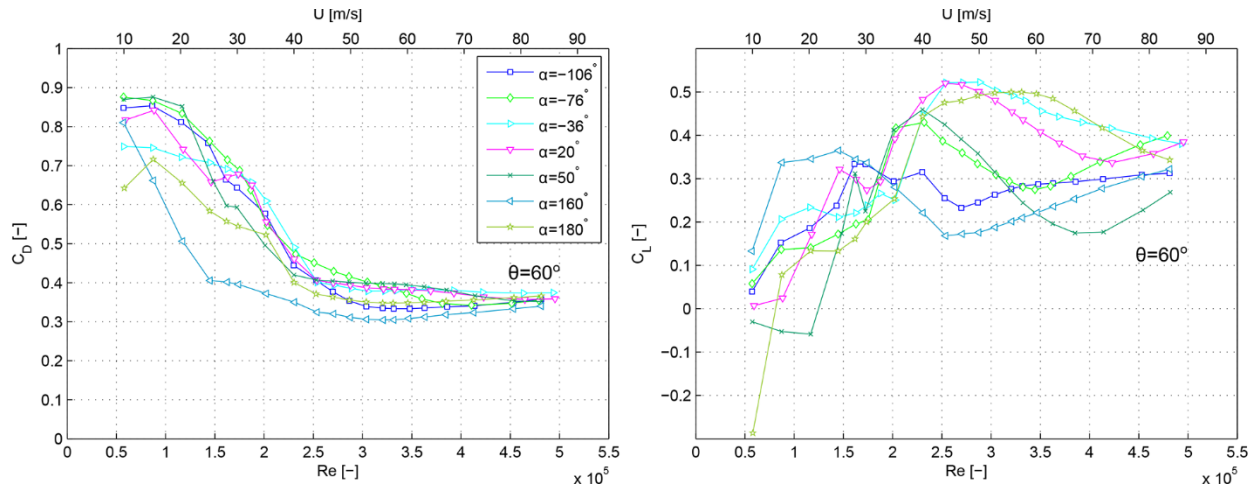
Source: FHWA.
Note: Different scale than figure 37.

Figure 41. Graph. Mean drag and lift coefficients for JRSS13b HF.

When a cable with double helical fillets is inclined to the flow, the helical fillet will, on one side of the cable, be nearly aligned with the flow and, on the other side of the cable, be nearly normal to the flow. Henceforth, this report will refer to the cable sides as the smooth and the rough cable sides, respectively. At lower Reynolds numbers, the direction of the total lift in figure 40 and figure 41 appeared random. For larger Reynolds numbers, the lift was found to be positive. It was directed toward the side of the cable with the helical fillet nearly parallel to the flow. Based on surface oil visualizations, the flow on the smooth cable side appeared to be similar to that on a smooth cylinder, and a laminar separation bubble formed when the boundary layer underwent a transition. Therefore, even for cables with helical fillets, one may describe a critical Reynolds number region. Although the lift had a span-wise variation, the helical fillet nearly normal to the flow disturbed the flow sufficiently, so the local lift on this side remained smaller than on the opposite smooth side.[22]

However, most importantly, even for cables with helical fillets, the force coefficients are dependent on the angle of attack, although the variations are not as large as for the smooth cylinder. Taking IR113E HF as the example, the surface distortions were seen to have an influence, as some of the characteristics prior to adding the helical fillet can be seen from figure 32 to figure 39. For example, the drag coefficient remained the highest for $\alpha = -48$ degrees and the lowest for $\alpha = 35$ degrees. In between, the drag was, however, somewhat unstructured. Regarding the lift coefficient, the minimum lift in the valley at higher Reynolds numbers was also related to the asymmetric regimes for the cable without helical fillets. This result is, however, not surprising since the smooth side of the cable, as just mentioned, behaved largely as a smooth cylinder.

When a laminar separation bubble on the smooth cable forms on the same side as the cable with helical fillets, the lift in the valley in figure 40 started increasing with Reynolds number. If the lift was positive in figure 33, it meant that the first laminar separation bubble on the smooth cable formed on the same side as for the cable with helical fillets. Therefore, the lift increased from the valley in figure 40 at the same Reynolds numbers the asymmetric regime began in

46

figure 33 (e.g., $\alpha = 35$ degrees for $Re > 2.6 \times 10^5$). If the lift was negative in figure 33, the first bubble on the smooth cable formed on the opposite side. Not before the second separation bubble started to form on the smooth cable did the lift in figure 40 increase from the valley (e.g., $\alpha = 100$ degrees for $Re > 3.5 \times 10^5$). So, at least on the smooth cable side, the behavior of the boundary layer and the influence of the cylinder shape distortions are largely maintained. The flow features associated with the presence of the helical fillets were studied through surface oil flow visualization experiments during this investigation, reported by Christiansen et al.[8]

The derivatives of the lift coefficients with respect to α are presented for IR113E and IR113E HF in figure 42 for the angles of attack where full Reynolds number sweeps were carried out. The derivatives show that the cable with helical fillets outperformed the smooth cable, with the magnitude of $\partial C_L / \partial \alpha$ being reduced. Although the increments of angle of attack were generally too large for a full assessment, the angles of attack 55, 50, and 45 degrees with only a 5-degree increment could be expected to show reliable trends.
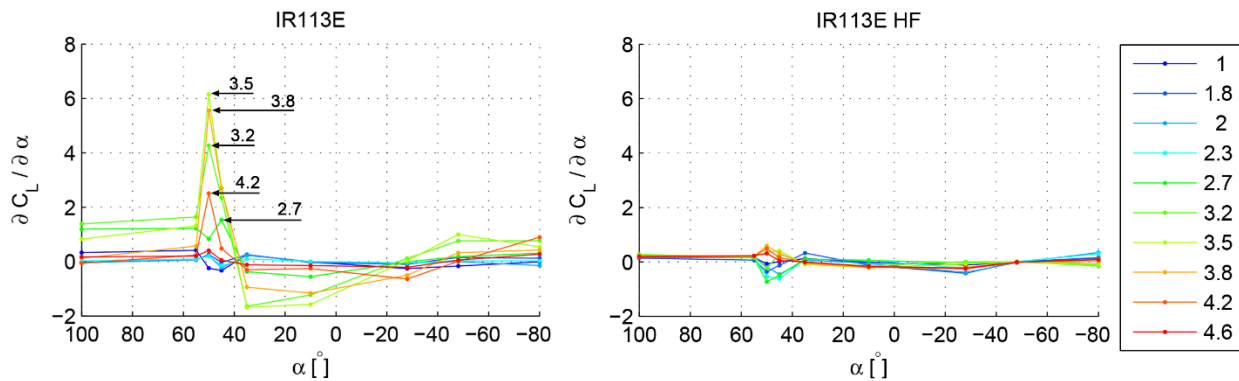
Source: FHWA.
Note: The values in the legend are $\times 10^5$.

Figure 42. Graph. Mean lift coefficient derivatives as a function of angle of attack for IR113E and IR113E HF from $\alpha = 100$ to -80 degrees at various Reynolds numbers.

However, when observing the force coefficients for IR113HF for the fine angle-of-attack increments in figure 43, the cable with helical fillets did not necessarily exhibit superior performance. For this cable model, the lift was highly sensitive to the angle of attack at lower Reynolds numbers, in particular within the range $\alpha = 45$ to 65 degrees. The large changes in the lift coefficient were recorded at Reynolds numbers of 1.85×10^5 and 2.05×10^5 before the formation of the laminar separation bubble based on the results for the smooth cable (figure 33). The time series of the lift coefficients in this Re range revealed boundary layer instabilities in the form of jumps in between semi-stable states. They were seen at $\alpha = 64$, 63, 55, and 49 degrees, but not for 65, 61, 59, 52, and 50 degrees; at least not within the 60-s sampling period. At the low Reynolds numbers, the boundary layer was thus considered to be unstable. The cause of the boundary layer instabilities was unclear, but it can be associated with the presence of the helical fillets.
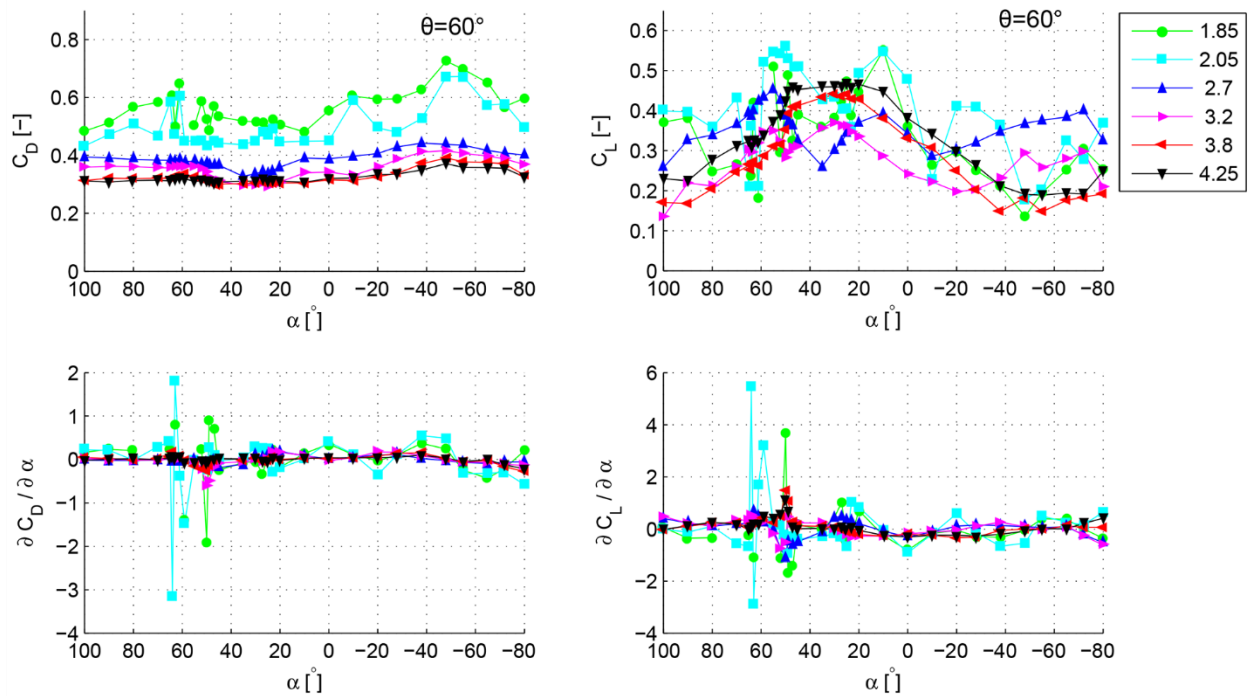
Source: FHWA.
Note: The values in the legend are $\times 10^5$.

Figure 43. Graph. Mean drag and lift coefficients as a function of angle of attack for IR113E HF from $\alpha = 100$ to -80 degrees in fine increments at various Reynolds numbers.

Variable Cable-Wind Angles for a Fixed Angle of Attack

The following investigation was carried out for cable models IR118E and IR113E HF. In previous laboratory experimental studies to characterize the mean aerodynamic force coefficients for varying cable-wind angles on stay cables, the influence of surface irregularities has not been accounted for (i.e., the cylinders have been assumed perfectly round). For cable models with HDPE tubes, only a handful of studies have been carried out for smooth cables and cables with helical fillets or pattern indentation. The outcome of these studies were graphs of drag and lift coefficients as a function of cable-wind angles and Reynolds number that are the data needed to predict propensity to wind-induced vibrations with a quasi-stationary model. However, the trends that could be depicted from these graphs could have been different if the angle of attack of the cable model would have been kept constant for all wind-cable angles.

The test program of the current study addressed this issue. In the following series of tests, the wind component normal to the cable axis U_N was directed to the same geometrical line on the cylinder cross section throughout the cable-wind angles tested. In total, four sweeps through the cable-wind angles were undertaken: two for the IR118E model and two for the IR113E HF model. For the IR118E model, the two geometrical points of attack of the cable that were studied corresponded to the angles of attack $\alpha = 90$ and -100 degrees for the 60-degree inclination and 0-degree yaw (figure 32). For the IR113E HF model, the points of attack corresponded to $\alpha = 55$ and -48 degrees (figure 40).

48

The results for the smooth IR118E model are shown in figure 44 and figure 45. As expected, the drag drops with decreasing cable-wind angle Φ. The results in figure 44 for the benchmark angle of attack of 90 degrees at a 60-degree inclination angle display a systematic decrease in the magnitude of lift in the single-bubble regime for decreasing Φ. This result is in accordance with findings by Bursnall and Loftin showing that for increasing yaw angles, the separation bubbles were less defined and did not form for yaw angles greater than or equal to 45 degrees.[23]
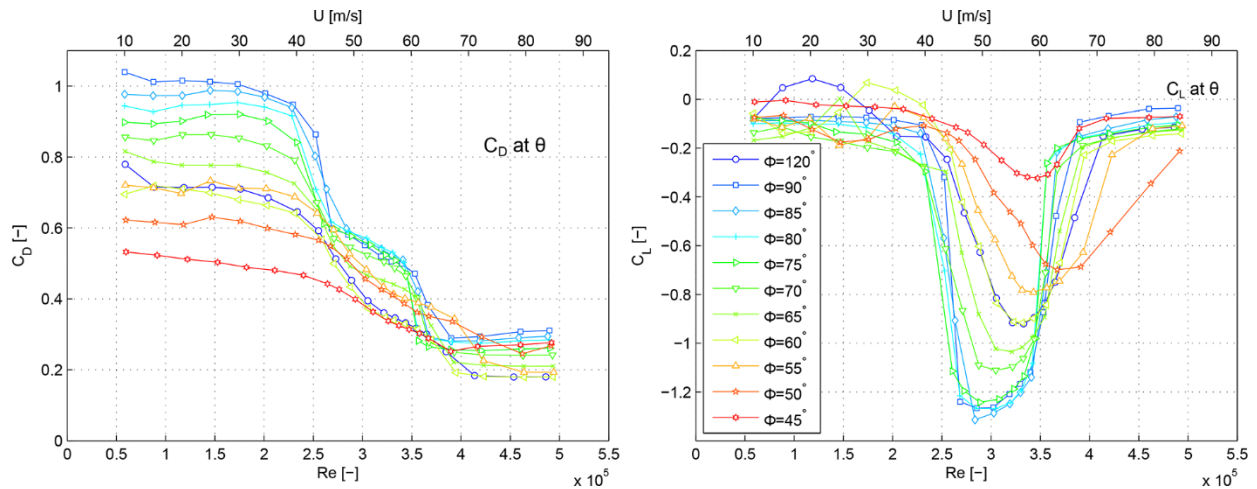
Source: FHWA.

Note: Geometrical angle of attack $\alpha_{\theta=60°}$ = 90 degrees. The coefficients are components normal to the cable axis, inclination angle θ.

Figure 44. Graph. IR118E: Mean drag and lift coefficients as a function of Reynolds number for various cable-wind angles.
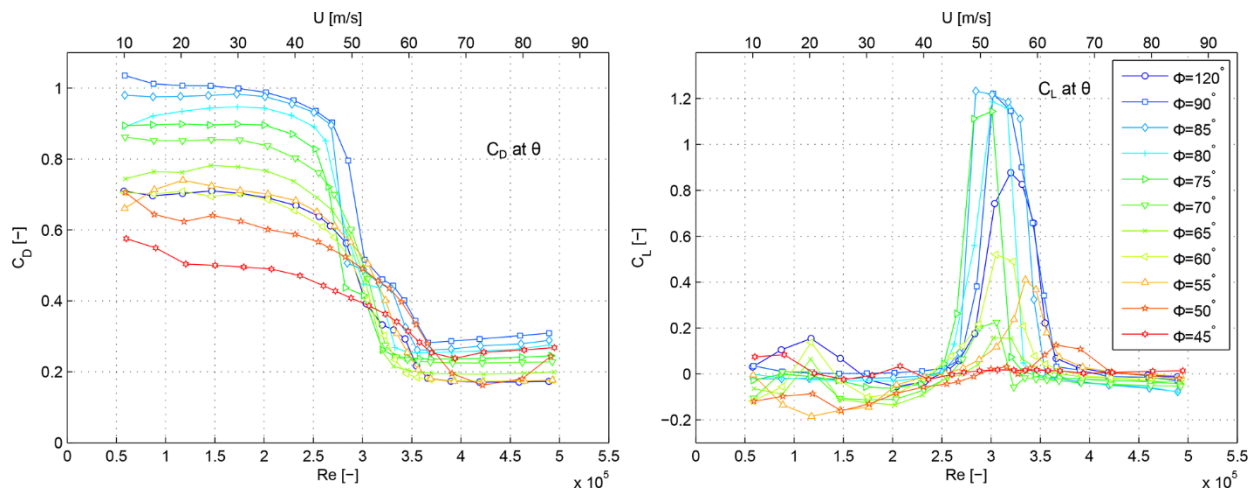
Source: FHWA.

Note: Geometrical angle of attack $\alpha_{\theta=60°}$ = −100 degrees. The coefficients are components normal to the cable axis, inclination angle θ.

Figure 45. Graph. IR118E: Mean drag and lift coefficients as a function of Reynolds number for various cable-wind angles.

The plateaus for the drag coefficient also gradually smoothen. Also, the curves for $\Phi = 120$ degrees coincided well with curves for $\Phi = 60$ degrees. For the other geometrical angles of attack shown in figure 45, the lift coefficient remained positive for all Φ, but a less systematic decrease in value. This geometrical angle of attack was more unstable or sensitive to different cable-wind angles. However, the lift coefficient was also more sensitive to small changes in the angle of attack. At $Re = 3 \times 10^5$, a 0.4 difference in lift coefficient was found between $\alpha = -100$ and -102.5 degrees (figure 35). This difference meant that a slight discrepancy in angle of attack could change the outcome. Nevertheless, the lift was generally lower for the lowest cable-wind angles, and the largest C_L were found for $\Phi = 75, 80, 85,$ and 90 degrees. The plateaus in drag have not been reported elsewhere in stay cable wind-angle studies. For earlier studies, the handling of the HDPE tube to construct the model—either when placed on an inner metallic core or through cutting a smaller section—could have removed larger surface shape distortions, thereby reducing the extent of the one-bubble regime.

The variations of the aerodynamic force coefficients for the cable model with helical fillets, IR113E HF, are shown in figure 46 and figure 47. The variations in drag and lift are similar between the two, but the drag was increased, and the lift decreased in figure 47 compared with figure 46. The magnitude and variations of the drag coefficient are similar to previous findings by Kleissl and Georgakis.[24]
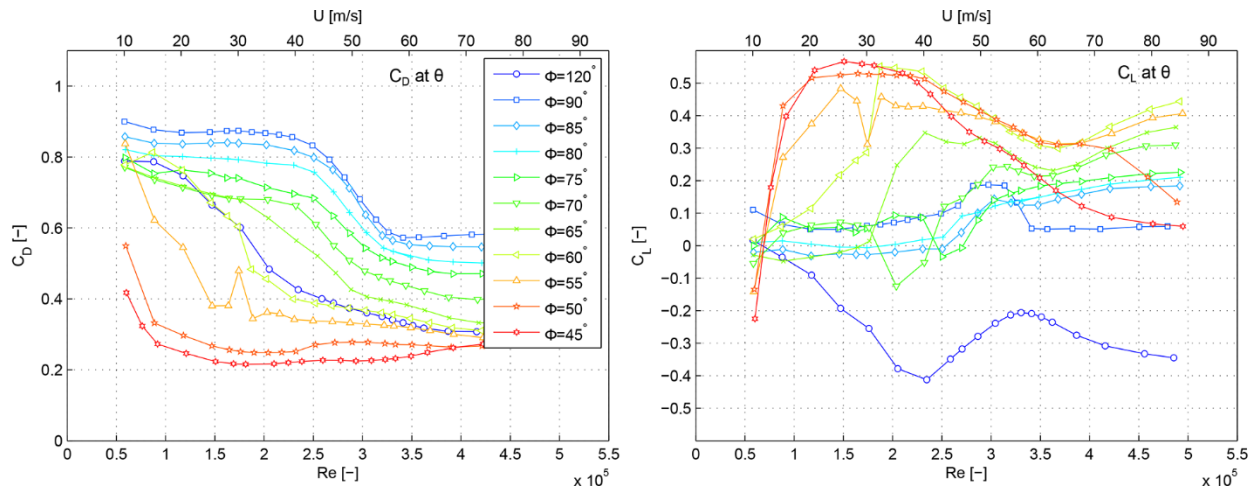
Source: FHWA.

Note: Geometrical point of attack $\alpha_{\theta=60°} = 55$ degrees. The coefficients are components normal to the cable axis, inclination angle θ.

Figure 46. Graph. IR113E HF: Mean drag and lift coefficients as a function of Reynolds number for various cable-wind angles.
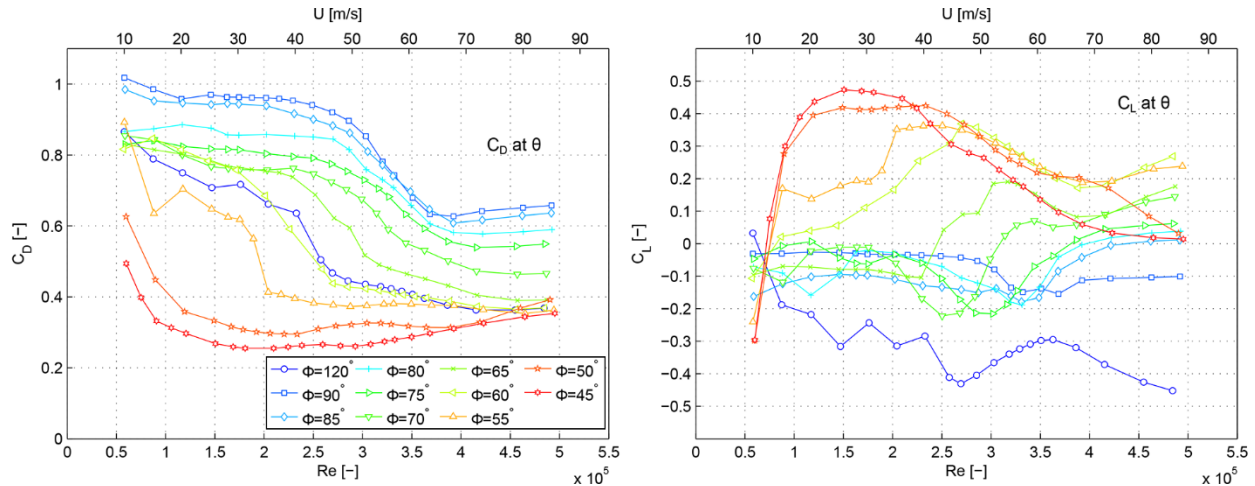
Source: FHWA.

Note: Geometrical point of attack $\alpha_{\theta=60°} = -48$ degrees. The coefficients are components normal to the cable axis, inclination angle θ.

Figure 47. Graph. IR113E HF: Mean drag and lift coefficients as a function of Reynolds number for various cable-wind angles.

In turbulent flow, the influence of surface irregularities was still clear for the cables with helical fillets. For IR113E HF (figure 55), the magnitudes of the drag and lift coefficients appeared in the same sequence as in smooth flow (figure 40). For example, the lowest lift coefficient was recorded for $\alpha = 100$ degrees, and the largest lift coefficient in the supercritical regime was for $\alpha = 35$ and 45 degrees.

The boundary layer transitions in Kleissl and Georgakis's study took place at lower Reynolds numbers. The lower numbers are attributed to a wind-tunnel turbulence intensity 3-4.5 times higher than the turbulence level in the 2- by 3-m wind tunnel for the current study in smooth flow.[24] Kleissl and Georgakis' largest reported lift was also slightly larger, reaching approximately 0.68.[24] The designs of the helical fillets were different in the two studies, which will influence the aerodynamics. Contrary to the results for the smooth cable model, the drag crisis for the cable with helical fillets and the nonzero lift was displaced to lower Reynolds numbers for decreasing Φ. This shift could be caused by the fillets tripping the flow to an earlier transition, as also suggested by Kleissl and Georgakis.[24]

For $\Phi = 90$ degrees, the mean lift was near zero. The periodic asymmetry introduced to the cross section by the helical fillets at this angle introduced periodic changes in lift that would cancel out over the length of the cable. However, a nonzero contribution is seen near $Re = 3 \times 10^5$, which could possibly be related to the formation of local separation bubbles. For the cable-wind angle of 120 degrees, the direction of the lift changed due to the 180-degree yaw. Some deviations in magnitude were observed between $\Phi = 120$ and 60 degrees.

CHAPTER 5. ANALYSIS AND DISCUSSION

QUASI-STEADY ANALYSIS

The wind-tunnel experiments of this study were carried out to establish a link between surface irregularities of the cross-sectional shapes of stay cables and propensity to wind-induced vibrations. By combining the variations of the aerodynamic force coefficients with Reynolds number and attitude to the flow of the cable models to the quasi-steady aerodynamics theory presented in Macdonald and Larose for a one degree-of-freedom (DOF) system, it is possible to predict the level of aerodynamic damping associated with the shapes investigated in this study.[21]

Based on Macdonald and Larose's study, the aerodynamic damping can be expressed by the equation shown in figure 48: [21]

$$
\zeta_a = \frac{\mu Re}{4m\omega_n} \cos\alpha_s \left\{
\begin{array}{l}
\cos\alpha_s \left[C_D \left(2\sin\phi + \frac{\tan^2\alpha_s}{\sin\phi} \right) + \frac{\partial C_D}{\partial Re} Re\sin\phi + \frac{\partial C_D}{\partial\phi}\cos\phi - \frac{\partial C_D}{\partial\alpha}\frac{\tan\alpha_s}{\sin\phi} \right] \\
- \sin\alpha_s \left[C_L \left(2\sin\phi - \frac{1}{\sin\phi} \right) + \frac{\partial C_L}{\partial Re} Re\sin\phi + \frac{\partial C_L}{\partial\phi}\cos\phi - \frac{\partial C_L}{\partial\alpha}\frac{\tan\alpha_s}{\sin\phi} \right]
\end{array}
\right\}
$$

Figure 48. Equation. Aerodynamic damping.

Due to the sag of stay cables, the natural frequencies of the cables in-plane and out-of-plane are different. The equations for a two DOF system have also been derived, but this approach is only feasible for a detuning of the frequencies smaller than two to three percent. For larger detuning, the two DOF solutions gravitate toward the one DOF solution, making it the preferred approach here.

The parameter α in figure 48 is the angle of attack. The aerodynamic damping also depends on the structural angle α_s, which is the angle between the motion direction of the body and the wind component normal to the cable axis. For the current setup with the inclination angle $\theta = 60$ degrees and the yaw angle $\beta = 0$ degrees, structural angles of 90 to 93 degrees were found for a sectional cable model with a smooth HDPE tube using a dynamic test rig.[4] The possibility of wind-induced vibrations for other structural angles α_s, however, should not be ignored.

The cable-wind angle ϕ (or Φ) is the angle between the cable vertical plane and the incoming wind speed, as shown in figure 19.

The derivatives with respect to ϕ have been ignored for the following calculations since these contributions were not available from the current tests for the reference shapes (and for most of the cable shapes). The contribution to the aerodynamic damping from these terms depends on α_s and ϕ. In the case of a pure across-wind response, $\alpha_s = 90$ degrees, the terms will vanish. As the motion direction becomes increasingly along-wind, the terms are more pronounced. However, the exact influence depends on the magnitude of the other terms in figure 19. For smooth cable

models, no study is known where one DOF model with all terms included has been applied. A quasi-steady analysis of the results of the tests on the scanned cable shapes, including the $\partial C_L/\partial \phi$ term, could be performed, but the $\partial C_L/\partial \alpha$ term would have to be ignored.

To leave out the dependency on the mass m and natural frequency f_n of the cable and the dynamic wind viscosity μ, a nondimensional aerodynamic damping parameter was suggested by Macdonald and Larose, as shown in figure 49.[21]

$$Z_a = \frac{\zeta_a m f_n}{\mu}$$

Figure 49. Equation. Nondimensional aerodynamic damping parameter.

The inherent structural damping of cable stays is generally negligible compared with the aerodynamic damping. As a result, the condition for instability is taken as $Z_a < 0$.

Regions of instability were found for a range of structural angles from 0 to 180 degrees. Only a few structural angles in steps of 30 degrees are shown in the following figures as they provided a reasonable envelope of the data. These angles are 0, 30, 60, 90, 120, and 150 degrees. The nondimensional aerodynamic damping parameter Z_a is shown in figure 50 and figure 51 for the 5-percent oval and the flat-faced cylinders, respectively. The minimum values are marked in each case, and the contributions to Z_a from the six terms in figure 48 are listed in table 3. Similar graphs of nondimensional aerodynamic damping as a function of α_s and Reynolds number for other shapes of this study are presented by Christiansen et al.[7]
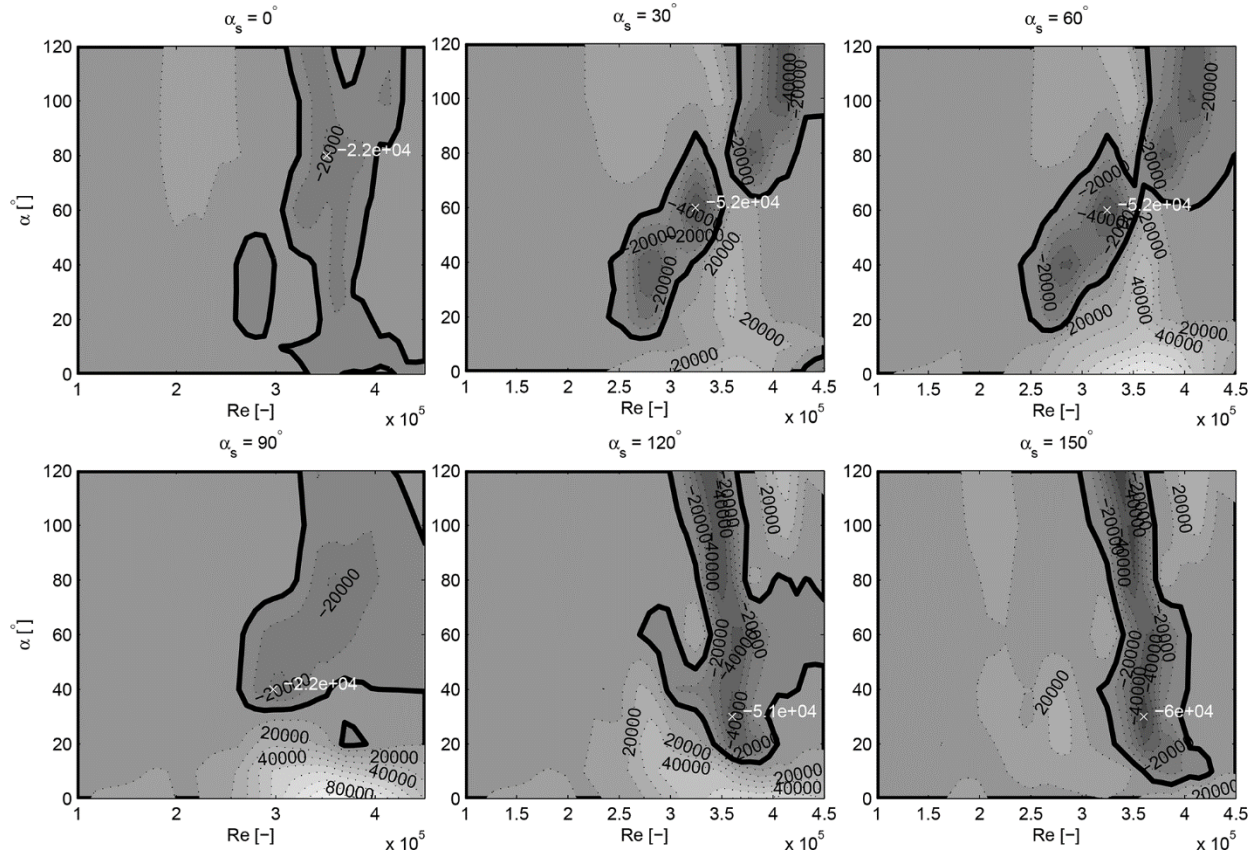
Source: FHWA.
Note: Thick black lines mark instability regions.

Figure 50. Graph. Nondimensional aerodynamic damping Z_a for the 5-percent oval model at different structural angles α_s for varying angles of attack α and Reynolds number.
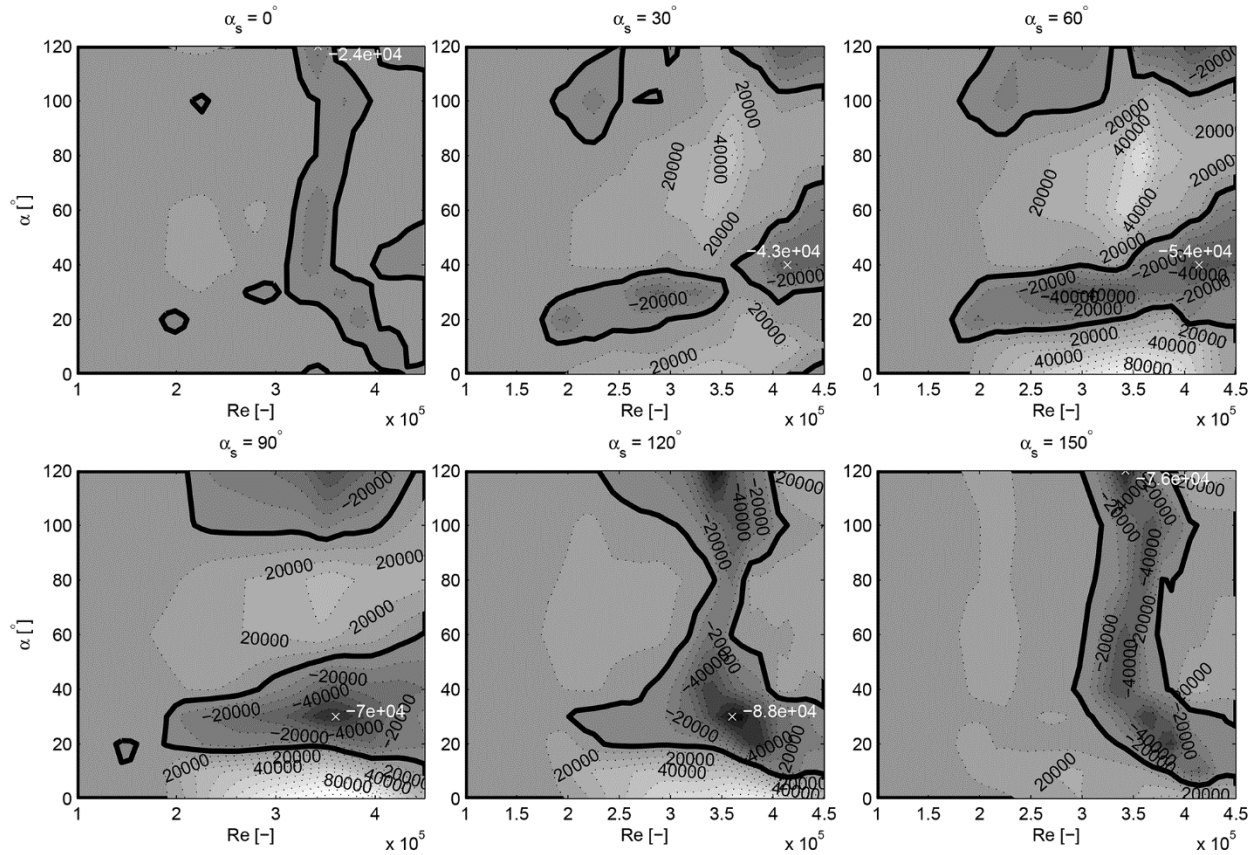
Source: FHWA.
Note: Thick black lines mark instability regions.

Figure 51. Graph. Nondimensional aerodynamic damping Z_a for the flat-faced model at different structural angles α_s for varying angles of attack α and Reynolds number.

Table 3. Minimum Z_a for various structural angles αs with related angle of attack α and Reynolds numbers, and contributions to Z_a from the complete individual terms (e.g., $\partial C_L/\partial Re \times Re \sin\phi$) in figure 48.

Model	α_s	$Z_{a,min}$	α	Re	C_D	$\partial C_D/\partial Re$	$\partial C_D/\partial \alpha$	C_L	$\partial C_L/\partial Re$	$\partial C_L/\partial \alpha$
	[Degrees]	[/10³]	[Degrees]	[/10⁵]	[/10³]	[/10³]	[/10³]	[/10³]	[/10³]	[/10³]
	0	−19	80	3.42	9	−27	—	—	—	—
	30	−36	100	3.87	6	−11	0	1	−30	−1
	60	−33	100	3.87	5	−4	0	1	−30	−4
Oval 3%	75	−19	100	3.87	4	−1	0	1	−17	−5
	90	−14	80	3.42	6	—	—	—	—	−19
	105	−33	80	3.42	6	−2	0	0	−19	−18
	120	−50	60	3.42	5	−6	1	1	−43	−8
	150	−54	60	3.42	6	−17	1	1	−43	−3
	0	−22	80	3.51	10	−33	—	—	—	—
	30	−52	60	3.24	10	−20	−2	−1	−33	−6
	60	−52	60	3.24	8	−7	−2	−1	−33	−17
Oval 5%	75	−37	60	3.24	7	−2	−1	−1	−19	−22
	90	−22	40	2.97	5	—	—	—	—	−27
	105	−36	80	3.51	7	−2	1	−1	−16	−25
	120	−51	30	3.6	5	−6	0	2	−50	−2
	150	−60	30	3.6	6	−17	0	2	−50	0
	0	−24	120	3.42	11	−35	—	—	—	—
	30	−43	40	4.14	8	−10	−2	3	−34	−8
	60	−54	40	4.14	6	−3	−2	3	−34	−23
Flat-faced	75	−57	30	3.42	6	−1	−1	−1	6	−66
	90	−70	30	3.6	5	—	—	—	—	−75
	105	−85	30	3.6	5	−1	0	1	−20	−70
	120	−88	30	3.6	6	−5	1	1	−34	−56
	150	−76	120	3.42	10	−26	2	−2	−47	−13

—No value.

The instability regions for the two oval cylinders were similar. Negative Z_a were obtained for most angles of attack α, although mainly from 30 to 120 degrees. For values $0 < \alpha_s < 90$ degrees, there were two instability regions that merged for $\alpha_s \geq 90$ degrees. The variation between the structural angles α_s was, however, not major, unlike the flat-faced cylinder. For the flat-faced cylinder, two horizontal instability regions merged into one vertical region for increasing α_s. For a fixed angle of attack, the planes had unstable vibrations and, as a result, varied significantly.

If the motion direction is purely across-wind (i.e., $\alpha_s = 90$ degrees), figure 48 is reduced to the conventional Den Hartog galloping condition of instability (figure 52)[19]:

$$ C_D + \partial C_L / \partial \alpha < 0 $$

Figure 52. Equation. Galloping condition of instability.

with a factor of $1/\tan \phi$. Note that if the dominating motion direction is across-wind, the total lift contribution is larger than in the case of along-wind motion ($\alpha_s = 0$ or 180 degrees) where drag takes over. This phenomenon is due to the $\cos \alpha_s \sin \alpha_s$ term. In an along-wind dominated motion direction, the contribution $\partial C_L / \partial \alpha$ is more significantly reduced compared with across-wind motion due to $\tan \alpha_s$. Therefore, the dominating contributions to negative Z_a are highly dependent on the structural angle α_s and on the cylinder shape. For all the models, the three most significant contributions to negative Z_a generally come from the $\partial C_D / \partial Re$, $\partial C_L / \partial Re$, and $\partial C_L / \partial \alpha$ terms (table 3). The larger the change in cylinder shape, the more influential the change in lift with respect to angle of attack becomes. The contributions from the $\partial C_D / \partial \alpha$ and C_L terms are negligible.

Concerning the 5-percent oval cylinder at the structural angles shown in figure 50, the dominating Z_a contribution comes from the $\partial C_L / \partial Re$ and $\partial C_L / \partial \alpha$ terms (table 3). The two extra structural angles, 75 and 105 degrees, in table 3 illustrate that the $\partial C_L / \partial \alpha$ contribution reduced quickly as the structural angle moved away from pure across-wind. As expected, the $\partial C_L / \partial \alpha$ contribution does, however, have a larger influence for the 5-percent oval model than for the 3-percent oval model. When the dominating motion direction became along-wind, the $\partial C_D / \partial Re$ contribution became significant.

For the flat-faced model with the more abrupt changes in shape, the contribution to the $\partial C_L / \partial \alpha$ term increased significantly and remained dominating over a larger α_s range. However, the values shown in table 3 were taken at one specific angle of attack α, and the governing contributions may have changed for other α. For example, for the flat-faced model at $\alpha_s = 120$ degrees, the dominating contribution for $\alpha = 60$ degrees came from the $\partial C_L / \partial Re$ term. Overall, for the structural angles shown, the more unstable regions were between the angles of attack of 20 to 40 degrees and 100 to 120 degrees.

Another important note is that the increments for α are either 10 or 20 degrees, which is a fairly coarse scale. For a cable in motion, a change in relative angle of attack would likely be around one to two degrees.

The results in table 3 represent a significant magnitude of aerodynamic damping that can be illustrated by plugging values of $f = 1.4$ Hz and $m = 66.7$ kg/m into the equation in figure 49. These values were taken from the previously mentioned Larose and D'Auteuil study.[4] For $\mu =$

1.82×10^{-5} N-s/m^2, $\zeta_a = -1.72$ percent for the largest negative nondimensional aerodynamic damping of -88×10^3 for the flat-faced model. This level of negative aerodynamic damping is important and would be difficult to mitigate with external cable dampers.

For most structural angles α_s, the contribution to Z_a by the $\partial C_L/\partial Re$ term could yield negative aerodynamic damping on its own without including the contributions from the terms $\partial C_D/\partial Re$ and $\partial C_L/\partial \alpha$. This phenomenon indicates that even for the cylinder with a round cross section, negative Z_a would be obtained since $\partial C_L/\partial Re$ is of similar magnitude and at the same Reynolds numbers as the oval and the flat-faced cylinders (figure 27 and figure 31). The magnitudes of $\partial C_L/\partial Re$ could not be related exclusively to the cross-sectional shapes.

This $\partial C_L/\partial Re$ term, however, proved insignificant for the Larose and D'Auteuil 2011 tests carried out on a sectional cable model with a smooth HDPE tube.[4] The results of a quasi-steady analysis were not published in the 2011 report, but the calculations from it are used in this study for comparison. For the cable rotation of -90 degrees, the smallest value of $\partial C_L/\partial Re$ was -0.7×10^{-5}, less than half the size of the smallest obtained for the oval and flat-faced cylinders shown in figure 27 and figure 31, respectively. Also, the drag crisis was displaced to lower Reynolds numbers with a difference of 10^5, which reduced the contribution of the complete $\partial C_L/\partial Re$ term (table 3) to more than -5×10^3. The displacement of the drag crisis region can be related to different turbulence intensities in the wind tunnels and different surface roughness of the models. Also, the forces from the tests in 2011 were based on the mean of four rings of pressure taps and not measured over the entire length of the model, as was the case in the present study.

DISCUSSION

Large amplitude vibrations have often been related to the drag crisis region and could be induced by changes in lift with the relative angle of attack. Based on the quasi-steady theory, the more abrupt the changes in surface shape curvature, the more dominating the $\partial C_L/\partial \alpha$ term became. In this section, the report discusses how a random cross section could be oriented for sufficiently large changes in the lift coefficient with the angle of attack to occur. The direction of the wind should be such that the asymmetric state switches sides or disappears for only a small change in angle of attack. For the reference sections studied in this report, the direction of the mean lift in the asymmetric regime was determined by the inwards curvature of the cross-section downstream of the laminar separation point. As the inward curvature gets smaller, the adverse pressure gradient becomes smaller, and the smaller a flow velocity change was needed to surmount the pressure gradient. In these tests, the first laminar separation bubble often formed on the side of the cylinder where the locally widest point was positioned the furthest upstream. The inward curvature downstream of the laminar separation location would generally be smaller on this side than on the opposite side, where the locally widest point was further downstream. The laminar separation point would also be positioned further upwind, and turbulent reattachment of the shear layer would occur here first.

For more symmetric locations of the widest points, the cylinder side with the locally widest point and furthest upstream was not necessarily where the first laminar separation bubble would form (i.e., the 5-percent oval model at $\alpha = 80$ degrees).

For true bridge cable cross sections, the surfaces may be more irregular, and the locally widest point may not necessarily indicate the direction of the mean lift. However, as observed in the test results of the replicates of true stay-cable shapes, this statement has proved to be true for some of the shapes. For example, with an elliptical cross section and the wind normal to the major axis (figure 53), a small change in relative angle of attack to either side could cause a change in the direction of lift.
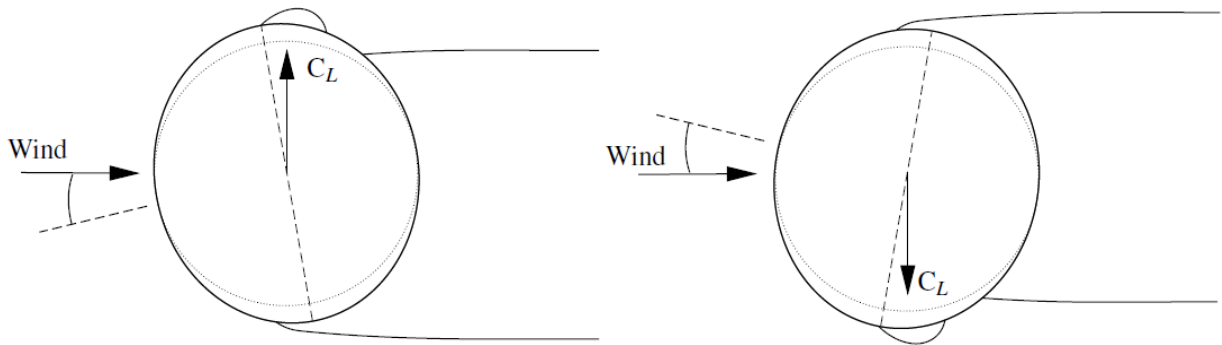
Source: FHWA.

Figure 53. Illustration. Change in direction of lift related to the formation/disintegration of a laminar separation bubble with only small changes in angle of attack of an elliptical section (exaggerated to facilitate understanding).

Natural jumps between boundary layer transition states for a fixed angle of attack occurred while testing the stationary cable models and were reported by Christiansen et al.[7] Correlating the cross-sectional shape with the occurrence of the boundary layer instabilities was not possible, but the instabilities were more frequently observed with larger changes in the curvature of the cross-sectional shapes.

CHAPTER 6. CONCLUSIONS AND RECOMMENDATIONS

REFERENCE CROSS-SECTIONAL SHAPES

The variations of the aerodynamic force coefficients with respect to Reynolds number and the angle of attack were discussed and related to the cylinder shape. Generally, once separation of the boundary layer happened, flow would reattach and form a separation bubble on the side of the cylinder with the smallest change in curvature downstream of the laminar separation point and, therefore, the weakest adverse pressure gradient. So, the lift force (across-wind) would also be directed to this side.

Considering the oval cylinders, the lift would be directed toward the distorted cylinder side when the oval head was on the upstream side. At about an 80-degree angle of attack, the lift would switch direction (the angle being dependent on the ovalization degree of either 3- or 5-percent) and be directed toward the circular side. A transition from laminar to turbulent flow in the boundary layer would, in the latter case, happen on the circular side of the cable at the same Reynolds number as a circular cylinder. The magnitude in lift generally increased as the ovalization degree increased. The extent of the asymmetric regime was related to the difference between the magnitude of the adverse pressure gradients on the opposing cylinder sides. The asymmetric regime extended over a larger range of Reynolds numbers as the changes in curvature increased on one cylinder side and were, therefore, the longest for the flat-faced cylinder. Besides a nonzero lift, the asymmetric regime also led to a plateau in the drag coefficient for increasing Reynolds numbers. In some cases, the changes in curvature of the surface for the flat-faced cylinder and, in turn, the adverse pressure gradient was too severe for flow reattachment, and no separation bubble would be formed.

The maximum rate of change of the drag coefficient with respect to Reynolds number was for all three reference shapes either equal to or smaller than for a circular cylinder, systematically depending on the angular position of the oval head or the rounded corners on the flat-faced cylinder. Concerning the rate of change of lift, the values were in the vicinity of one another, but no direct conclusion could be drawn from the oval cylinders. For the flat-faced cylinder with the largest changes in curvature after laminar flow separation, the rate of change seemed larger than for a circular cylinder. The rate of change of the force coefficients as a function of the angle of attack increased as changes in curvature of the surface increased.

From the quasi-steady analysis, the $\partial C_L/\partial Re$ contribution to the aerodynamic damping was found to dominate the unstable regions for the 3-percent oval cylinder. This domination by the $\partial C_L/\partial \alpha$ contribution was also the case for the 5-percent oval cylinder, but it had somewhat more influence in a narrow region of across-wind dominated vibration planes. However, for the flat-faced cylinder, the $\partial C_L/\partial \alpha$ contribution, was, as expected, significant. The contributions from the $\partial C_D/\partial \alpha$ and C_L terms were of negligible magnitude. For the oval cylinders, instabilities were seen for all angles of attack but mainly for 30 to 120 degrees. For the flat-faced cylinder, instabilities were generally between 20 to 40 and 100 to 120 degrees.

This part of the study provided a good understanding of the aerodynamics of cylinders in relation to their shape distortions. The results indicated that the change in lift coefficient as a function of

angle of attack could instigate vibrations. This portion of the experiment also indicated which shape characteristics could cause such large aerodynamic force changes, and how these critical angles could be determined. These findings significantly advance understanding of the more realistic stay-cable cross sections.

STAY-CABLE CROSS-SECTIONAL SHAPES

The aerodynamics of various replicates of HDPE tube field shapes were investigated, which had never been done before. This study was completed to determine the influence on the aerodynamics of measured distortions of the protective HDPE tubes.

The aerodynamic force coefficients with respect to Reynolds number were found to be highly dependent on the angle of attack. For one of the cross sections, the direction of the lift force was related to the shape of the cylinder for different angles of attack. The formation of the first laminar separation bubble was not random. The formation was instead related to the cylinder shape, which is critical to the development and magnitude of the adverse pressure gradients. The difference between the adverse pressure gradients on the opposing cylinder sides also determined the velocity range over which the asymmetric regime extended. For increasing deformations, the range generally became wider.

The magnitude of the derivative of the lift coefficient with respect to the angle of attack reached a value of up to -12.7. This value is significantly larger than the current value of -2.0 in the PTI recommendations. As a result, a cable with this cross-sectional shape could be prone to large wind-induced vibrations for certain wind directions.

When a helical fillet was added to the cross sections, variations in the force coefficients with angle of attack were still observed, although they were smaller. In fact, certain characteristics of the force coefficients could be tracked between the models with and without helical fillets. As the side of the cable with the helical fillet behaved similarly to a smooth cylinder, the shape distortions did, at least on this cable side, still influence the transition of the boundary layer. The magnitude of the derivative of the lift coefficient with respect to the angle of attack was reduced to -3.0. This transition change occurred in the subcritical region.

The influence of the cable-wind angle was examined. Here, the component of the wind was directed toward the same geometrical line on the cable model to account for the model shape. To the authors' knowledge, such a study has not been carried out before. The variations of the drag and lift coefficients were distinct for each geometrical point of attack, and regions of potential instabilities were identified.

RECOMMENDATIONS

This study demonstrates that shape distortions of the HDPE tube are an important parameter for the understanding of the aerodynamics of stay cables.

As a result, further research should be done to verify, through dynamic tests on free-to-respond replicas of stay cables that the level of aerodynamic damping predicted from the quasi-steady theory is appropriate. This verification is in accordance with the planned second phase of this study, where three of the shapes investigated in the first phase would be tested in a dynamic rig.

The three cable shapes that are being recommended for the second phase are the flat-faced reference shape, IR118E, and IR113E HF. Ideally, the tests should be carried out on full-scale replicas in a large two DOF dynamic rig and a wind tunnel capable of accommodating 6-m-long section models. However, the difficulty of fabricating full-scale replicas of stay cables might be hard to overcome. The current SLS technology is not suitable for making large pieces. An alternative approach would be to devise a new dynamic rig suitable for smaller section models such as those used in the first phase. The SLS models and the carbon fiber spar of the current study could be reused, ensuring that the test conditions would be identical. The models could be kept light, and the mass-damping parameter (i.e., Scruton number) could be adjusted by adding structural damping. The experiments could be carried out at low wind speeds in the sub-critical Reynolds number range and at high wind speeds in the critical range to confirm the influence of Reynolds number on the wind-induced vibrations.

PTI should consider integrating these results into the larger body of knowledge that supports their existing stay-cable design guidelines with regard to stay-cable galloping, with and without the ice accretion. The results of the current study reveal that stay-cable shapes could experience larger negative aerodynamic damping conditions than covered by the guidelines. Given the multitude of cross-sectional shapes, a statistical approach is needed where the probability of exceeding predefined negative aerodynamic levels would be determined based on a number of representative samples of stay-cable cross-sectional shapes. The experiments discussed constitute the start of this database. The measurement campaign of cross-sectional shapes of stay cables in service initiated by FHWA would be at the center of this approach. The authors of this study, therefore, recommend that the FHWA campaign continue to scan cables from as many recent bridges as possible and establish whether cross-sectional shapes of HDPE tubes vary over time.

APPENDIX A. DETAILED LIST OF RUNS AND EXPERIMENTAL CONDITIONS

Table 4 through table 27 contain the test matrix logs from wind tunnel testing conducted in 2015. Block 1 testing involved 20-point speed sweeps at 9-axial rotations. Group A includes the reference shapes. Group B includes the cable shapes. Positive rotation values indicate counterclockwise rotation, and negative rotation values are clockwise rotation.

Table 4. Block 1 testing, group A, calibration.

Day	Tare	Run No.	No. Point	Comment	Inclination (Degrees)	Yaw Angle (Degrees)	Axial Rotation (Degrees)	Observations; State Jumps
5/20	—	—	—	No tare, Fs=1500Hz, LP 600Hz, t=5s, positive-negative values, mean only.	—	—	—	—
5/20	—	7	—	Floor Fx1.	—	—	—	—
5/21	—	8	—	Floor Fy1.	—	—	—	—
5/21	—	9	—	Top Fx2.	—	—	—	—
5/21	—	10	—	Top Fy2.	—	—	—	—
5/21	—	12	—	Balance Fx3 (point 9+10 are not good).	—	—	—	—
5/21	—	13	—	Balance Fy3.	—	—	—	—
	—	24	—	Tare.	—	—	—	—
5/21	27	28	—	10 lb pull from top balance in the wind direction (Y).	60	0	—	—
5/21	29	30	—	Round model installed, tech pushing with one hand.	60	0	—	—
5/21	31	32	3	Round model installed. point 1: no load. Point 2: tech pushing toward control room. Point 3: tech pushing downwind.	60	0	—	—

65

Day	Tare	Run No.	No. Point	Comment	Inclination (Degrees)	Yaw Angle (Degrees)	Axial Rotation (Degrees)	Observations; State Jumps
—	—	—	—	Unless otherwise specified, all runs are Reynolds number sweeps of approximately 20 points to cover the critical Reynolds number range.	—	—	—	—

—No notes were taken.

Table 5. Block 1 testing, group A, model: circular cylinder.

Day	Tare	Run No.	No. Point	Comment	Inclination (Degrees)	Yaw Angle (Degrees)	Axial Rotation (Degrees)	Observations; State Jumps
5/22	34	35	8	Shakedown. Bad data: motion of the upper end influenced following data sampling. Upper end vibrating at approx. 50 m/s (point 3). Point 7: rampdown 85–0 m/s. point 8: 0 m/s.	60	0	0	State jumps seen at ca. 15m/s during the sweep.
5/22	34	36	—	0 m/s taken 5 min after run 35	60	0	0	—
—	—	—	—	Pretest (run 38) voltage FX1 = −0.2 V, Y1 = −0.37 V, X2 = −0.060 V, Y2 = −0.12 V.	60	0	0	—

Day	Tare	Run No.	No. Point	Comment	Inclination (Degrees)	Yaw Angle (Degrees)	Axial Rotation (Degrees)	Observations; State Jumps
5/22	37	38	8	Shakedown. Point 7: rampdown 85–0 m/s. point 8: 0 m/s.	60	0	0	State jumps at 40–45 m/s and 50–60 m/s during the sweep. Tech made fast changes in the wind speed - this could be why we see so pronounced state jumps - affected by wind.
5/22	—	39	—	0 m/s taken 5 min after run 38.	60	0	0	—
5/25	—	—	—	Start-up procedure. Measuring wind for 5 min. 4 blades, 16 stators, at 40 m/s the rpm is 230.	60	0	0	—
5/25	41	42	14	Shakedown. Delpc1 not working: bad data.	60	0	0	Large jumps between 60–70 m/s
5/25	41	43	—	1 point at 50 m/s only	—	—	—	—
5/25	44	45	20	First test.	60	0	0	Instantaneous jumps 30–40 m/s, big jump 56–57 m/s. After 68 m/s no vortex shedding.
5/25	46	47	21	Repeat of run 45 with two more points.	60	0	0	45 m/s instantaneous jumps. Big jump again 57–58 m/s.
5/25	48	49	17	Tape over gaps between model ends and central part.	60	0	0	—

Day	Tare	Run No.	No. Point	Comment	Inclination (Degrees)	Yaw Angle (Degrees)	Axial Rotation (Degrees)	Observations; State Jumps
5/25	50	51	21	Model rotated 45 deg clockwise. Note: Positive rotation is clockwise versus the models by FHWA, where it is counterclockwise.	60	0	45	Jumps on FX2 at 15 m/s. large FX1 oscillations at 60 m/s.

—No notes were taken.

Table 6. Block 1 testing, group A, model: oval 3 percent.

Day	Tare	Run No.	No. Point	Comment	Inclination (Degrees)	Yaw Angle (Degrees)	Axial Rotation (Degrees)	Observations; State Jumps
5/25	52	53	21	—	60	0	0	State jump by 30 m/s.
5/26	54	55	20	—	60	0	10	State jump by 45–46 m/s, picture 100-1783. No more side force at U = 68 m/s.
5/26	56	57	19	—	60	0	20	—
5/26	59	60	20	—	60	0	30	Large side force jump between 45 and 50 m/s.
5/26	62	63	19	—	60	0	40	—
5/26	64	65	19	—	60	0	60	—
5/26	66	67	19	—	60	0	80	—
5/26	68	69	20	—	60	0	100	—
5/26	70	71	20	—	60	0	120	—

—No notes were taken.

Table 7. Block 1 testing, group A, model: oval 5 percent.

Day	Tare	Run No.	No. Point	Comment	Inclination (Degrees)	Yaw Angle (Degrees)	Axial Rotation (Degrees)	Observations; State Jumps
5/25	52	53	21	—	60	0	0	State jump by 30 m/s.
5/26	54	55	20	—	60	0	10	State jump by 45–46 m/s, picture 100-1783. No more side force at U=68 m/s.
5/26	56	57	19	—	60	0	20	—
5/26	59	60	20	—	60	0	30	Large side force jump between 45 and 50 m/s.
5/26	62	63	19	—	60	0	40	—
5/26	64	65	19	—	60	0	60	—
5/26	66	67	19	—	60	0	80	—
5/26	68	69	20	—	60	0	100	—
5/26	70	71	20	—	60	0	120	—

—No notes were taken.

Table 8. Block 1 testing, group A, flat face.

Day	Tare	Run No.	No. Point	Comment	Inclination (Degrees)	Yaw Angle (Degrees)	Axial Rotation (Degrees)	Observations; State Jumps
5/28	90	91	20	—	60	0	0	—
5/28	92	93	20	—	60	0	10	Instantaneous jumps near 25 m/s, picture 100-1814.
5/28	94	95	20	—	60	0	20	35 m/s crazy state jumps correlated.
5/28	96	97	21	Last point (no. 21) is at 40 m/s (it was forgotten).	60	0	30	Crazy state jumps over a long velocity span!
5/28	98	99	20	—	60	0	40	—

Day	Tare	Run No.	No. Point	Comment	Inclination (Degrees)	Yaw Angle (Degrees)	Axial Rotation (Degrees)	Observations; State Jumps
5/28	100	101	20	—	60	0	60	—
5/28	102	103	21	—	60	0	80	—
5/28	104	105	20	—	60	0	100	—
5/28	106	107	20	—	60	0	120	—

—No notes were taken.

Table 9. Block 1 testing, group B, shape 5: M46.

Day	Tare	Run No.	No. Point	Comment	Inclination (Degrees)	Yaw Angle (Degrees)	Axial Rotation (Degrees)	Observations; State Jumps
7/27	114	115	8	Shakedown.	60	0	0	—
7/27	116	117	20	—	60	0	0	No. 16 state jumps.
7/27	118	119	20	—	60	0	−55	No. 14–16 state jumps!
7/27	120	121	20	—	60	0	−90	Look around no. 10.
7/27	122	123	20	—	60	0	−93	No. 9–11!
7/27	124	125	20	—	60	0	−115	Jump in between 9 and 10. Jumps at no. 19–20.
7/27	126	127	20	—	60	0	34	No jumps.
7/27	128	129	20	—	60	0	90	Not much. No.5 and 10ish.
7/27	130	131	20	—	60	0	−146	No. 14 a bit.
7/27	132	133	20	—	60	0	148	No. 8, 9, 10!

—No notes were taken.

Table 10. Block 1 testing, group B, shape 6: JR SS08.

Day	Tare	Run No.	No. Point	Comment	Inclination (Degrees)	Yaw Angle (Degrees)	Axial Rotation (Degrees)	Observations; State Jumps
7/27	134	135	20	—	60	0	0	No. 9–15!
7/28	136	137	20	—	60	0	−30	pt3. no. 9–10, pt17 unsteadiness.
7/28	138	139	20	No. 20 is a repeat of no. 16.	60	0	30	pt3, no. 5, something in x at top, pt14 unsteady, pt16 and 17 (18) state jumps. No. 20 is a repeat of no. 16 and state jumps were repeated.
7/28	140	141	20	—	60	0	-56	pt11
7/28	142	143	20	—	60	0	−86	pt4, pt12 unsteadiness x bottom. pt13–16.
7/28	144	145	20	—	60	0	−116	pt4, pt8–10.
7/28	146	147	20	—	60	0	60	pt4, a bit at pt15.
7/28	148	149	20	—	60	0	90	pt11–13! 3 states!
7/28	150	151	20	—	60	0	124	pt9–10.

—No notes were taken.

Table 11. Block 1 testing, group B, shape 7: IR 118E.

Day	Tare	Run No.	No. Point	Comment	Inclination (Degrees)	Yaw Angle (Degrees)	Axial Rotation (Degrees)	Observations; State Jumps
7/28	152	153	21	—	60	0	90	Semi-stable states recorded for the first time! In subcritical state! Only the top one! No. 4–6. pt21 is reproducing pt4, but the jumps did not appear from descending wind speed. We had to go below the 25 m/s and increase again. pt17 jumps bottom lift.
7/28	154	155	20	—	60	0	−126	pt4 again nearly semi-stable. pt10: state jumps.
7/28	156	157	20	—	60	0	70	pt4 again. pt18!
7/28	158	159	20	—	60	0	−54	Boring. unsteadiness pt16–17.
7/29	160	161	20	—	60	0	130	pt13–15 bursts and jumps.
7/29	162	163	21	—	60	0	110	between 35–40 m/s lift changes sign twice, pt9 made to find this. pt3 and 7, some semi-stable. Between 39.5 and 40.5 m/s there is action. pt10–12.
7/29	164	165	20	—	60	0	180	pt17 state jumps. pt1?

Day	Tare	Run No.	No. Point	Comment	Inclination (Degrees)	Yaw Angle (Degrees)	Axial Rotation (Degrees)	Observations; State Jumps
7/29	166	167	20	—	60	0	−100	pt4 and 11–15 state jumps.
7/29	168	169	20	—	60	0	0	(pt4), pt12–16.

—No notes were taken.

Table 12. Block 1 testing, group B, shape 8: IR 113E.

Day	Tare	Run No.	No. Point	Comment	Inclination (Degrees)	Yaw Angle (Degrees)	Axial Rotation (Degrees)	Observations; State Jumps
7/29	170	171	20	—	60	0	−48	pt4 jumps (25 m/s) top only, pt5 (pt19).
7/29	172	173	20	—	60	0	55	pt13–14.
7/29	174	175	20	—	60	0	−80	(pt3–4,15).
7/29	176	177	20	—	60	0	−28	pt5 (pt17).
7/29	178	179	20	—	60	0	35	pt3. pt8 (top bigger than bottom), 9–10 state jumps. 17–18. From TrBL0 to TrBL1, and TrBL1 to TrBL2!
7/29	180	181	20	Last wind speed at pt20 was measured without accounting for the barometric pressure - correct speed by using barometric pressure from pt19. Corrected by tech.	60	0	45	pt3 semi-stable!
7/29	183	184	20	—	60	0	50	pt4 (6), pt15–16.

Day	Tare	Run No.	No. Point	Comment	Inclination (Degrees)	Yaw Angle (Degrees)	Axial Rotation (Degrees)	Observations; State Jumps
7/30	185	186	20	—	60	0	100	pt4, pt9–9 and 17. State jumps from TrBL0 to TrBL1, and TrBL1 to TrBL2!
7/30	188	189	20	—	60	0	10	pt6 and 16.

—No notes were taken.

Table 13. Block 1 testing, group B, shape 9: JR SS13a.

Day	Tare	Run No.	No. Point	Comment	Inclination (Degrees)	Yaw Angle (Degrees)	Axial Rotation (Degrees)	Observations; State Jumps
7/30	190	191	20	—	60	0	50	pt4–5 (12–14 unsteadiness).
7/30	192	193	20	—	60	0	−76	pt16–17 jumps.
7/30	194	195	20	Wind speed issue with pt13–14 (as run181). Fixed by tech.	60	0	−56	pt3,5,10 unsteady, 15–17 jumps!
7/30	196	197	21	pt12–13 are the same wind speed.	60	0	−106	pt(3−)5, State jumps pt12–17.
7/30	198	199	20	—	60	0	180	pt2,6. slow transition
7/30	200	201	21	—	60	0	170	Unsteady drag (pictures taken). pt4–6 semi-stable, pt16.
7/30	202	203	20	—	60	0	−36	pt3, 19 (20).
7/30	204	205	20	—	60	0	160	pt7.
7/30	206	207	20	Delete pt5.	60	0	20	pt4, 18–19ish unsteady.

—No notes were taken.

Table 14. Block 1 testing, group B, shape 10: JR SS13b.

Day	Tare	Run No.	No. Point	Comment	Inclination (Degrees)	Yaw Angle (Degrees)	Axial Rotation (Degrees)	Observations; State Jumps
7/30	208	209	20	—	60	0	−106	pt8–10 (18).
7/31	210	211	20	—	60	0	−76	pt4–5, 11, 18.
7/31	212	213	21	—	60	0	−56	pt4, 10–11, 18.
7/31	214	215	20	—	60	0	−36	pt4–5.
7/31	216	217	20	—	60	0	20	pt5!
7/31	218	219	20	—	60	0	50	—
7/31	220	221	20	—	60	0	160	pt4! Semi-stable for both top and bottom. Rare!
7/31	220	222	4	Extra points to see unsteadiness reported in previous run 221 at low wind speeds.	60	0	160	—
7/31	223	224	20	Bad data. Tape was around dummy part. Time lost.	60	0	170	—
7/31	225	226	20	—	60	0	170	—
7/31	227	228	20	—	60	0	180	pt2–5.

—No notes were taken.

Table 15. Block 1 testing, group B, shape 11: IR 113E with helical fillets.

Day	Tare	Run No.	No. Point	Comment	Inclination (Degrees)	Yaw Angle (Degrees)	Axial Rotation (Degrees)	Observations; State Jumps
7/31	229	230	20	—	60	0	−80	pt4 top semi-stable. Sudden drop in bottom lift. pt6.
7/31	231	232	20	—	60	0	−48	pt7–8 correlated semi-stable jumps!

Day	Tare	Run No.	No. Point	Comment	Inclination (Degrees)	Yaw Angle (Degrees)	Axial Rotation (Degrees)	Observations; State Jumps
7/31	233	234	20	—	60	0	−28	pt6–8 short semi-stable.
8/4	235	236	20	—	60	0	10	pt3, pt5 semi-stable (30 m/s), pt6.
8/4	237	238	20	—	60	0	35	jump between 25 and 30 m/s, hysteris. Plenty jumps unrecorded on the screen but none in the time series.
8/4	239	240	20	—	60	0	45	pt4–7 semi-stable.
8/4	241	242	21	—	60	0	50	(pt1).
8/4	243	244	21	—	60	0	55	pt 8.
8/4	245	246	21	—	60	0	100	(pt3–4) pt5-6.

—No notes were taken.

Block 2 testing involved five-point speed sweeps at multiple axial rotations.

Table 16. Block 2 Testing, IR 118E: U=[40, 52, 58, 64, 70] m/s.

Day	Tare	Run No.	No. Point	Comment	Inclination (Degrees)	Yaw Angle (Degrees)	Axial Rotation (Degrees)	Observations; State Jumps
8/4	—	—	—	Axial rotation (5-degree steps) versus Cf. Only four Reynolds no. Smooth and turbulent flow. (Antisymmetric shapes assumed).	—	—	—	—
8/4	247	248	5	—	60	0	120	—
8/4	249	250	5	—	60	0	115	—
8/4	251	252	5	—	60	0	125	—
8/4	251	253	5	—	60	0	127.5	—

Day	Tare	Run No.	No. Point	Comment	Inclination (Degrees)	Yaw Angle (Degrees)	Axial Rotation (Degrees)	Observations; State Jumps
8/4	251	254	5	—	60	0	135	jumps 58 m/s?
8/4	251	255	5	—	60	0	−120	—
8/4	259	260	5	—	60	0	−110	—
8/4	259	261	5	—	60	0	−105	—
8/4	259	262	5	—	60	0	−102.5	—
8/4	259	263	6	—	60	0	−95	pt3 jumps
8/4	259	264	5	—	60	0	−170	—
8/5	267	268	8	With Cobra Probe, aligned with cable edge opposite control room (right cable side seen from oncoming wind), approximately 2D downwind measured from cable center line. Wind speeds below 50 m/s only. The probe is not correlated with the force sensors. They are two different systems.	60	0	90	—
8/5	269	270	5	With Cobra Probe, 1/4D inward from cable edge opposite control room, approx. 2D downwind measured from cable center line. Last point is ramp down.	60	0	90	—
8/5	271	272	5	With Cobra Probe, approximately 2D downwind from cable center. Last point is ramp down.	60	0	90	—

Day	Tare	Run No.	No. Point	Comment	Inclination (Degrees)	Yaw Angle (Degrees)	Axial Rotation (Degrees)	Observations; State Jumps
8/5	273	274	5	With Cobra Probe installed 15 mm downwind from cable center axis. Last point is ramp down.	60	0	90	—
8/5	275	276	5	—	60	0	−155	—
8/5	277	278	5	—	60	0	−152.5	—
8/5	277	279	5	—	60	0	−140	—
8/5	277	280	5	—	60	0	132.5	pt4 jumps
8/5	277	281	5	—	60	0	134	—
8/5	277	282	5	—	60	0	137	—
8/5	277	283	5	—	60	0	−145	—
8/5	277	284	5	—	60	0	−130	—

—No notes were taken.

Table 17. Block 1 Testing, Group B, Shape 12: JR SS13b with helical fillets.

Day	Tare	Run No.	No. Point	Comment	Inclination (Degrees)	Yaw Angle (Degrees)	Axial Rotation (Degrees)	Observations; State Jumps
8/5	285	286	21	Omit pt7.	60	0	−76	pt1 semi-stable! pt8–9 semi-stable.
8/5	287	288	21	—	60	0	−106	pt1, pt4–7 semi-stable.
8/5	287	289	21	—	60	0	180	(pt3–4) pt8.
8/5	287	290	21	—	60	0	160	pt2 semi-stable.
8/5	287	291	21	—	60	0	50	wild pt9.

Day	Tare	Run No.	No. Point	Comment	Inclination (Degrees)	Yaw Angle (Degrees)	Axial Rotation (Degrees)	Observations; State Jumps
8/5	292	293	many	With cobra probe, aligned with cable edge opposite control room (right cable side seen from oncoming wind), approximately 2D downwind measured from cable center line. Wind speeds below 50 m/s only.	60	0	−106	—
8/6	294	295	21	—	60	0	−36	jumps below 42 m/s, bi-stable pt9.
8/6	294	296	21	—	60	0	20	bi-stable jumps pt8–9.

— No notes were taken.

Table 18. Block 2 testing, IR 113E: U=[35, 45, 55, 65, 75] m/s for the majority.

Day	Tare	Run No.	No. Point	Comment	Inclination (Degrees)	Yaw Angle (Degrees)	Axial Rotation (Degrees)	Observations; State Jumps
8/6	—	—	—	Axial rotation (finer steps) versus Cf. Only a few Reynolds no. Smooth and turbulent flow.	—	—	—	—
8/6	297	298	5	—	60	0	57	—
8/6	297	299	2	forgot a point in run 298.	60	0	57	—
8/6	297	300	5	—	60	0	59	—
8/6	297	301	5	—	60	0	65	—
8/6	297	302	6	—	60	0	63	pt2 semi-stable correlated and uncorrelated between top and bottom! pt1.
8/6	297	303	6	—	60	0	64	pt2.

Day	Tare	Run No.	No. Point	Comment	Inclination (Degrees)	Yaw Angle (Degrees)	Axial Rotation (Degrees)	Observations; State Jumps
8/6	297	304	6	—	60	0	61	—
8/6	297	305	6	—	60	0	70	pt2 three semi-stable states!
8/6	297	306	6	—	60	0	80	pt2 semi-stable!
8/6	297	307	6	—	60	0	90	—
8/6	297	308	6	—	60	0	0	jumps pt1–2.
8/6	297	309	6	—	60	0	−10	pt1, jump enormous pt2.
8/6	310	311	6	—	60	0	−20	pt1–2.
8/6	310	312	6	—	60	0	−38	pt(1)2(3).
8/6	310	313	6	—	60	0	−55	pt2(3).
8/6	310	314	6	—	60	0	−65	pt(1)2(3).
8/6	310	315	6	—	60	0	-72	pt1 (three semi-stable) pt2.
8/6	310	316	6	—	60	0	20	pt1.
8/6	310	317	6	—	60	0	30	pt1–2.
8/6	310	318	6	—	60	0	25	pt1–2.
8/6	310	319	6	—	60	0	27	pt2.
8/6	310	320	6	—	60	0	23	pt2.
8/6	310	321	6	—	60	0	47	pt2.
8/6	310	322	6	—	60	0	49	—
8/6	310	323	6	—	60	0	52	—

—No notes were taken.

Table 19. Block 2 testing, IR 113E with helical fillets and installation of turbulent grid.

Day	Tare	Run No.	No. Point	Comment	Inclination (Degrees)	Yaw Angle (Degrees)	Axial Rotation (Degrees)	Observations; State Jumps
8/7	324	325	7	Turbulent flow. Cobra Probe measurements of turbulence. No model. Use delpc3 for static pressure.	—	—	—	—
8/7	326	327	18	Turbulent flow. Use delpc3 for static pressure.	60	0	-48	pt1–4.
8/7	326	328	21	Turbulent flow. Use delpc3 for static pressure.	60	0	35	pt2 lower.
8/7	326	329	21	Turbulent flow. Use delpc3 for static pressure.	60	0	45	—
8/7	326	330	21	Turbulent flow. Use delpc3 for static pressure.	60	0	100	pt3–7(8).
8/7	326	331	21	Turbulent flow. Use delpc3 for static pressure.	60	0	55	pt3–4.

—No notes were taken.

Table 20. Block 2 testing, IR 118E with installation of turbulent grid.

Day	Tare	Run No.	No. Point	Comment	Inclination (Degrees)	Yaw Angle (Degrees)	Axial Rotation (Degrees)	Observations; State Jumps
8/7	332	333	21	Turbulent flow. Use delpc3 for static pressure.	60	0	90	—
8/7	332	334	21	Turbulent flow. Use delpc3 for static pressure.	60	0	−100	—
8/7	332	335	22	Turbulent flow. Use delpc3 for static pressure.	60	0	−126	—
8/7	332	336	21	Turbulent flow. Use delpc3 for static pressure.	60	0	−54	—

Day	Tare	Run No.	No. Point	Comment	Inclination (Degrees)	Yaw Angle (Degrees)	Axial Rotation (Degrees)	Observations; State Jumps
8/7	332	337	21	Turbulent flow. Use delpc3 for static pressure.	60	0	180	—

—No notes were taken.

Table 21. Block 2 testing, IR 118E: U=[40, 52, 58, 64, 70, 74] m/s.

Day	Tare	Run No.	No. Point	Comment	Inclination (Degrees)	Yaw Angle (Degrees)	Axial Rotation (Degrees)	Observations; State Jumps
8/10	338	339	6	—	60	0	170	—
8/10	338	340	6	—	60	0	160	—
8/10	338	341	6	—	60	0	150	—
8/10	338	342	6	—	60	0	140	—
8/10	338	343	6	—	60	0	−133	—
8/10	338	344	6	—	60	0	80	In post-processing, the angle of attack for run 343 and run 344 needs to be interchanged.

—No notes were taken.

Block 3 testing involved yaw angles, with one fixed axial rotation in smooth flow.

Table 22. Block 3 testing, IR 118E.

Day	Tare	Run No.	No. Point	Comment	Inclination (Degrees)	Yaw Angle (Degrees)	Axial Rotation (Degrees)	Observations; State Jumps
8/10	345	346	20	Corresponds to having the stagnation line of the normal wind component on the same physical location of the model equal to the 90-degree rotation in the initial run 153 setup.	60	32.2	54	pt5. pt7 approximately semi-stable. pt16 unsteady. Like run153 (pt4–6,17).
8/10	345	347	2	Bad data. Mistake made in angle.	60	32.2	−136	—
8/10	345	348	20	Corresponds to having the stagnation line of the normal wind component on the same physical location of the model equal to the −100-degree rotation in the initial run 167 setup.	60	32.2	−136	pt11–12 bursts in both directions! Like run167 (pt4 and 11–15 state jumps).
8/10	349	350	20	Corresponds to 90-degree angle-of-attack of normal wind component.	60	46.9	39	pt8–10 the top approximately. semi-stable,15–16 the bottom bursts.
8/10	349	351	20	Corresponds to −100 degrees.	60	46.9	−151	pt9–13 bursts in both directions (pt12).
8/10	352	353	20	Corresponds to 90 degrees.	60	58.8	28	pt8 unsteady,14–15 some bursts.
8/10	352	354	20	Corresponds to −100 degrees.	60	58.8	−162	pt9–12 bursts/semi-stable (two in one!) and at "stable" TrBL1.

Day	Tare	Run No.	No. Point	Comment	Inclination (Degrees)	Yaw Angle (Degrees)	Axial Rotation (Degrees)	Observations; State Jumps
8/10	355	356	20	Corresponds to 90 degrees. Pictures taken of liquid stripe.	60	69.7	18	pt5,8,14–15. state jump between 44–47 m/s (i.e., pt8) and 58-62 m/s on screen (i.e., pt14–15).
8/10	355	357	20	Corresponds to −100 degrees.	60	69.7	−172	pt9,10 semi-stable!! pt13 bursts!
8/10	358	359	20	Corresponds to 90 degrees. Pictures taken of liquid stripe.	60	80	9	Pt8-9, 14–15 both semi-stable.
8/11	360	361	20	Corresponds to −100 degrees.	60	80	180	sudden mean lift increase between pt9 and 10. drag fluctuations pt12. Textbook CD CL!
8/11	362	363	20	Corresponds to 90 degrees.	60	90	0	pt8 bursts, pt(14–15 unsteady)16.
8/11	362	364	20	Corresponds to −100 degrees.	60	90	170	bursts and semi-stable pt10, at pt14 three semi-stable states.
8/11	365	366	20	Bad data. Cross talk on top balance. Time lost.	60	180	−90	—
8/11	367	368	20	Corresponds to 90 degrees.	60	180	−90	Picture taken of speed sweep kl 12.00. pt17 unsteady.
8/11	367	369	20	Corresponds to −100 degrees.	60	180	80	pt11, 14–16.

—No notes were taken.

Table 23. Block 3 testing, IR 113E HF.

Day	Tare	Run No.	No. Point	Comment	Inclination (Degrees)	Yaw Angle (Degrees)	Axial Rotation (Degrees)	Observations; State Jumps
8/11	370	371	20	Corresponds to having the stagnation line of the normal wind component on the same physical location of the model equal to the 55-degree rotation in the initial run 244 setup.	60	180	−125	pt6 semi-stable (run244 pt8).
8/11	370	372	20	Corresponds to having the stagnation line of the normal wind component on the same physical location of the model equal to the −48-degree rotation in the initial run 232 setup.	60	180	132	pt5–8 semi-stable (run 232 pt7–8 semi-stable).
8/11	373	374	20	Different stagnation line, corresponding to −35 degrees.	60	90	−125	—
8/11	373	375	22	Corresponds to 55 degrees.	60	90	−35	pt13–16 a bit unsteadiness.
8/12	376	377	22	Corresponds to -48 degrees.	60	90	−138	pt15–18 a bit unsteadiness.
8/12	378	379	20	Corresponds to 55 degrees.	60	80	−26	pt10–12 a bit unsteadiness.
8/12	378	380	20	Corresponds to -48 degrees.	60	80	−129	pt(10–12)13–15(16) semi-stable is starting. Pics taken at 09:50 of streamlines.
8/12	381	382	21	Corresponds to 55 degrees. Omit pt14.	60	69.7	−17	pt9–10 some semi-stable unsteadiness.

Day	Tare	Run No.	No. Point	Comment	Inclination (Degrees)	Yaw Angle (Degrees)	Axial Rotation (Degrees)	Observations; State Jumps
8/12	381	383	20	Corresponds to −48 degrees.	60	69.7	−120	some unsteadiness.
8/12	384	385	20	Corresponds to 55 degrees.	60	58.8	−7	pt7–8 semi-stable bottom, pt10–11 unsteadiness.
8/12	384	386	20	Corresponds to −48 degrees.	60	58.8	−110	—
8/12	387	388	20	Corresponds to 55 degrees.	60	46.9	4	pt7, 10–12 unsteadiness.
8/12	387	389	20	Corresponds to −48 degrees.	60	46.9	−99	pt3 jumps! Very low.
8/12	390	391	20	Corresponds to 55 degrees.	60	32.2	19	pt7 unsteadiness.
8/12	392	393	22	Corresponds to −48 degrees.	60	32.2	−84	pt11–15 unsteadiness.

—No notes were taken.

Flow visualization testing was performed using tufts and whool on a stick (sometimes noted as the wand.)

Table 24. Visualizations, JR SS13.

Day	Tare	Run No.	No. Point	Comment	Inclination (Degrees)	Yaw Angle (Degrees)	Axial Rotation (Degrees)	Observations; State Jumps
8/12	N/A	N/A	N/A	IR113E HF: Corresponds to -48 degrees. Tests with wand and whool. See videos. Loading not recorded. Approximately 10 m/s.	60	32.2	−84	—

Day	Tare	Run No.	No. Point	Comment	Inclination (Degrees)	Yaw Angle (Degrees)	Axial Rotation (Degrees)	Observations; State Jumps
8/12	N/A	N/A	N/A	IR118E: Corresponds to −100 degrees. Tests with wand and whool. See videos. Loading not recorded. Approximately 10 m/s.	60	32.2	−136	—
8/12	—	—	—	Check of load calibration, X and Y directions.	—	—	—	—
8/12	394	395	3	Load sensors: 1 kg load. Floor: 117 1/4 inch (298 cm) between load on pully and load sensor.	N/A	N/A	N/A	—

—No notes were taken.

N/A = No value associated with that test.

Table 25. Visualizations, IR 118E.

Day	Tare	Run No.	No. Point	Comment	Inclination (Degrees)	Yaw Angle (Degrees)	Axial Rotation (Degrees)	Observations; State Jumps
8/13	N/A	N/A	N/A	Flow visualization with tufts: JRSS13a.	60	0	160	As more tufts were added the aerodynamics changed to very fluctuating loads (pics taken).
8/13	N/A	N/A	N/A	Surface oil visualization. JRSS13a, U=48m/s, around 09:00 am. Some marks from the tape in the flow visualization. with tufts were seen.	60	0	160	Clear separation bubble on one side. The separation on the side with no bubble varied along the length and was further downstream on the top. Also at top and bottom but not in the middle, there were some big downward rotating vortices it seemed.
8/13	N/A	N/A	N/A	Surface oil visualization. JRSS13a, U=80m/s, around 09:20 am.	60	0	160	Clear separation bubbles on both sides.
8/13	N/A	N/A	N/A	Surface oil visualization. JRSS13b HF U=48 m/s around 09:45 am.	60	0	160	—

Day	Tare	Run No.	No. Point	Comment	Inclination (Degrees)	Yaw Angle (Degrees)	Axial Rotation (Degrees)	Observations; State Jumps
8/13	N/A	N/A	N/A	Surface oil visualization. JRSS13b HF U=25 m/s around 10:12 am. After approximately 5 min. we go up to 80 m/s as we did not see much (the magic potion did not move).	60	0	160	—
8/13	397	398	20	—	45	0	90	Very strong vortex shedding at low Reynolds numbers
8/13	397	399	20	—	45	0	−100	—
8/13	400	401	20	Corresponds to having the stagnation line of the normal wind component on the same physical location at the model equal to the 90-degree rotation in the initial run 153 setup.	45	25	56.5	—
8/13	400	402	20	Corresponds to having the stagnation line of the normal wind component on the same physical location at the model equal to the −100-degree rotation in the initial run 167 setup.	45	25	−133.5	—
8/14	403	404	20	Corresponds to 90 degrees	45	35.8	44.4	pt18–19 some bursts
8/14	403	405	20	Different stagnation line, corresponding to −167.9 degrees.	45	35.8	146.5	pt14–16, 19-20 bursts.

Day	Tare	Run No.	No. Point	Comment	Inclination (Degrees)	Yaw Angle (Degrees)	Axial Rotation (Degrees)	Observations; State Jumps
8/14	403	406	20	Corresponds to −100 degrees.	45	35.8	−145.5	pt6 unstable, pt12–16 bursts.

—No notes were taken.
N/A = No value associated with that test.

Table 26. Visualizations, IR 113E HF.

Day	Tare	Run No.	No. Point	Comment	Inclination (Degrees)	Yaw Angle (Degrees)	Axial Rotation (Degrees)	Observations; State Jumps
8/14	407	408	22	Corresponds to having the stagnation line of the normal wind component on the same physical location of the model equal to the 55-degree rotation in the initial run 244 setup.	45	35.8	9.5	pt5–9 semi-stable! Some unsteady.
8/14	407	409	22	Corresponds to having the stagnation line of the normal wind component on the same physical location of the model equal to the −48-degree rotation in the initial run 232 setup.	45	35.8	−93.5	pt7–10 semi-stable.
8/14	410	411	22	Corresponds to 55 degrees.	45	24.6	22	—
8/14	410	412	22	Corresponds to −48 degrees.	45	24.6	−81	—
8/14	413	414	22	—	45	0	55	—
8/14	413	415	23	—	45	0	−48	—

—No notes were taken.

Table 27. Cobra probe, IR 113E HF.

| Day	Tare	Run No.	No. Point	Comment	Inclination (Degrees)	Yaw Angle (Degrees)	Axial Rotation (Degrees)	Observations; State Jumps
8/14	417	416	2	Cobra probe, 2D downwind cable measured from cable center line, and approximately 10 cm outwards from cable edge with the helical fillets near normal to flow (the side opposite control room, the right side as seen by the wind).	45	35.8	−93.5	—
8/14	417	418	2	Cobra probe, 2D downwind cable measured from cable center line, and approximately 5 cm outwards from cable edge with the helical fillets near normal to flow (the side opposite control room, the right side as seen by the wind).	45	35.8	−93.5	—

Day	Tare	Run No.	No. Point	Comment	Inclination (Degrees)	Yaw Angle (Degrees)	Axial Rotation (Degrees)	Observations; State Jumps
8/14	417	419	1	Cobra probe, 2D downwind cable measured from cable center line, and approximately 2.5 cm outwards from cable edge with the helical fillets near normal to flow (the side opposite control room, the right side as seen by the wind).	45	35.8	−93.5	—
8/14	417	420	1	Cobra probe, 2D downwind cable measured from cable center line, and approximately along cable edge with the helical fillets near normal to flow (the side opposite control room, the right side as seen by the wind).	45	35.8	−93.5	—
8/14	417	421	1	Cobra probe, 2D downwind cable measured from cable center line, and approximately 2.5 cm inward from cable edge with the helical fillets near normal to flow (the side opposite control room, the right side as seen by the wind).	45	35.8	−93.5	—

Day	Tare	Run No.	No. Point	Comment	Inclination (Degrees)	Yaw Angle (Degrees)	Axial Rotation (Degrees)	Observations; State Jumps
8/14	417	422	1	Cobra probe, 2D downwind cable measured from cable center line, and approximately 5 cm from cable edge with the inward helical fillets near normal to flow (the side opposite control room, the right side as seen by the wind).	45	35.8	−93.5	—

— No notes were taken.

APPENDIX B. ADDITIONAL EXPERIMENTAL RESULTS IN GRAPHICAL FORM

Figure 54 and figure 55 show plots of aerodynamic force coefficients as a function of Reynolds number. Figure 56 compares the aerodynamic forces on the top and bottom force sensors of the model. Figure 57 through figure 65 show plots of the mean force coefficients for the oval and circular cylinder shapes at varying angles of attack.
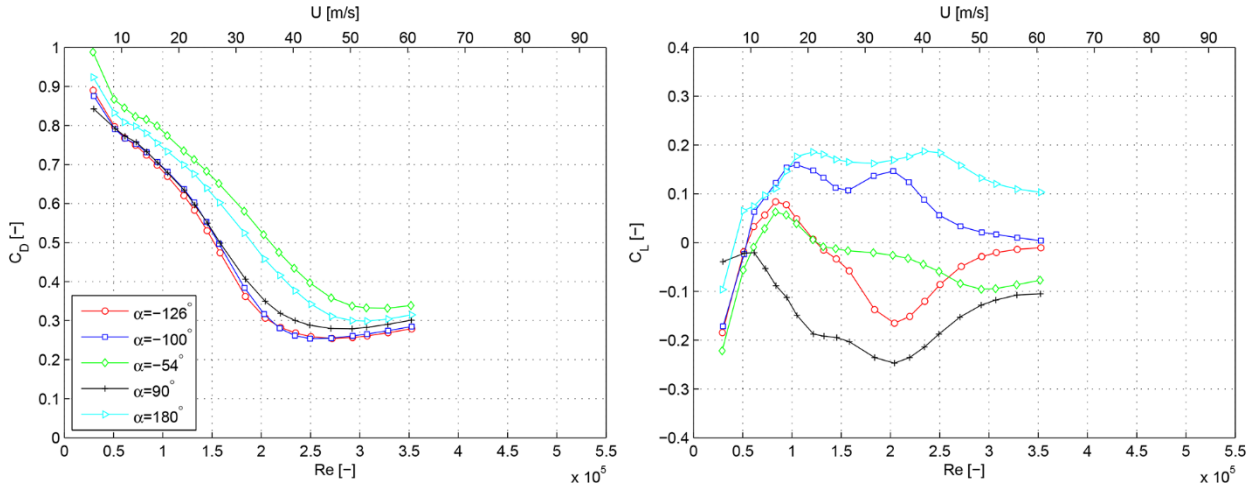
Source: FHWA.
Note: Cable model at 60-degree inclination.

Figure 54. Graph. Aerodynamic force coefficients as a function of Reynolds number in turbulent flow for cable model IR118E.
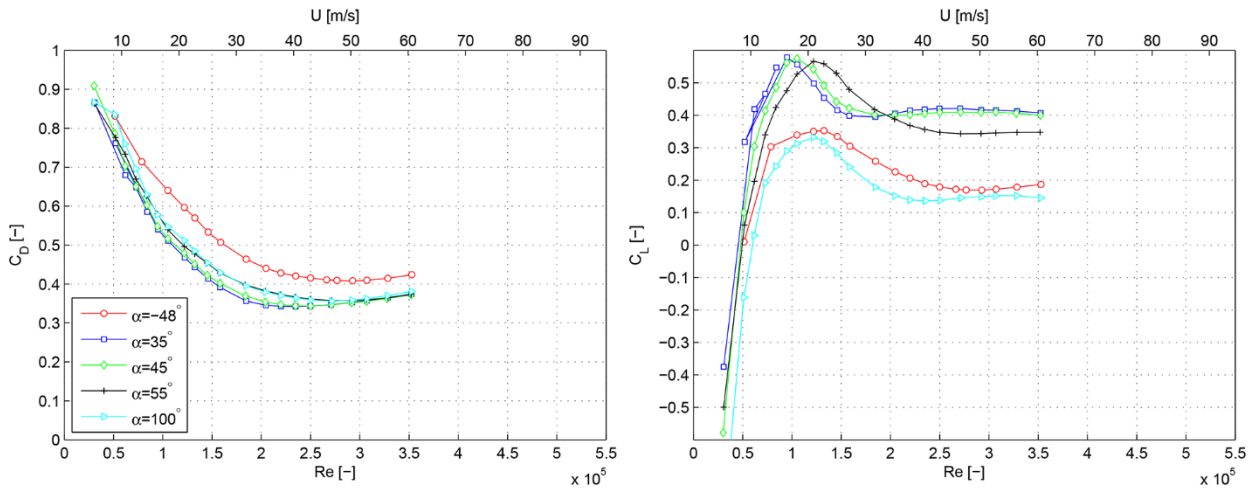
Source: FHWA.
Note: Cable model at 60-degree inclination.

Figure 55. Graph. Aerodynamic force coefficients as a function of Reynolds number in turbulent flow for cable model IR113E HF.
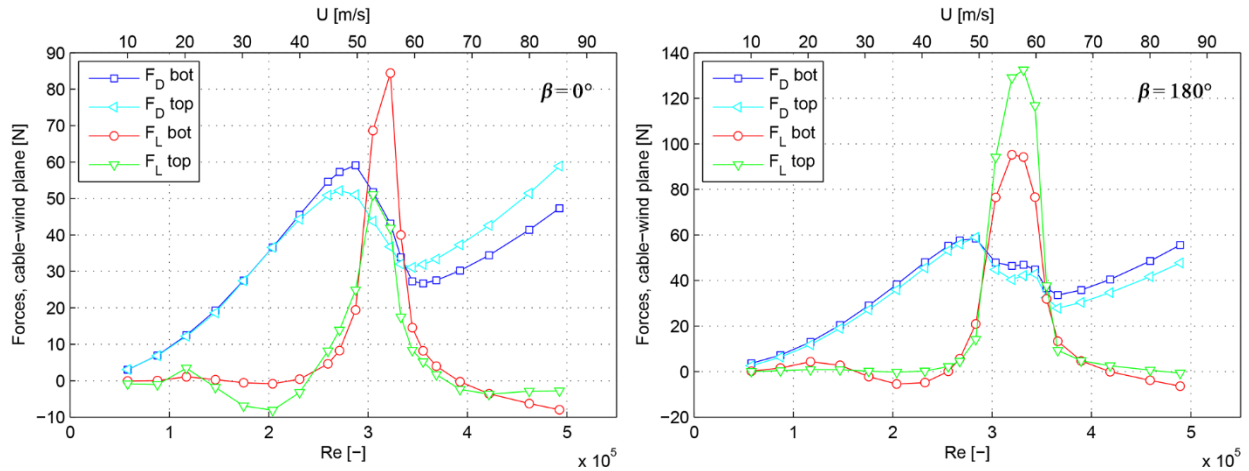
Note: Cable model at 60-degree inclination. Angle of attack $\alpha = -100$ degrees. Left: run 167, yaw angle = 0 degrees. Right: run 369, yaw angle = 180 degrees.

Figure 56. Graph. Variations of the aerodynamic forces measured by the top and bottom force sensors as a function of Reynolds number in smooth flow for cable model IR118E.
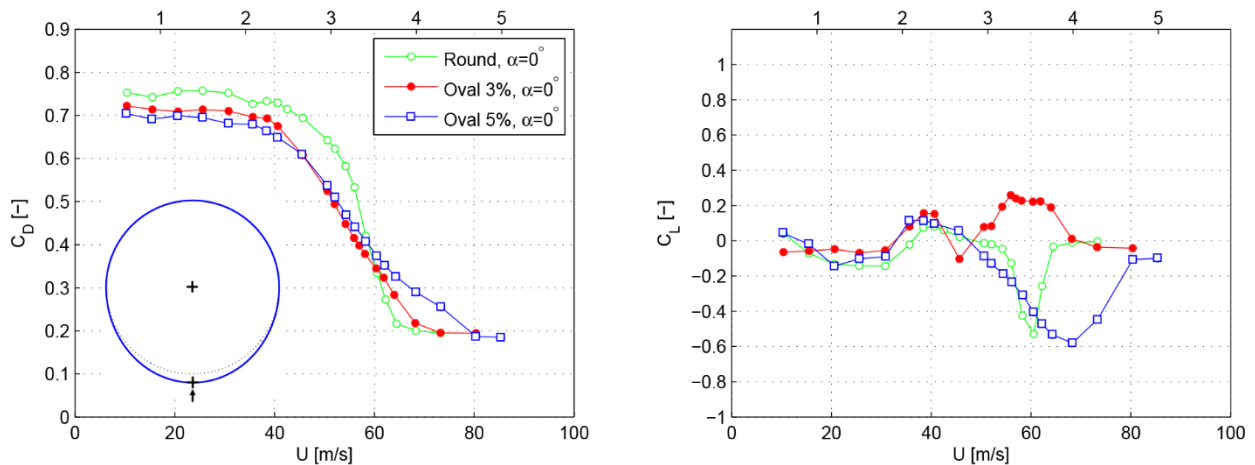
Note: Cable models at 60-degree inclination.

Figure 57. Graph. Mean drag and lift coefficients as a function of wind speeds for the oval and round cylinders at angles of attack $\alpha = 0$ degrees.
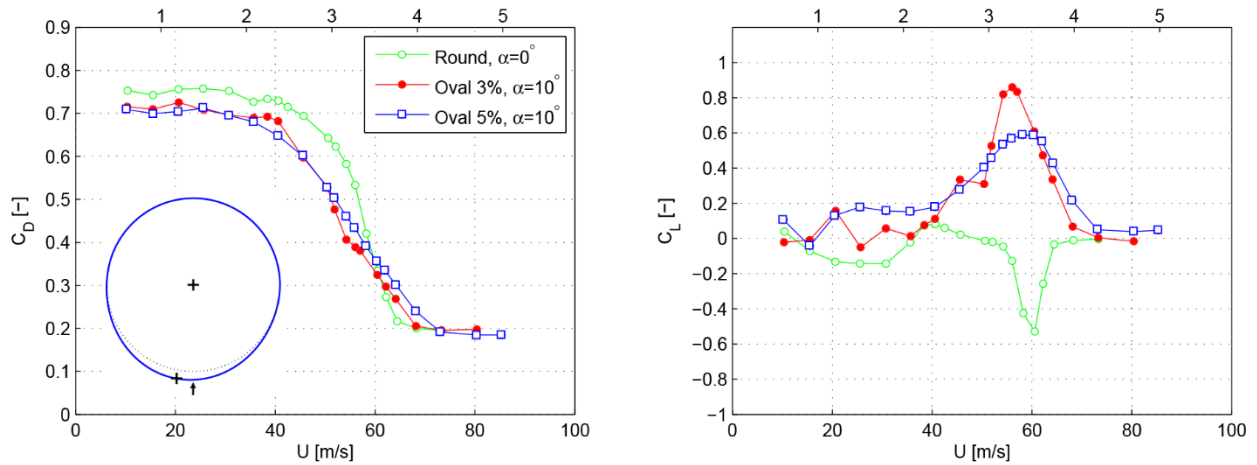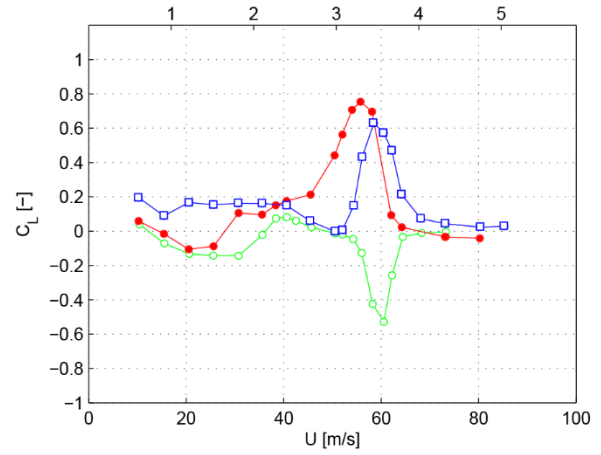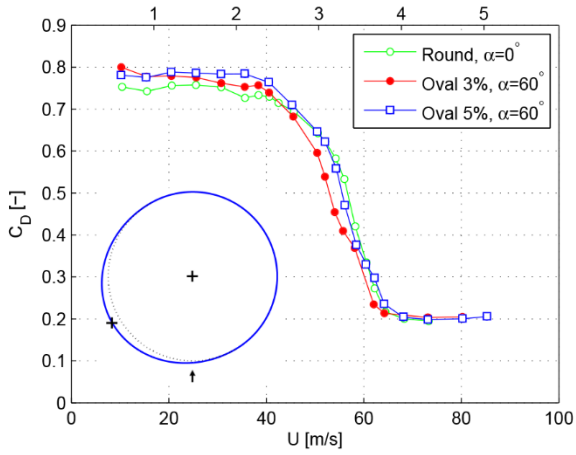
Figure 58. Graph. Mean drag and lift coefficients as a function of wind speeds for the oval and round cylinders at angles of attack α = 10 degrees.
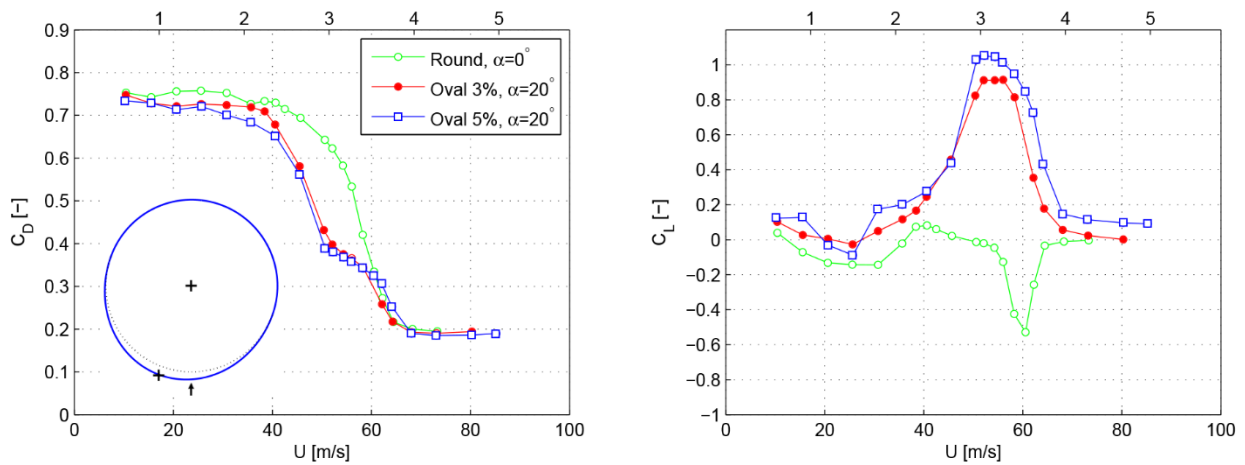
Figure 59. Graph. Mean drag and lift coefficients as a function of wind speeds for the oval and round cylinders at angles of attack α = 20 degrees.
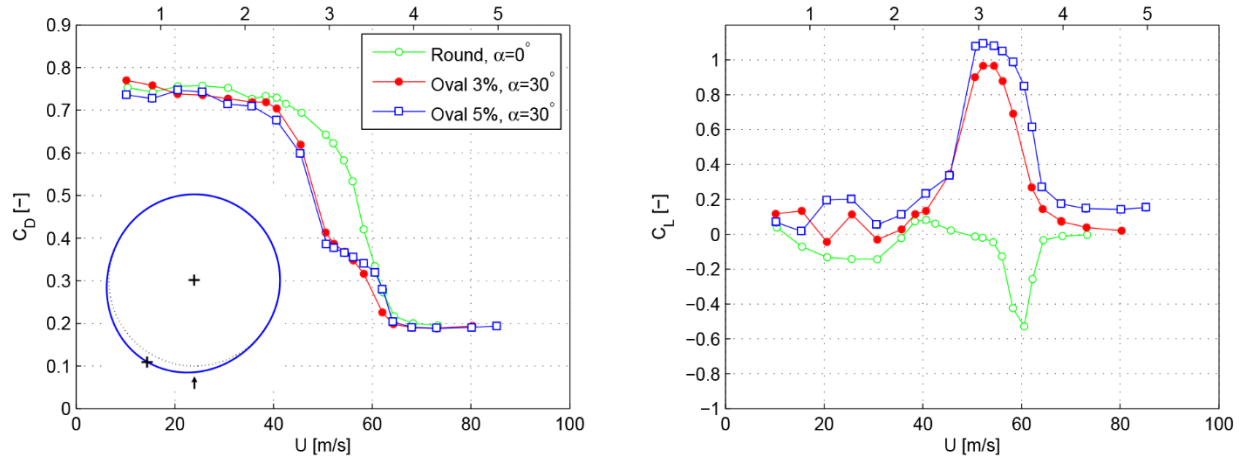
Note: Cable models at 60-degree inclination.

Figure 60. Graph. Mean drag and lift coefficients as a function of wind speeds for the oval and round cylinders at angles of attack α = 30 degrees.
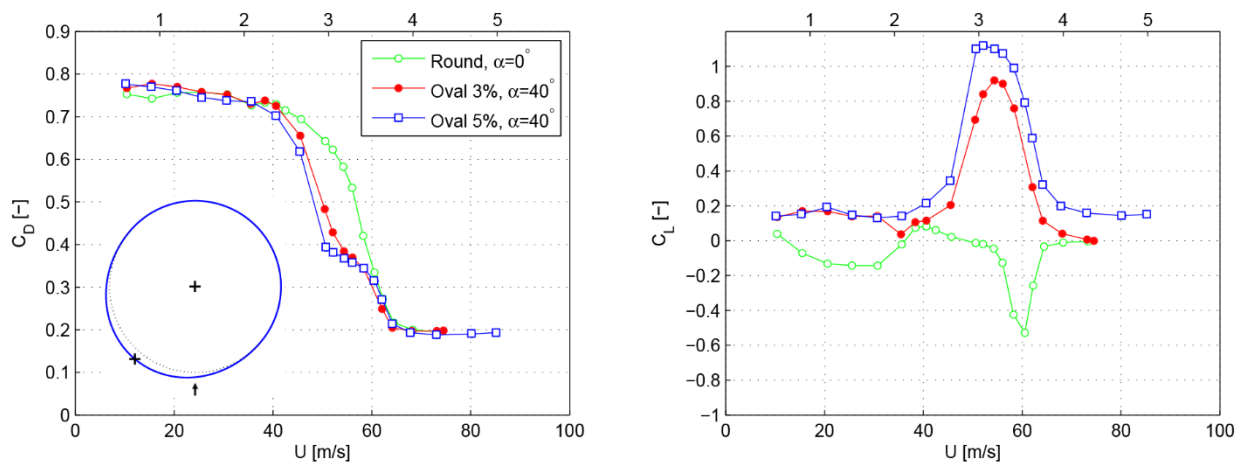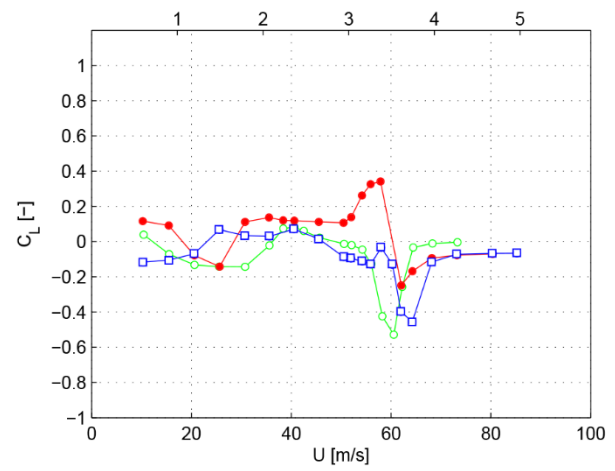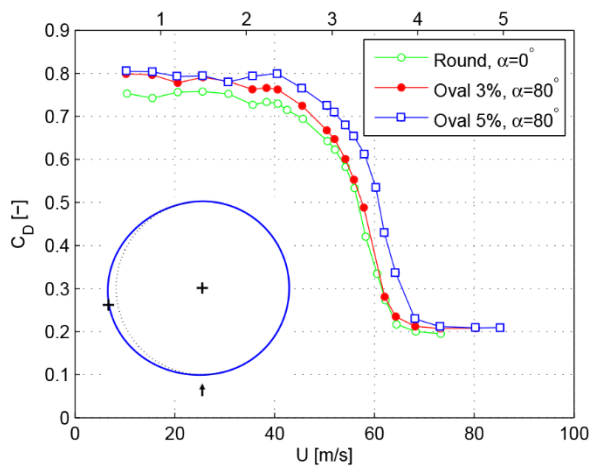
Note: Cable models at 60-degree inclination.

Figure 61. Graph. Mean drag and lift coefficients as a function of wind speeds for the oval and round cylinders at angles of attack α = 40 degrees.

Note: Cable models at 60-degree inclination.

Figure 62. Graph. Mean drag and lift coefficients as a function of wind speeds for the oval and round cylinders at angles of attack α = 60 degrees.
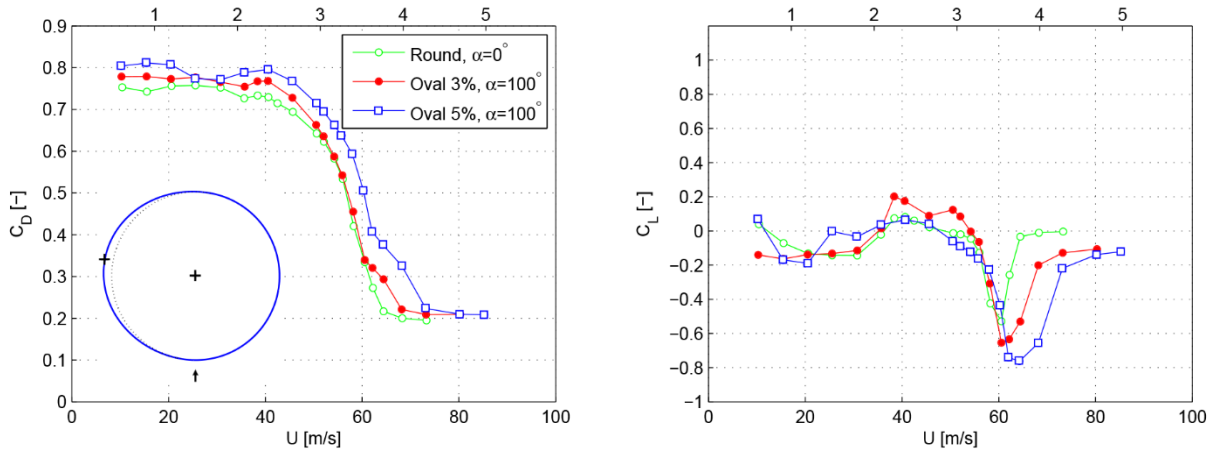
Note: Cable models at 60-degree inclination.

Figure 63. Graph. Mean drag and lift coefficients as a function of wind speeds for the oval and round cylinders at angles of attack α = 80 degrees.

Note: Cable models at 60-degree inclination.

Figure 64. Graph. Mean drag and lift coefficients as a function of wind speeds for the oval and round cylinders at angles of attack α = 100 degrees.
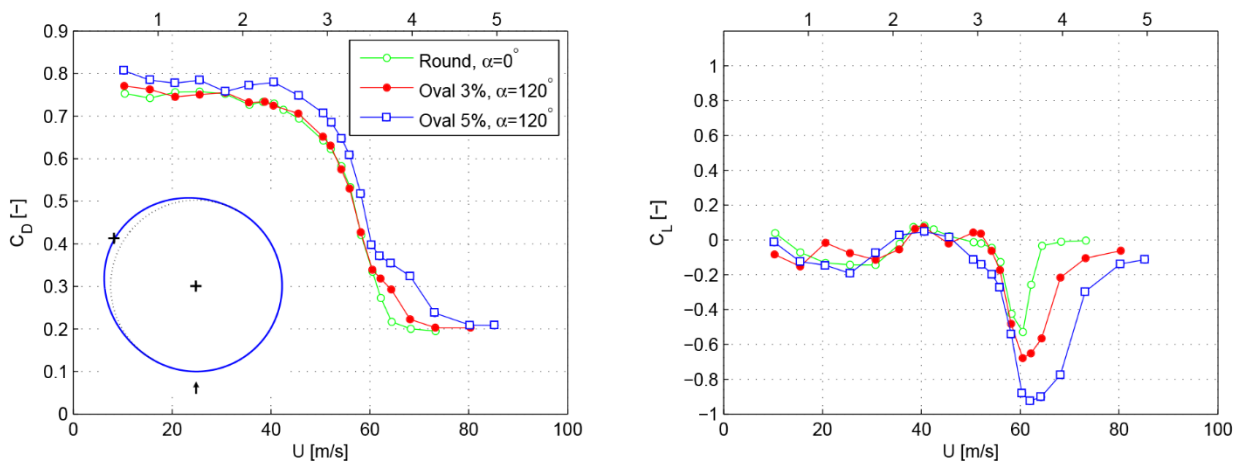
Note: Cable models at 60-degree inclination.

Figure 65. Graph. Mean drag and lift coefficients as a function of wind speeds for the oval and round cylinders at angles of attack α = 120 degrees.

REFERENCES

1. Post-Tensioning Institute. 2012. *Recommendations for Stay Cable Design, Testing and Installation, Sixth Edition*. PTI DC45.1-12. Phoenix, AZ: Post-Tensioning Institute.

2. Kumarasena, S., N. Jones, P. Irwin, P. Taylor. 2007. *Wind-Induced Vibration of Stay Cables*. Report No. FHWA-HRT-05-083. Washington, DC: Federal Highway Administration.

3. Park, S. and H.R. Bosch. 2014. *Mitigation of Wind-Induced Vibration of Stay Cables: Numerical Simulations and Evaluations*. Report No. FHWA-HRT-14-049, Federal Highway Administration, Washington, DC.

4. Larose, G. and A. D'Auteuil. 2014. *Wind Tunnel Investigations of an Inclined Stay Cable with a Helical Fillet*. Report No. FHWA-HRT-14-070. Washington, DC: Federal Highway Administration.

5. Bosch, H.R. and J.R. Pagenkopf. 2014. *Dynamic Properties of Stay Cables on the Penobscot Narrows Bridge*. Report No. FHWA-HRT-14-067. Washington, DC: Federal Highway Administration.

6. Bosch, H.R. and J.R. Pagenkopf. 2017. *Dynamic Properties of Stay Cables on the Bill Emerson Bridge*. Report No. FHWA-HRT-17-037. Washington, DC: Federal Highway Administration.

7. Christiansen, H., G. Larose, J. Jakobsen, and H. Bosch. 2016. "Aerodynamics of a Flat Faced and Oval Cylinders with Applications to Bridge Stay Cables," *Journal of Fluids and Structures*, (submitted).

8. Christiansen, H., G. Larose, J. Jakobsen, and H. Bosch. 2016. "Aerodynamics of Bridge Stay Cables Based on Cross-sectional Shapes Measured in the Field," *Journal of Fluids and Structures*, (submitted).

9. Larose, G., M. Savage, and J. Jakobsen. 2003. "Wind Tunnel Experiments on an Inclined and Yawed Circular Cylinder in the Critical Reynolds Number Range," Presented at *11th International Conference On Wind Engineering*. Lubbock, Texas: International Conference On Wind Engineering.

10. Matteoni, G. and C. Georgakis. 2012. "Effects of Bridge Cable Surface Roughness and Cross-sectional Distortion on Aerodynamic Force Coefficients," *Journal of Wind Engineering and Industrial Aerodynamics* 104–106, May-July 2012: 176–187.

11. Engineering Sciences Data Unit International. 1986. *Mean Forces, Pressures and Flow Field Velocities for Circular Cylindrical Structures: Single Cylinder with Two-dimensional Flow*. ESDU 80025. London, UK: Engineering Science Data Unit.

12. Zasso, A., G. Larose, S. Giappino, and S. Muggiasca. 2005. "Effects of Turbulence Intensity and Surface Roughness on Stays of Cable Stayed Bridges" Presented at the *6th International Symposium on Cable Dynamics*. Charleston, SC: International Symposium on Cable Dynamics.

13. Hackett, J. and K. Cooper. 2001. "Extensions to Maskell's Theory for Blockage Effects on Bluff Bodies in a Closed Wind Tunnel," *Aeronautical Journal* 105, no. 1050: 409–418.

14. Benidir, A., O. Flamand, L. Gaillet, and G. Dimitriadis. 2015. "Impact of Roughness and Circularity-defect on Bridge Cables Stability," *Journal of Wind Engineering and Industrial Aerodynamics* 137, Feb. 2015: 1–13.

15. Zdravkovich, M. 1997. *Flow around Circular Cylinders, Volume 1*, Oxford, UK: Oxford University Press.

16. Ma, W., Q. Liu, X. Du, and Y. Wei. 2015. "The Effect of Reynolds Number on the Aerodynamic Forces and Galloping Instability of Cylinder with Semi-elliptical Cross-sections." Presented at the *14th International Conference on Wind Engineering*. Porto Alegre, Brazil: International Conference on Wind Engineering.

17. D'Auteuil, A., G. Larose, and S. Zan. 2012. "Wind Turbulence in Speed Skating: Measurement, Simulation and its Effect on Aerodynamic Drag." *Journal of Wind Engineering and Industrial Aerodynamics* 104–106, May-July 2012: 585–593.

18. MATLAB. 2006. *Computer Software*. Version 2015a.

19. Den Hartog, J. 1985. *Mechanical Vibrations*. Mineola, NY: Dover Publications.

20. Lockwood, V. 1967. *Effects of Reynolds Number and Flow Incidence on the Force Characteristics of a Family of Flat-front Cylinders*. Report No. NASA-TN-D-3932. Hampton, VA: National Aeronautics and Space Administration.

21. Macdonald, J. and G. Larose. 2006. "A Unified Approach to Aerodynamic Damping and Drag/Lift Instabilities, and its Application to Dry Inclined Cable Galloping," *Journal of Wind and Structures* 22, no.2: 229–252.

22. Christiansen, H., J. Jakobsen, J. Macdonald, G. Larose, and H. Bosch. 2018. "Aerodynamics of a Stay Cable with Helical Fillets - Part I: Stability and Load Characteristics." *Journal of Wind Engineering and Industrial Aerodynamics* 177: 376–391.

23. Bursnall, W. and L. Loftin. 1951. *Experimental Investigation of the Pressure Distribution About a Yawed Circular Cylinder in the Critical Reynolds Number Range*. NACA-TN-2463. Langley Field, VA: National Advisory Committee for Aeronautics.

24. Kleissl, K. and Georgakis, C. 2012. "Comparison of the Aerodynamics of Bridge Cables with Helical Fillets and a Pattern-indented Surface," *Journal of Wind Engineering and Industrial Aerodynamics* 104–106, May-July 2012: 166–175.